Soft robotic manipulators with proprioception

Scharff, R.B.N.

DOI
10.4233/uuid:2a2a3b0d-7dee-4518-b96d-42dd58492ffd

Publication date
2021

Document Version
Final published version

Citation (APA)
Scharff, R. B. N. (2021). *Soft robotic manipulators with proprioception*. [Dissertation (TU Delft), Delft University of Technology]. https://doi.org/10.4233/uuid:2a2a3b0d-7dee-4518-b96d-42dd58492ffd

Soft Robotic Manipulators with Proprioception

Dissertation

for the purpose of obtaining the degree of doctor
at Delft University of Technology
by the authority of the Rector Magnificus Prof.dr.ir. T.H.J.J. van der Hagen,
chair of the Board for Doctorates,
to be defended publicly on
Monday 26 April 2021 at 15:00 o'clock by

Rob Bernardus Nicolaas SCHARFF

Master of Science in Integrated Product Design,
Delft University of Technology, the Netherlands,
born in Zederik, the Netherlands.

This dissertation has been approved by the promotors

Composition of the doctoral committee:

Rector Magnificus	chairperson
Prof.dr. C.C.L. Wang	Delft University of Technology, promotor
Prof.dr.ir. J.M.P. Geraedts	Delft University of Technology, promotor
Dr. J. Wu	Delft University of Technology, copromotor

Independent members:

Prof.dr.ir. R. H. M. Goossens	Delft University of Technology
Prof.dr.ir. D. A. Abbink	Delft University of Technology
Dr. B. Mazzolai	Instituto Italiano di Tecnologia
Dr. A. Weightman	The University of Manchester
Prof.dr. P. Vink	Delft University of Technology, reserve member

Keywords: Soft Robotics, Proprioception

Printed by: Ridderprint, the Netherlands

Front & Back: M.A. Sandoval Martinez

ISBN 978-94-6384-193-1

An electronic version of this dissertation is available at
`http://repository.tudelft.nl/`.

Table of Contents

Glossary

Abbreviations

3D	Threedimensional
AM	Additive Manufacturing
DOF	Degree Of Freedom
FDM	Fused Deposition Modeling
FNN	Feedforward Neural Network
LDR	Light-Dependent Resistor
LED	Light-Emitting Diode
LSTM	Long Short-Term Memory
MSE	Mean Squared Error
MVLR	Multivariate Linear Regression
MVPR	Multivariate Polynomial Regression
PLA	Polylactic Acid
RGB	Red, Green, and Blue
RGBC	Red, Green, Blue, and Clear
SLS	Selective Laser Sintering
SVR	Support Vector Regression
TPU	Thermoplastic Polyurethane

Definitions

3D Printing See *Additive Manufacturing*

Actuator A device that converts energy to mechanical action in such a way that it can be controlled. In the case of soft pneumatic actuators, the word actuator is used to refer to every air chamber that can be independently controlled

Additive Manufacturing (AM) A manufacturing method based on building threedimensional objects from digital files, usually by adding material in a layer-wise manner

Bellow An air chamber that deforms upon inflation. Sometimes used to refer to the smallest repeating unit within the air chamber

Compliant Mechanism A flexible mechanism that achieves transmission of force and motion through elastic deformation

Closed-Loop Control A control system in which the control action is dependent on the output generated by the system

Degrees of Freedom (DOFs) The number of independent aspects of motion that determine the configuration of a mechanical system such as a (soft) robot

Dexterous Manipulation The ability of a manipulator to perform a task in a skillful and effective way

Feedforward Neural Network (FNN) Machine learning algorithm consisting of an artificial neural network with no feedback connections

Fused Deposition Modeling (FDM) An additive manufacturing technology based on the extrusion of a thermoplastic filament

Gripper A device for prehension purposes

Long Short-Term Memory (LSTM) Machine learning algorithm consisting of an artificial recurrent neural network structure with feedback connections

Machine Learning Algorithm Algorithm that builds a model based on training data in order to make predictions, without being explicitly programmed to do so

Manipulator A device that physically interacts with its environment in order to perform a task. In this dissertation, it is mostly used to refer to devices that are aimed at replacing the human hand

Multivariate Linear Regression (MVLR) Machine learning algorithm that applies linear regression with more than one dependent variables and one or more predictor variables

Multivariate Polynomial Regression (MVPR) Machine learning algorithm that models the relationship between more than one dependent variables and one or more predictor variables as a polynomial

Open-Loop Control A control system in which the control action is independent of the output generated by the system

Out-of-Plane Deformation Deformation outside the primary plane in which the deformation is intended

Photopolymer A class of materials that undergo photochemical reactions upon exposure to light that result in changes in their structures that modify their chemical and mechanical properties

PolyJet An additive manufacturing technology that involves jetting photopolymer droplets and solidifying them with an ultraviolet light

Proprioception Perception or awareness of the position and movement of the body

Robot A machine that can sense, analyze, decide, and act without human intervention

Selective Laser Sintering (SLS) An additive manufacturing technology in which a laser is used to selectively induce fusion between powder particles

Soft Robot A robot that is primarily composed of materials with moduli in the range of the moduli of soft biological materials (Young's moduli between 10^4 and 10^9 Pa)

Support Vector Regression (SVR) Machine learning algorithm based on constructing a hyperplane or set of hyperplanes in a high- or infinite-dimensional space for regression

Underactuated System A system in which the number of actuators is less than the number of degrees of freedom of the system

Summary

Agriculture and horticulture depend heavily on human labor to perform tasks that are often dirty, hazardous, and highly repetitive. One reason for the lack of automation of these tasks is the absence of suitable robotic handling equipment. Rigid robotic manipulators are typically incapable of performing dexterous manipulation tasks such as harvesting apples as they lack the ability to adapt to objects of various shapes and sizes. Such robotic manipulators need a large number of sensors and actuators to overcome these challenges, making them overly complex and not very robust. Therefore, the development of robotic manipulators for dexterous manipulation tasks has begun to focus on morphological computation, in which at least some aspects of the control are outsourced to the body of the robot.

Taking inspiration from grasping mechanisms in natural systems, the field of soft robotics attempts to address this problem by constructing robots from soft materials. Although soft robotics may be the key to realizing automation of dexterous manipulation tasks, the current commercially available soft robotic grippers are only capable of performing simple pick-and-place tasks with open-loop control. This limited capability is in large part due to a lack of techniques to endow these manipulators with a sense of self-movement and body position, known as proprioception. Proprioception is a simple problem for conventional robots with rigid members and discrete joints, as the body position can be easily reconstructed using the information from encoders in the robots' joints. However, it is a highly challenging problem for soft robots with virtually infinite degrees of freedom and above all, no suitable off-the-shelf sensors.

The objective of this research is to develop a systematic approach to building soft robotic manipulators with accurate proprioception in order to enable the development of closed-loop control algorithms for dexterous soft robots. This approach includes fabricating actuators with desired behavior, designing sensors to capture the deformation of these actuators, calibrating the sensors, and reconstructing the deformed shape. How to best accomplish these steps remains an open question.

This dissertation focuses on soft robots that are actuated through inflation of soft material air chambers. Pneumatic actuation of soft robots has significant advantages over other types of actuation as it does not require electric wiring and allows for customization of the robots' behavior by altering the shape and size of the air chambers. The fabrication of these customized designs can be

realized through additive manufacturing (AM). It is demonstrated in this work that multiple soft actuators and sensors can be integrated into a monolithic soft robot.

The presence of the air chambers is then exploited for proprioception purposes. The inner walls of the air chamber are illuminated with one or more small light sources and the reflected light is measured with multiple optical (color) sensors. Deformations of the air chamber result in changes in the reflection of light and thus in a change in the signal of the optical sensors. The sensitivity of the sensing method can be increased by optimizing the placement of the sensors as well as by integrating structures that maximize changes in light intensity and color as a result of deformation. This is demonstrated through a soft bending actuator that exploits multi-material AM to integrate a multi-color structure as signal generator inside the air chamber.

A machine learning-based calibration method is employed to translate the sensor readings to the corresponding shape of the soft actuator. The target variables are obtained through the capturing of strategically placed markers on the actuators by one or more cameras, while the actuator undergoes a range of deformations through a combination of an actuation pressure and external forces. Results indicate that the coordinates of the markers can be accurately predicted from the sensor readings even when the actuator is interacting with objects.

This collection of points must be converted to a soft robot representation that is useful for real-time visualization and closed-loop control. To this end, the captured marker coordinates are converted to shape parameters prior to training of the machine learning model. The machine learning model then predicts shape parameters that can be used to reconstruct the shape of soft robots in real-time. This process is demonstrated for the deformation of a soft continuum joint represented as a transformation matrix and the shape of a soft membrane represented by the control points of a Bézier-surface.

Besides capturing and reconstructing the shape of soft robots, it is important to prevent the undesired deformation in soft robots from occurring in the first place. Out-of-plane deformation in soft pneumatic bending actuators is a major cause of failed grasps in soft robotic manipulators. Out-of-plane deformation can be reduced by embedding a stiffening structure inspired by spatial flexures in the 3D-printed soft actuator. This structure reduces the out-of-plane deformation without significantly increasing the in-plane bending stiffness. Thus, the number of degrees of freedom that need to be captured and reconstructed can be reduced.

In conclusion, this dissertation presents an approach to building soft robotic manipulators equipped with accurate proprioception. The compatibility of the chosen sensing, actuation, and fabrication techniques allows the designer to easily realize soft robotic manipulators with the desired behavior through an integrated design approach. Thus, this research provides an excellent starting point for the development of more advanced closed-loop control algorithms for soft robotic manipulators. Eventually, this development will enable soft robotic manipulators to perform dexterous manipulation tasks.

Samenvatting

Landbouw en tuinbouw zijn zeer afhankelijk van menselijke arbeid voor het uitvoeren van taken die vuil, gevaarlijk, en zeer repetitief zijn. Een van de redenen voor het uitblijven van automatisering van deze taken is het gebrek aan geschikt gereedschap voor robots om dergelijke natuurlijke objecten te hanteren. Harde robotische manipulatoren zijn normaliter niet goed in het volbrengen van taken zoals het plukken van appels omdat ze niet goed in staat zijn zich aan te passen aan kwetsbare objecten met verschillende vormen en groottes. Een groot aantal sensoren en actuatoren zijn nodig om dergelijke functionaliteiten te bewerkstelligen in harde robotische manipulatoren. Om dit te omzeilen, is de focus in de ontwikkeling van robotische manipulatoren komen te liggen bij het vereenvoudigen van de aansturing van de robot door een deel van de aansturing uit te besteden aan het lichaam van de robot.

Geïnspireerd door grijp-mechanismen in natuurlijke systemen, richt het onderzoeksgebied van de zachte robotica zich op het aanpakken van dit probleem door het gebruik van zachte materialen in het bouwen van robots. Hoewel zachte robotica wel eens de sleutel zou kunnen zijn tot het automatiseren van taken die fijne motoriek vereisen, zijn de huidige commercieel beschikbare zachte grijpers slechts in staat tot het uitvoeren van eenvoudige ‘pick-and-place’-taken met een open regelkring. Dit komt met name door het gebrek aan middelen om deze grijpers uit te rusten met het vermogen om de positie van het eigen lichaam en lichaamsdelen waar te nemen (ook wel proprioceptie genoemd). Proprioceptie is een goed opgelost probleem voor harde robots met rigide leden en discrete gewrichten, aangezien de positie van de robot gereconstrueerd kan worden aan de hand van de informatie van codeerapparaten in de gewrichten van de robot. Daarintegen is proprioceptie een zeer uitdagend probleem voor zachte robots met vrijwel oneindig veel vrijheidsgraden en geen geschikte ‘off-the-shelf’ sensoren.

Het doel van dit onderzoek is het ontwikkelen van een systematische aanpak om zachte robotische manipulatoren met nauwkeurige proprioceptie te bouwen om zo de weg vrij te maken voor de ontwikkeling van aansturingen voor zachte robots middels een gesloten regelkring voor het uitvoeren van taken die fijne motoriek vereisen. Dit omvat het fabriceren van actuatoren met gewenst gedrag, het ontwerpen van sensoren om de deformatie van de actuatoren vast te leggen, het kalibreren van deze sensoren, en het reconstrueren van de vorm van de robot. Hoe deze stappen het best verwezenlijkt kunnen worden is nog een open vraag.

Dit proefschrift richt zich op zachte robots die aangedreven worden door perslucht in luchtkamers gemaakt van een zacht materiaal te blazen. Pneumatische aandrijving van zachte robots biedt voordelen boven andere aandrijvingen aangezien er geen elektrische bedrading nodig is en het gedrag van de robot op maat gemaakt kan worden door het aanpassen van de vorm en grootte van de luchtkamers. Deze op maat gemaakte ontwerpen kunnen gefabriceerd worden middels additive manufacturing. Zodoende kunnen meerdere zachte actuatoren en sensoren worden geïntegreerd in een monolithische zachte robot.

De aanwezigheid van de luchtkamers wordt vervolgens benut voor het realiseren van proprioceptie. De inwendige wanden van de luchtkamers worden belicht met één of meerdere lichtbronnen en het gereflecteerde licht wordt gemeten door meerdere optische (kleuren) sensoren. Deformatie van de luchtkamer resulteert in veranderingen in de reflectie van het licht en leidt daardoor tot een verandering in het signaal van de optische sensoren. De gevoeligheid van de meetmethode kan worden verhoogd door de plaatsing van de sensoren te optimaliseren en door structuren te integreren die de verschillen in licht intensiteit en kleur ten gevolge van deformatie van de luchtkamer maximaliseren. Dit wordt gedemonstreerd aan de hand van een zachte robot vinger waarin met behulp van multi-materiaal AM een kleurenstructuur binnenin de luchtkamer is geïntegreerd.

Een machinaal leren-gebaseerde kalibratie wordt toegepast om de signalen van de sensoren te vertalen naar de bijbehorende vorm van de zachte actuator. De doelvariabelen worden verkregen door strategisch geplaatste markers op de actuatoren met één of meer cameras vast te leggen, terwijl de actuator gedeformeerd wordt door een combinatie van perslucht in de luchtkamer en externe krachten. De coördinaten van de markers kunnen nauwkeurig voorspeld worden aan de hand van de sensor signalen, zelfs wanneer de actuator in interactie is met objecten.

Deze collectie van punten moet worden omgezet naar een representatie van de zachte robot die bruikbaar is voor realtime visualisatie en het aansturen van zachte robots met een gesloten regelkring. De vastgelegde marker coördinaten worden daarom eerst omgezet naar parameters van waaruit de vorm van de robot efficiënt gereconstrueerd kan worden. Deze vorm-parameters worden direct als doelvariabelen gebruikt voor het machinaal leren. In dit proefschrift wordt de deformatie van een zacht continuüm gewricht gerepresenteerd door een transformatiematrix, en de vorm van een zacht membraan gerepresenteerd door de controlepunten van een Bézier-oppervlak.

Naast het vastleggen en reconstrueren van de vorm van zachte robots, is het belangrijk om de deformatie die niet gewenst is te voorkomen. De uit het vlak deformatie in zachte robot vingers is een belangrijke oorzaak van mislukte grepen van zachte robotische manipulatoren. Deze deformatie kan gereduceerd worden door een structuur in de actuator te integreren. Deze structuur verminderd de uit het vlak deformatie zonder de stijfheid in het vlak noemenswaardig te verhogen. Hiermee kan het aantal vrijheidsgraden dat vastgelegd en gereconstrueerd moet worden gereduceerd worden.

In conclusie, dit onderzoek presenteert een aanpak tot het bouwen van zachte robotische manipulatoren uitgerust met nauwkeurige proprioceptie. De compatibiliteit van de gebruikte technieken voor het meten, aandrijven, en fabriceren van de zachte robot stelt de ontwerper in staat om eenvoudig een manipulator met het gewenste gedrag te realiseren middels een integrale ontwerp aanpak. Het onderzoek vormt hiermee een uitstekend uitgangspunt voor het ontwikkelen van algortihmes voor het aansturen van zachte robotische manipulatoren met een gesloten regelkring. Dit maakt het gebruik van zachte robotische manipulatoren voor het uitvoeren van fijn motorische taken mogelijk.

1

Introduction

This chapter provides a brief overview of robotic manipulators for the automation of dexterous manipulation tasks. It then introduces soft robotics as a new field of research with the potential to revolutionize robotic manipulation. Next, it identifies the ability to build soft robotic manipulators endowed with accurate proprioception as a crucial step towards advancing this line of research. The main challenges in achieving this objective are explained and four research questions are defined. The chapter concludes with a discussion of the research cycles in which the research questions will be addressed, as well as the organization of the work.

1.1 Introduction

Ever since the first industrial robots entered the market, robots have been known for their excellent capabilities in executing high-speed, high-precision, and high-force tasks in structured and well-known environments. As a result, industries with the right boundary conditions have drastically increased their productivity by employing robots to perform these types of tasks. However, robots have failed to make a similar impact in industries that require the execution of tasks in highly unstructured and unpredictable environments, such as agriculture and horticulture. As a consequence, these industries still heavily depend on human labor to perform tasks that are often dirty, hazardous and highly repetitive. Moreover, the need for workers to be able to access the workplace often limits the achievable yield through restrictions in terms of usable space and environmental conditions (e.g. temperature and CO_2 levels). The automation of dexterous manipulation tasks in unstructured environments would allow for a more bio-diverse and thus unstructured use of agricultural land. This approach to land use would in turn allow for a more sustainable farming concept known as agroforestry that could mitigate non-point source pollution, control soil erosion, and create wildlife habitats. One of the main challenges in automating these tasks is the lack of appropriate handling equipment that can interact with an unknown environment in a desired way.

For example, a task such as harvesting apples (see Figure 1.1) requires adjusting a caging grasp to the size and shape of the apple, tilting the apple around its stem, and carefully placing it among the other apples. All these steps should be largely be performed by touch, as sight is often occluded by leaves, branches and other apples. Applying too much force or applying the forces in an incorrect manner will result in damaged apples or a damaged tree.

Conventional position-controlled manipulators with limited degrees of freedom (DOFs) are incapable of completing such tasks. Taking inspiration from the way in which the human hand performs these tasks, roboticists have developed robotic hands with large numbers of sensors, joints, and actuators [1] (e.g., the *Utah/MIT Hand* [2], the *Gifu Hand II* [3], and the *DLR Hand II* [4]). These features allowed them to sense external forces, and adjust their behavior accordingly (see, for example, the adaptive control strategy proposed by Craig et al. [5] and the impedance control proposed by Hogan [6]). Despite the enormous complexity of some of these robotic hands in terms of design and control, they have not come close to the effectiveness of the human hand in performing these tasks. Moreover, these robotic hands are very costly and often lack robustness.

Figure 1.1: Picking an apple as an example of a dexterous manipulation task performed by the human hand - *Photo Credits: Human hand is picking an apple from apple tree by Laertgreen, https://www.shutterstock.com/video/clip-7906141-human-hand-picking-apple-tree, License at http://creativecommons.org/licenses/by/2.0.*

In an attempt to reduce the complexity of these manipulators while maintaining their ability to adjust to their environment, research in robotics has explored the use of morphological computation, in which at least some aspects of the control are outsourced to the body of the robot. Examples of developments using this approach include underactuated manipulators in which the number of actuators is lower than the DOFs [7] (e.g. the *BarrettHand grasper* [8] and the *Delft Hand 2* [9]), or the addition of an elastic component in between the actuator and the load (known as series elastic actuators [10]). Nevertheless, these manipulators still rely on a large number of rigid components such as bearings, joints, metal links, actuators, sensors, springs, and gears. The almost exclusive use of rigid materials is in stark contrast to grasping mechanisms in natural systems, in which soft tissue plays a crucial role in realizing adaptive and compliant grasping behavior.

This observation has inspired attempts to construct manipulators, and even complete robots, from soft materials in order to increase their ability to deal with unpredictable environments. This field of research is known as soft robotics [11]. In this dissertation, the term soft robots is used to refer to systems that are capable of autonomous behaviour, and that are primarily composed of materials with moduli in the range of that of soft biological materials, following the definition by Rus and Tolley [12]. Many soft robotic manipulators with a range of different actuation, sensing, and fabrication methods have been developed over the past years [13]. However, several challenges in the use of soft materials in robotics must be overcome in order to to enable soft robots to perform dexterous manipulation tasks.

The purpose of this research is to enable the use of soft robots for the automation of dexterous manipulation tasks.

1.2 Scope of the research

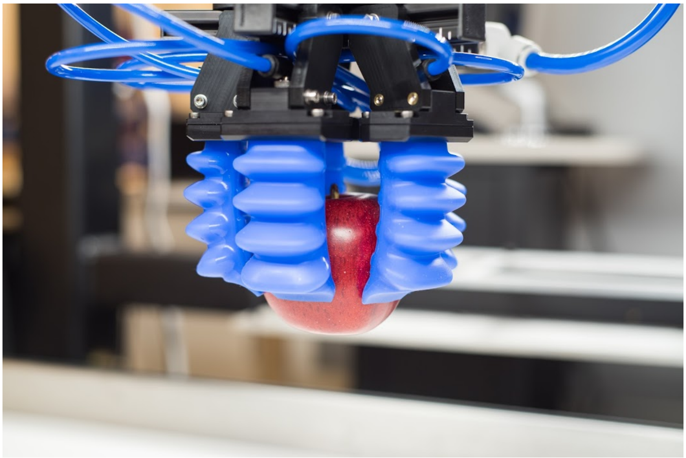

Figure 1.2: State of the art soft robotic manipulators used for pick-and-place tasks - *Photo Credits: softroboticsinc.com*

Although soft robotics might be the key to automation of dexterous manipulation tasks, the current commercially available soft grippers (see Figure 1.2) are only capable of performing simple pick-and-place tasks with open-loop control due to a lack of perceptive capabilities. Perception is essential to the realization of autonomous and intelligent robots. As external (vision-based) perception is usually not sufficient in unpredictable and complex environments, a sense of self-movement and body position, known as proprioception, is needed to move from open-loop control to closed-loop control. Proprioception is a relatively simple problem for conventional robots with rigid members and discrete joints, as the body position can be easily reconstructed using the information from encoders in the robots' joints. However, it is a very challenging problem for soft robots with virtually infinite DOFs and no suitable off-the-shelf sensors. This research addresses the challenges in building soft robotic manipulators with proprioception. It thus paves the way for the development of closed-loop control algorithms for soft robotic manipulators and, eventually, for the development of soft manipulators capable of executing dexterous manipulation tasks.

The research objective is to develop a systematic approach to building soft robotic manipulators with proprioception in order to enable the development of closed-loop control algorithms for dexterous manipulation tasks.

1.3 Research Questions

The key challenges in the realization of proprioception in soft robotic manipulators are integrated design, capturing deformation, reconstruction and restraining superfluous degrees of freedom. These challenges will be explained and transformed into research questions.

1.3.1 Integrated Design

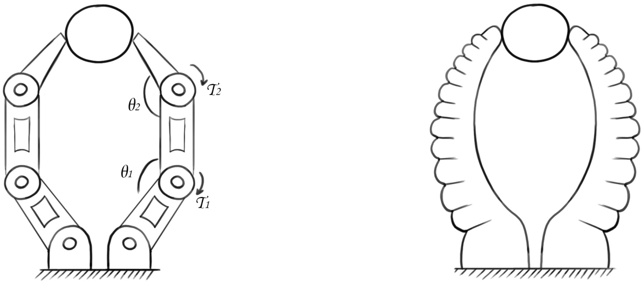

Figure 1.3: Challenge of integrated design. A rigid robotic manipulator is assembled from discrete links, actuators and sensors, whereas the body, actuators, and sensors of soft robots are intertwined and embedded throughout the entire body of the robot. - *Illustration by M.A. Sandoval Martinez*

Rigid robotic manipulators are typically assembled from many off-the-shelf components that can be designed mostly independently from each other. For example, the designer of the robot's joint motors does not need to be aware of the force sensors used in the fingertip of the manipulator. The desired interaction between the components can be programmed after the construction of the robot is complete. Such an approach is not possible for soft-bodied robotic manipulators that have continuously deformable bodies (see Fig. 1.3. The actuators and sensors of soft robots are heavily intertwined and distributed throughout the entire body of the robot. To achieve a desired behavior, the design and manufacturing of the sensors, actuators, and structure of the soft robot must be considered in concert. Key to facilitating such an integrated design approach for soft robots with proprioception is the composition of a set of compatible actuation, sensing and manufacturing techniques that are flexible enough to be altered in unison without further complications. For example, a small change in the design of the actuator should not require a complete redesign of the sensors or reconsideration of the manufacturing technique. Instead, the set of actuation, sensing, and manufacturing techniques should have sufficient flexibility to accommodate these changes in a streamlined way. The first research question is therefore defined as:

RQ1 *What combination of actuation technique(s), sensing technique(s), and fabrication technique(s) for soft robotic manipulators can facilitate an integrated design approach to design the behavior of soft robotic manipulators with proprioception?*

1.3.2 Capturing Deformation

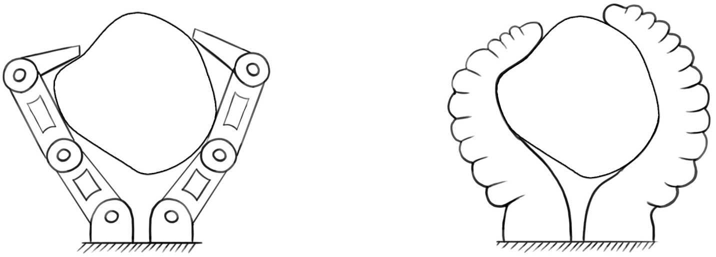

Figure 1.4: Challenge of capturing the deformation of a soft robot. The deformation of a rigid manipulator occurs only at the joints, whereas the deformation inside a soft manipulator occurs throughout the entire body. - *Illustration by M.A. Sandoval Martinez*

Rigid robotic manipulators usually have a limited number of DOFs with an actuator and a sensor for every DOF. Most deformations in rigid robots occur very locally. For example, a rigid robotic manipulator commonly has a joint motor and an encoder to control and measure a rotation around a single axis. In contrast, soft robots have virtually infinite DOFs. A single actuator can create deformations throughout the entire robot. Not only are these deformations dependent on the actuation input, but they also depend on the external forces that are acting on the robot (see Fig. 1.4). Therefore, sensors for soft robots should be able to capture and distinguish between a very large number of possible robot positions. As soft robots deform throughout their entire body, sensors for soft robots should be capable of withstanding these deformations as well without impeding the robots movement. No off-the-shelf sensors meet these requirements. Thus, a major challenge in realizing proprioception in soft robots is the development of a sensing method that does meet these requirements, as addressed in the following researc question:

RQ2 *How to endow soft actuators with embedded sensors that accurately capture the actuator's deformed shape?*

1.3.3 Reconstruction

Rigid robotic manipulators are commonly composed of a chain of rigid bodies connected by joints with encoders. Therefore, the orientation and position of the manipulator can be easily computed as a function of the joint variables. A simple model suffices to translate the encoder output pulses to the speed and position of a joint. Due to the virtually infinite DOFs in soft robots, on the other hand, the relationship between the sensor data and the orientation and position (or shape) of the soft robotic manipulator is much more complex (see Fig. 1.5).

This complexity makes it challenging to calibrate the sensors and reconstruct the shape of the robot from this data. The relationship between the sensor data and the soft robot shape is often complicated and difficult to model. Therefore, a calibration step is required. Moreover, a simplified model of the soft robotic manipulator is necessary to reduce the number of parameters needed to describe the robot's shape. This model should balance accuracy with computational efficiency for real-time control and visualization. The third research question is defined as:

RQ3 *How to reconstruct the shape of soft robots in real time?*

1.3.4 Restraining Superfluous Degrees of Freedom

Besides capturing and reconstructing the deformation of soft robots, it is important to prevent undesired deformation from occurring in the first place. In contrast to rigid robots, in which every DOF of the robot has been added with a specific purpose, the desired DOFs of soft robots are most often accompanied

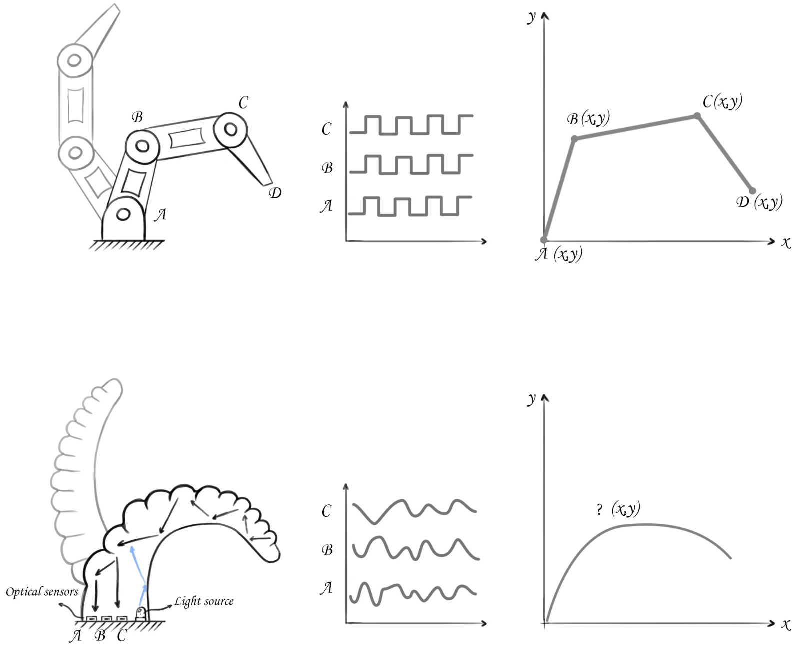

Figure 1.5: Challenge of soft robot reconstruction. Whereas the position of a rigid robot can be easily reconstructed from the encoders in the joints, the signals that capture the deformation of soft actuators are generally much harder to interpret. Moreover, it is challenging to find a small number of shape parameters that can accurately describe the large variety of shapes that the soft robot can assume. - *Illustration by M.A. Sandoval Martinez*

by DOFs that are not helpful or even worsen the performance of the robot (see Fig. 1.6). Before allocating resources to measure and reconstruct these superfluous DOFs, it is meaningful to take a step back and explore whether these DOFs can be restrained. Not only would this improve the performance of the robot, but it would also simplify the problem of capturing the deformation of the soft robot, calibrating and reconstructing the soft robot, and controlling the soft robot. Therefore, the fourth research question is defined as:

RQ4 *How to restrain superfluous degrees of freedom in soft robotic manipulators?*

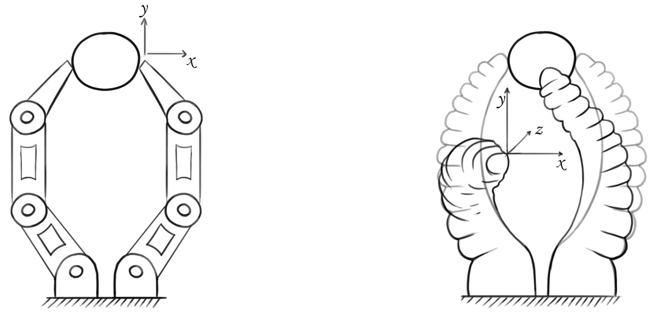

Figure 1.6: Challenge of superfluous degrees of freedom. The motion of a rigid manipulator is restrained to occur in-plane only, resulting in a steady grasp. The soft manipulator can move out-of-plane resulting in a failed grasp - *Illustration by M.A. Sandoval Martinez*

1.4 Research Cycles and Thesis Organization

This thesis is organized around five research cycles (RCs), each addressing one or more of the research questions (RQs) defined in Section 1.3. An overview of the organization of the thesis is shown in Fig. 1.7. Each research cycle is discussed in a separate chapter (Chapters 2–6), preceded by this introduction (Chapter 1) and followed by a discussion (Chapter 7) and conclusion (Chapter 8). The chapters that discuss the findings from the research cycles comprise of a collection of conference articles, journal articles, and book chapters. After an initial exploration into building a manipulator with proprioception in RC1, two lines of research are performed in parallel. RCs 2–4 focus on the challenges regarding the realization of accurate proprioception. Chapters 3–5 focus on the capturing of deformation, calibration, and reconstruction respectively. However, as each chapter is a self-contained publication, some overlap between these topics exists across the different chapters. RC5 focuses on the development of a more suitable actuator for manipulation tasks through restraining superfluous DOFs. The purpose of the individual research cycles will be discussed in more detail below.

RC1 The first research cycle served as an exploration into the integrated design and fabrication of soft robotic actuators and sensors with desired behavior (RQ1). Additive manufacturing was used to print flexible air

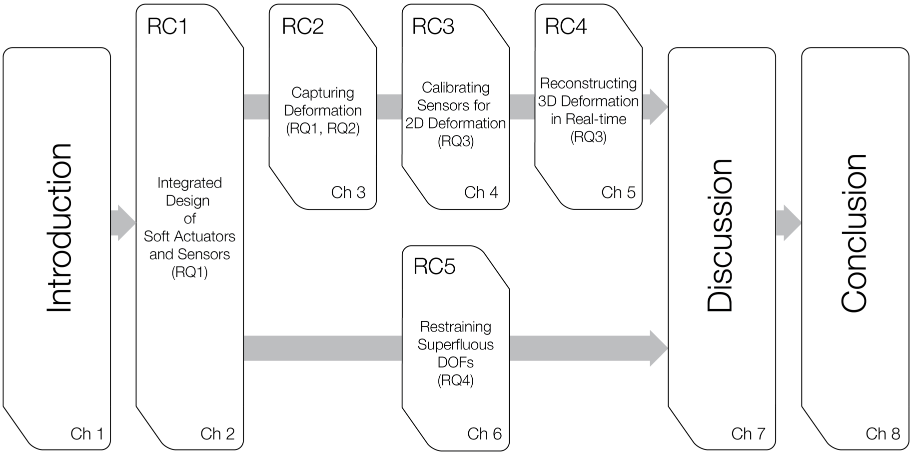

Figure 1.7: Overview of the research cycles, research questions, and chapters of this thesis

chambers that served either as pneumatic actuators (by inflating them with air), or as sensors (by measuring changes in air pressure inside the chamber upon deformation). The freedom in designing the shape of the air chambers was exploited to realize a range of different motions, forces and sensing behavior. Finally, the actuators and sensors were combined into a soft robotic hand that can be 3D-printed in one go. Through a simple control system, the soft robotic hand is capable of shaking a human hand in an interactive way: the robotic hand senses how hard the hand is squeezed and squeezes back accordingly.

RC2 The soft robotic manipulator developed in RC1 was a step towards designing soft robotic manipulators with desired behavior. However, the manipulator's actuators still lacked perception. The air-pressure-based deformation sensing that was applied in research cycle one has several limitations. First, measuring the pressure inside an air chamber only provides a single signal. As there are many soft robot shapes for which a certain pressure can be realized, this method is incapable of encoding the large number of DOFs in soft robots into unique signals. Second, air-pressure-based sensing cannot be used for closed-loop control of actuators that are controlled by air pressure. In RC2, an optical sensing method for pneumatic actuators was developed. The sensing principle is based on the use of color sensors in combination with 3D-printed color patterns inside the air chamber of soft pneumatic actuators. It was demonstrated that this method is capable of encoding small changes in the shape of soft actuators that have a large number of DOFs. Thus, this research cycle addressed RQ2. It was also demonstrated that the proposed sensing method is compatible with the use of additive manufacturing of soft pneumatic actuators. Hereby, the development of this sensing method also completes the set of techniques that facilitates an integrated design approach to designing the behavior of soft robotic manipulators with proprioception (RQ1).

RC3 In RC2, the signals from the sensors were first merged to a single bending metric and then calibrated to the angle of a single bellow on the actuator. This is an overly simplified way of representing the shape of soft actuators that have many more DOFs. Moreover, the calibration was performed during unobstructed bending and would therefore not yield reliable results when the actuator was interacting with objects. The aim of RC3 was to address the problem of calibration. As the relationship between the shape of the actuator and the sensor signals cannot be easily modeled analytically, a machine learning-based approach was adopted to calibrate the sensors. First, a vision-based system was used to capture the position of a number of markers on the soft actuator while it was interacting with objects. Next, a machine learning model was trained using the raw sensor data as inputs, and the marker coordinates as outputs. Through this approach, a set of points on the robot could be accurately predicted from the sensor data, even when the soft actuator was interacting with objects. This calibration provided the basis for the reconstruction method (RQ3) discussed in RC4.

RC4 In RC3, it was demonstrated that the captured sensor signals can be used to accurately predict points that are located on the robot. However, this collection of points needs to be converted to a robot representation that is useful for real-time visualization as well as closed-loop control. To this end, the captured marker coordinates are converted to shape parameters that are used for training the machine learning model. The shape parameters that are predicted by the machine learning model can be used to reconstruct the shape of soft robots in real time (RQ3). The calibration procedure in RC3 was limited to static soft robot postures with two-dimensional bending deformation. In this research cycle, the sensing, calibration, and reconstruction were demonstrated for soft robots composed of multiple actuators undergoing dynamic three-dimensional deformation. With a much larger soft robot workspace, many more training samples are needed to train the machine learning model. A motion capture system was deployed to rapidly collect the dynamic data.

RC5 This research cycle addresses RQ 4. In RC1, it was demonstrated that a range of different actuation behaviors could be realized by modifying the shape of the air chambers. However, the fingers of the soft robotic hand had a tendency to slip as a result of out-of-plane deformation. In soft robotic manipulators, this out-of-plane deformation is a major cause of failed grasps. In this research cycle, the problem of out-of-plane deformation in soft pneumatic actuators was demonstrated, and a method for reducing the out-of-plane deformation was developed. This was achieved through embedding a structure inspired by compliant mechanisms in the 3D-printed soft actuator. This structure reduces the out-of-plane deformation without significantly increasing the in-plane bending stiffness.

2

Integrated Design of Soft Actuators and Sensors: An Exploration

This chapter explores the integrated design and fabrication of soft robotic actuators and sensors with desired behavior. Additive manufacturing is used to print flexible air chambers that serve either as pneumatic actuators (by inflating them with air) or as sensors (by measuring changes in air pressure inside the chamber upon deformation). The freedom in designing the shape of the air chambers is exploited to realize a range of different motions, forces, and sensing behavior. Finally, the actuators and sensors are combined into a soft robotic hand that can be 3D-printed in one go. Through a simple control system, the soft robotic hand is capable of shaking a human hand in an interactive way: the robotic hand senses how hard the hand is squeezed and squeezes back accordingly.[1]

---

[1] This chapter is published as: **R. B. N. Scharff**, E. L. Doubrovski, W. A. Poelman, P. P. Jonker, C. C. L. Wang, and J. M. P. Geraedts, “Towards behavior design of a 3D-printed soft robotic hand”, in *Soft Robotics: Trends, Applications and Challenges: Proceedings of the Soft Robotics Week, April 25-30, 2016, Livorno, Italy*. Springer International Publishing, 2017, pp. 23–29. Note: a few small corrections and/or clarifications have been made to the original published text.

2.1 Introduction

Pneumatic actuation is one of the two most-used actuation techniques in soft robots [12]. This type of actuation is often realized through the inflation of channels in elastic material. These actuators are promising in soft robotics since (1) they are under-actuated and compliant, (2) they can be free of internal electronics and electric components, and (3) their performance can be tuned through the morphology of the actuated segment [15]–[17]. These features provide a significant benefit in applications such as soft pneumatic hands [18], orthotics [19], and locomotion [20]. Previous researchers mainly used molding techniques to fabricate silicone soft robots [17], [20], [21]. However, the constraints of the molding processes limit the design freedom. As a result, in existing approaches actuators are usually oriented in the same plane or fabricated separately and later assembled into a functional structure. *Additive Manufacturing* (AM), or 3D printing, is a collection of digital fabrication processes that build up objects by adding material layer upon layer. AM has been used to integrate multiple actuators [22], [23] or air pressure sensors [24] with structural components. In literature, an advanced design method was developed to design the deformation elasticity of structures fabricated by AM [22]. Nevertheless, little attention was paid to the methodology of customizing the behavior of each specific actuator and sensor within a soft robotic product. This work presents a case study in which multiple air pressure actuators, sensors, and structural components are integrated in a single body product using the AM process *Selective Laser Sintering* (SLS). To show the possibility of designing human-like behavior, an interactive setup was made realizing a handshake between a user and the hand. The air pressure-based robotic hand comprises eight actuators and two sensors without any internal electronics. The hand measures the force that is exerted upon it and squeezes back accordingly, adapting itself to the user's grip. For each part of the hand, the behavior was customized based on a given volume and function. The main technical contribution of this work is the integration of air pressure actuators, air pressure sensors and structural components that are designed for the desired behavior of this specific volume within the product.

2.2 Design of Soft Robotic Hand

We simplified the complexity of the human hand and subdivided it into parts with a specific function as actuator or sensor. The carpometacarpal joint of the

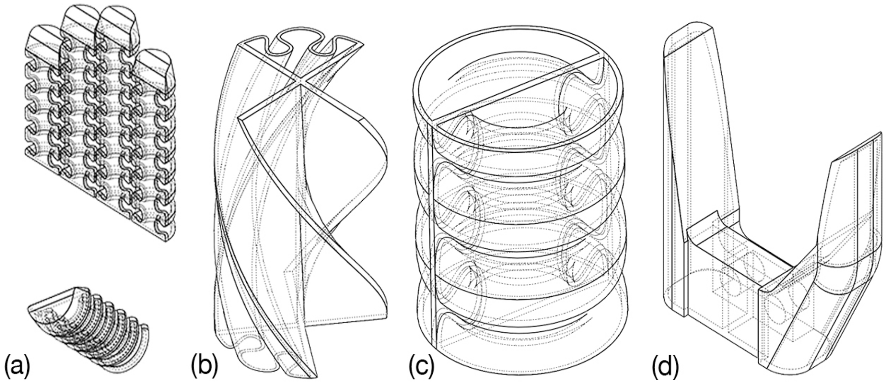

Figure 2.1: An illustration of different parts used in our design — from left to right, (a) bending actuators, (b) rotational actuator, (c) bidirectional actuator and (d) sensing air chambers

thumb is fixed in a position suitable for shaking hands. The design of our soft robotic hand consists of four different parts (see Fig. 2.1 for an illustration), including (1) bending actuators, (2) a rotational actuator, (3) a bidirectional actuator, and (4) sensing air chambers, all shown and discussed below. They are designed to mimic the behavior of a human's hand.

2.2.1 Bending Actuators

The principle of a pneumatic bending actuator is based on pressurizing an air chamber formed by an inextensible bottom layer and an extensible top layer (see also Fig. 2.1a). The bending range can be improved by creating a more S-shaped curve of the bellow, whereas the exerted force at a given position can be improved by increasing the bellow's stiffness [15]. This principle was used to create the difference in behavior between the fingers and thumb. Given a designed model and fabrication constraints, the following properties influenced the design process of bending actuators; we need (1) a minimum bending range of $90°$ of the thumb (the angle measured on tip orientation) at a pressure of less than $400\ \mathrm{kPa}$, (2) a minimum bending range of $180°$ of the other fingers, to be achieved with the same pressure, (3) to maximize the exerted force of the thumb bellow, and (4) to minimize the radial expansion of the bellows.

2.2.2 Rotational Actuator

The principle of this rotational actuator was inspired by the elephant's trunk. The elephant has helical muscles in its trunk that, when contracted, cause rotation of the trunk [25]. This principle can be mimicked by sweeping a radially expanding bellow over a helical path (see Fig. 2.1b). Here, the design process is influenced by the following demands on properties; we need to (1) maximize the radial expansion of the bellow upon inflation, (2) minimize the lateral expansion of the bellow upon inflation, (3) maximize the structure's bending and axial stiffness, (4) minimize its rotational stiffness, (5) at least $45°$ of pronation to be achieved with at most $400\ \mathrm{kPa}$ pressure. Our design consists of a bellow swept over a helical path of 0.4 revolutions over a height of $70\ \mathrm{mm}$. The bellow is encapsulated between two segments of an X-profile, and the actuator has a diameter of $50\ \mathrm{mm}$.

2.2.3 Bidirectional Actuator

Two bending actuators that share an inextensible layer were used to mimic the antagonistic setup of a bidirectional actuator. Pressurizing one of the two bellows can be used to create palmar or dorsal flexion. Pressurizing both air chambers will inflate the bellows and therefore enhance the palmar and dorsal stiffness of the wrist. The following factors are considered in our design of the bidirectional actuator; we need to (1) minimize the palmar and dorsal bending stiffness, (2) maximize the radial and ulnar bending stiffness, (3) maximize the axial and rotational stiffness, (4) achieve minimal palmar flexion of $45°$ within $400\ \mathrm{kPa}$ pressure, (5) obtain minimal dorsal flexion of $45°$ with the same pressure, (6) maximize the bending stiffness upon pressurization of both actuators. Our design can be found in Fig. 2.1c. To increase the radial and ulnar bending stiffness, the inextensible layer of the double bellow is designed rectangular instead of following the curves of the bellows. The shape of the bellows is extensively curved to ensure self-collision to create extra stiffness when inflated. The actuator has a diameter of $50\ \mathrm{mm}$ and an effective height of $70\ \mathrm{mm}$.

2.2.4 Sensing Air Chambers

The principle of our sensor was inspired by the work of [24]. Squeezing an air chamber results in an increase in air pressure, which can be measured externally from the hand. Our design incorporates the following considerations; we need to (1) mimic compliance of a human hand at contact areas, (2) provide a connection structure between fingers, thumb and wrist, and (3) minimize the air volume to maximize the sensitivity. Our design is shown in Fig. 2.1d. It essentially shows the palm of the hand as base to connect wrist and thumb and two extensions of the palm at which the finger-set is attached. See also Fig. 2.3. If these extensions are squeezed towards each other they output air pressure that can be measured and electronically processed by our control system.

2.2.5 Pneumatic Control System

A *Freescale MP3V5010* sensor with a range of 0-10 kPa was used to measure the change of air pressure in both air chambers of the hand palm when people shake our soft-robotic hand. The sensed signal is then mapped to a 0-400 kPa pressure using a *Festo VPPE-3-1-1/8-6-010-E1* proportional pressure regulator to control the gripping force of the thumb and fingers. The bidirectional and torsional actuator are manually controlled using a 3/2 valve and a pressure of $100\ \mathrm{kPa}$.

2.3 Design for Manufacturing

The final design was fabricated on an SLS machine by Materialise (www.materialise.com) using the flexible polyurethane-like *TPU92A-1* material. It took 12.5 h to print our soft robotic hand. While designing the hand, the following manufacturing factors were considered:

- Wall thicknesses: A minimum wall thickness of $1\ \mathrm{mm}$ was used to prevent leakages, whereas the maximum wall thickness was limited to $10\ \mathrm{mm}$ to prevent excessive warping.
- Removal of unused material: For each air chamber, an aperture with a diameter of at least $10\ \mathrm{mm}$ was required to remove the unused material. The powder was removed by inserting a flexible cable through this aperture. This cable was guided to the end of the air chamber through its internal geometry. Therefore, all sharp edges inside the air chamber were smoothened and branched air chambers were not possible. This means every finger needed to have a separate opening for airflow.
- Fittings: The apertures for the removal of support material were used to insert G1/4 threaded push-in fittings. Therefore, the aperture diameter was determined to be $10.5\ \mathrm{mm}$ and the depth at least $10\ \mathrm{mm}$. Because of the flexibility of the material, the apertures were surrounded by a

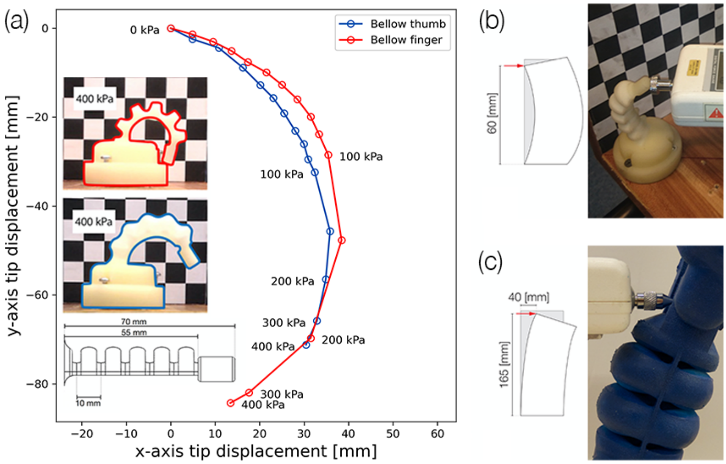

Figure 2.2: (a) Displacement of thumb design (blue) and finger design (red), (b) setup for measuring the force of the bending actuators and (c) setup for measuring the stiffness of the wrist

minimum wall thickness of 5 mm to create a secure connection with the fitting.

2.4 Results

In our design practice, various separate bending actuators of the same length and number of bellows but different shape of bellows were prototyped to find a good design for the thumb and fingers. Figure 2.2a shows the performance of the designs that were later implemented in the hand. For both bellow designs, the horizontal force was measured in the setup as shown in Fig. 2.2b. When supplying a pressure with 400 kPa, the exerted force of the thumb bellow was 7.6 N, whereas the finger bellow exerted a force of 1.8 N. The bidirectional actuator shows a bending angle of 45 ° when a pressure of 90 kPa is applied to one of the bellows (angle measured at top orientation). The stiffness of the wrist was measured using the setup as shown in Fig. 2.2c. A 0.8 N force was needed for a 40 mm displacement of the passive wrist, whereas a 2.9 N force was needed for the same displacement upon pressurization of the bellows at 400 kPa. The rotational actuator achieved a 45 ° pronation at a pressure of 60 kPa. The final design of our soft robotic hand by integrating all these actuators, sensors and structures can be found in Fig. 2.3.

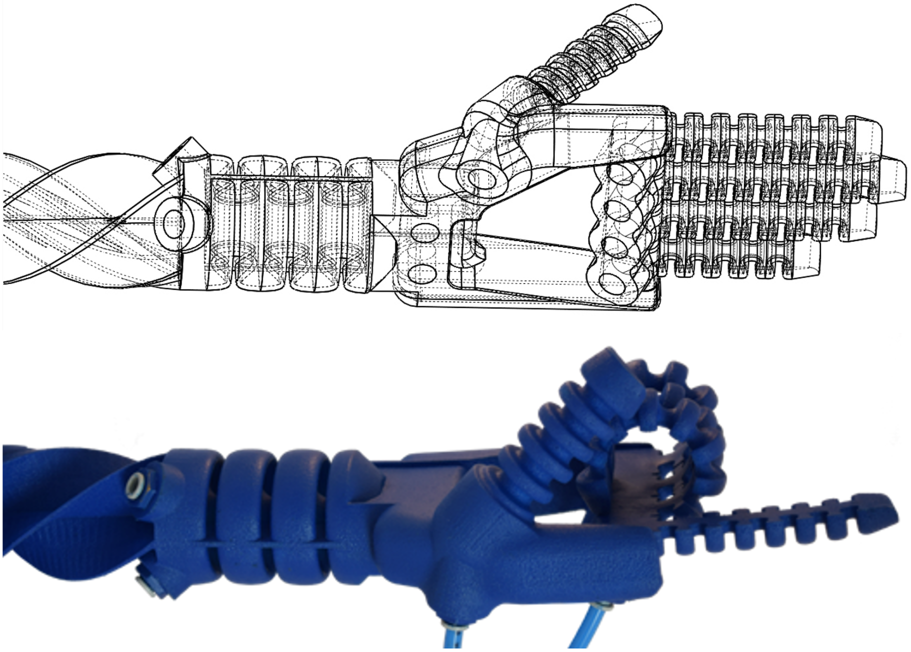

Figure 2.3: The final integrated design of our soft robotic hand, the performance of which can be found in video: https://youtu.be/AdMhkIM4hwA

2.5 Conclusions and Future Work

This work shows that the design of a set of behaviors in soft-robotic products does not have to be limited to making use of existing components. In fact, these behaviors can be deeply embedded in the integral design of a robot's actuators, sensors and structures. We showed that it is possible to design bending actuators, rotational actuators, bidirectional actuators, and sensing air chambers using mono-material SLS, and create a robotic hand with it for the purpose of human-machine interfacing, in this case for interactively shaking hands. Since the hand was created using mono-material AM, the design freedom was limited because differences in extensibility had to be created through designing the shape of the bellow's walls. In contrast, when using multi-material in AM, relative differences in behavior can also be created through compositions of complex structures of both rigid and soft materials. Thereby, a desired behavior could be addressed more easily - see [26] for an example.

3

Capturing the Deformation of Soft Robots

The soft robotic manipulator developed in Chapter 2 represents a step towards designing soft robotic manipulators with desired behavior. However,the manipulator's actuators still lack perception. The air-pressure-based deformation sensing that was applied in RC1 has several limitations. First, measuring the pressure inside an air chamber only provides a single signal. As there are many soft robot shapes for which a certain pressure can be realized, this method is incapable of encoding the large number of degrees of freedom in soft robots into unique signals. Second, air-pressure-based sensing cannot be used for closed-loop control of actuators that are controlled by air pressure. In this chapter, the development of an optical sensing method for pneumatic actuators is described. The sensing principle is based on the use of color sensors in combination with 3D-printed color patterns inside the air chamber of soft pneumatic actuators. It is demonstrated that this method is capable of encoding small changes in the shape of soft actuators that have a large number of degrees of freedom. It is also demonstrated that the proposed sensing method is compatible with the use of additive manufacturing of soft pneumatic actuators. Thus, the development of this sensing method also completes the set of techniques that allow for an integrated design approach to designing the behavior of soft robotic manipulators with proprioception.[1]

---

[1] This chapter is published as: **R. B. N. Scharff**, R. M. Doornbusch, X. L. Klootwijk, A. A. Doshi, E. L. Doubrovski, J. Wu, J. M. P. Geraedts, and C. C. L. Wang, "Color-based sensing of bending deformation on soft robots", in *2018 IEEE International Conference on Robotics and Automation (ICRA)*, 2018, pp. 4181–4187. Note: a few small corrections and/or clarifications have been made to the original published text.

3.1 Introduction

Sensors are widely used in robotic systems to provide feedback to achieve precise control of operations. However, the compliance of soft actuators precludes the use of many conventional sensors such as encoders, metal/semiconductor strain gauges, and inertial measurement units for proprioception purposes [12]. As soft robots can deform in all directions throughout their entire body, sensors should be able to detect these unpredictable and large deformations. Moreover, ideal sensors for soft robots should be bendable and/or stretchable, and should have little influence on the performance of actuators. No off-the-shelf sensor meets these requirements.

3.1.1 Overview

This work presents a novel color-based sensing approach to provide feedback for active position control of soft pneumatic actuators. In these actuators, pressurized air is used to inflate air chambers. The geometrical asymmetry in the design or constituent materials drives the shape to deform in a desired way [12]. For example, bending can be realized through pressurization of an air chamber with an extensible top layer and an inextensible bottom layer. The basic idea of our deformation sensing approach is to translate the elongations that occur in the extensible parts of soft actuators into a measurable change of color ratios captured by a color sensor. This is achieved through flexible multi-color structures that can be easily fabricated and integrated in or onto soft actuators through multi-color *Additive Manufacturing* (AM).

To interpret the raw RGB values obtained from the electric sensor and correlate them to the level of bending deformation, the signals are analyzed and transformed into a bending metric (κ). This metric can serve the purpose of controlling the deformation in a feedback control loop. Details of the signal analysis and calibration can be found in Section 3.3.

For example, in the actuator shown in Fig.3.1, the RGB values are captured by an electronic color sensor placed near the root of the actuator (indicated by a red arrow in Fig. 3.1(a) and (b)). It can be observed that, under a constant air pressure, the bending deformations without external force (a) and with an external force (b) are clearly different. Based on the difference in κ values, the air pressure is adjusted until κ matches the value of κ for the reference bending (a). Fig.3.1(c) and (d) show that visually indistinguishable deformations corresponding to (a) can be achieved. Notice that different external forces are

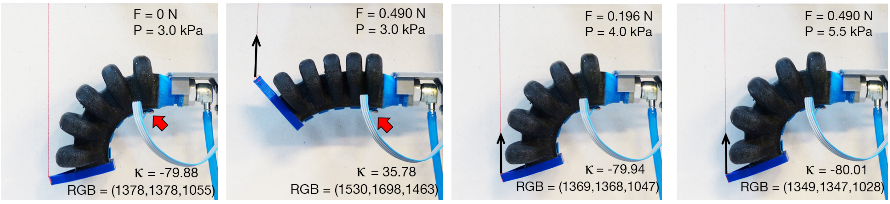

(a) **(b)** **(c)** **(d)**

Figure 3.1: An example to demonstrate the function of color signals for sensing deformations. (a) The deformation of a soft actuator under an air pressure of $3.0\,kPa$ serves as a reference. (b) The deformation is changed when an external force is applied to the tip of the soft actuator (indicated by the black arrow), under the same air pressure. The bending metric κ, calculated from the Red-Green-Blue (RGB) values measured by the color sensor, enables an accurate control of the deformation. Different external loads are applied in (c) and (d), the same deformation to (a) is achieved by increasing the air pressure until obtaining the same signal κ.

applied in (c) and (d), while they both have the same κ value. The experimental results of our sensing approach are further discussed in Section 3.4.

3.1.2 Related work

If the geometry of a task is known as a priori, the curvature of an actuator can be controlled through the applied pressure and mechanical programming (e.g., [14], [28]). For operations in complex and unstructured environments, mechanical programming becomes insufficient and sensors are needed.

Exteroceptive measurement of curvature can be achieved through a visual tracking system (e.g., [18], [29], [30]). However, proprioceptive sensing approaches have the potential to create more compact sensing systems and further improve the autonomy of soft robots. This requires sensors that can be integrated on soft actuators, such as draw wire encoders [31], resistive sensing using embedded conductive ink [32], [33], and highly flexible capacitive sensors built from conductive fabrics and silicone [34] or by depositing aluminum and silver layers on elastomer sheet [35], [36]. A more complete overview of sensing principles for soft actuators can be found in [37] and [13].

Attempts to further integrate sensors in soft actuators have been made through integration of resistive flex sensors or magnetic curvature sensors [38] in the inextensible layer during the fabrication process. Integration of sensors in other parts of the actuators requires the sensors to be stretchable as well. Zhao et al. demonstrate curvature control through integration of stretchable optical waveguides throughout an actuator in [39], [40]. Integration of *EGaIn* sensors in the dorsal surface of an actuator has been demonstrated in [41].

As the high flexibility of soft robots allows for many different deformations, most of the aforementioned work can use multiple sensors to measure the curvature more accurately or make a distinction between different types of deformation. As not all deformations are equally important, Wall et al. [42] developed a method to find an effective layout from a set of sensors. In this chapter, we only study the functionality of a single sensor based on color signals.

3.1.3 Contribution

The technical contribution of our approach is twofold.

- A novel sensing principle integrating multicolored structures to serve as signal generators and thus provide feedback for deformation control.
- Signal processing and calibration methods for transforming raw color values into a meaningful bending metric.

Our sensing approach is contactless, easy-to-integrate, cost-effective and has a low power-consumption. As the measurements directly link to the geometry of the color printed 3D structures, our approach is less affected by external loading and time-related material response such as elastic hysteresis.

3.2 Signal Generator

Two embodiments of color-change generating structures are presented in this work: an external and an internal signal generators. We envision usage of the first embodiment in soft actuators where elongation of the air chamber is mainly based on material strain[2] (e.g. [43]), whereas the second embodiment is especially useful for actuators where elongation is mainly realized through bellow-like geometries (e.g. [17]). Note that we use two contrasting colors instead of black-and-white patterns to enable filtering out intensity fluctuations that occur due to the changing structure, as explained in Section 3.3. The use of color also allows us to further extend the signal generators described below by embedding more colors in the structures, which generates more color patterns and therefore is able to sense more complicated deformations.

---

[2] Although we test the external generator on a bellow-based pneumatic actuator.

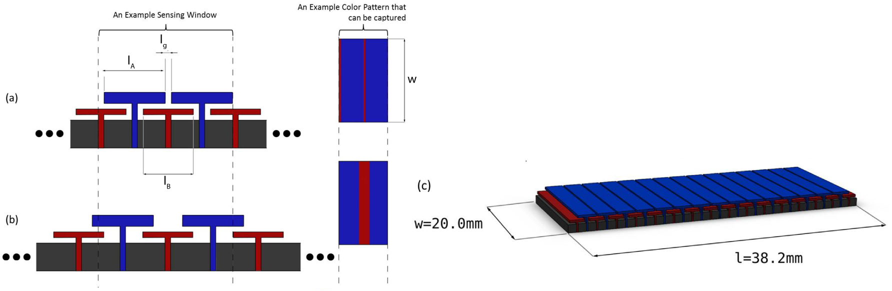

Figure 3.2: Side view of the structure for an external signal generator in a released position (a) and a stretched position (b). The dimensions for T-components are $l_\mathrm{A} = 2.2\,\mathrm{mm}$, $l_\mathrm{B} = 1.8\,\mathrm{mm}$, and $l_\mathrm{g} = 0.2\,\mathrm{mm}$. Sixteen pairs of such T-components are periodically used in our design (c).

3.2.1 External signal generator

The first embodiment of our approach is a structure composed of T-shaped components with alternating height and color, embedded onto a highly stretchable and light-absorbing material (see Fig. 3.2). A color sensor captures signals from the top-view of the structure. When being stretched, the lower T-component become less occluded by the higher components – i.e., having more area observed through the sensing window so that the ratio of colors changes. The measurement of this color ratio is used to indicate the amount of strain.

The structure is divided into a number of periods, with a period defined as the smallest repeating structure:

$$p = l_\mathrm{A} + l_\mathrm{g} + \Delta l. \tag{3.1}$$

Here l_A is the length of a high T-shaped component, l_g is the initial gap size, and Δl is the change in length of the non-occluded part of a low T-shaped component l_B upon stretching. Considering that the width w of a structured strip is constant, the ratio of areas exposed to the sensing window can be calculated by

$$r_\mathrm{A} = \frac{l_\mathrm{A}}{p}, \quad r_\mathrm{B} = \frac{l_\mathrm{g} + \Delta l}{p}, \tag{3.2}$$

for the ratio of the high T-shaped component A and low T-shaped component B respectively. Note that this is only valid when $\Delta l \leq l_\mathrm{B} - l_\mathrm{g}$; otherwise, the flexible base material will be exposed to influence the quality of color signal. Strain in the flexible base material can now be obtained as:

$$\epsilon = \Delta l / (l_\mathrm{A} + l_\mathrm{g}). \tag{3.3}$$

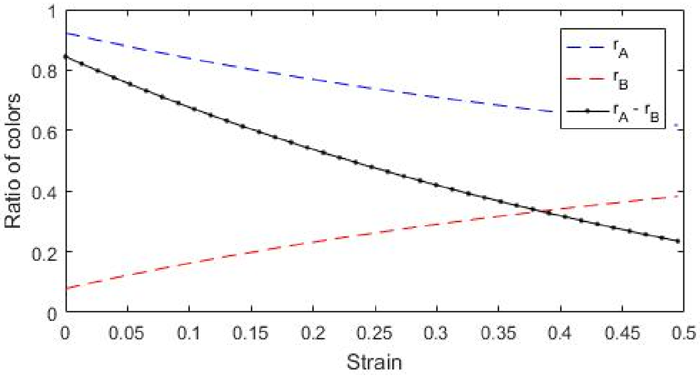

Figure 3.3: The ratios of the exposed surface area of A and B components (i.e., $r_A(\epsilon)$ and $r_B(\epsilon)$) and their difference are all monotonic functions of the strain presented on the belt. The curves are generated by the structure shown in Fig.3.2.

The relation between the color ratios and the strain are plotted in Fig.3.3 for the structure given in Fig.3.2. It can be found that the ratio difference $((r_{\mathrm{A}}(\epsilon) - r_{\mathrm{B}}(\epsilon)))$ is monotonic and also very sensitive to the strain presented on our color signal generator.

Note that the size of a sensing window is not taken into account here. Fluctuations of the signal presented in Fig.3.3 will be generated when a non-integer amount of periods is visible within the sensing window. This will be further discussed in Section 3.3. As we aim to design a structure that can generate a consistent signal regardless of where the color sensor is placed, this error is minimized by minimizing the length of a period.

3.2.2 Internal signal generator

The second embodiment of our design is a color signal generator integrated into an existing design of a soft pneumatic actuator. This is realized by colorizing different regions of an Ω-shaped bellow in different colors, as illustrated in Fig.3.4. A color sensor is embedded in the inextensible layer of the bending actuator. Upon pressurization of the air chamber, the inflation of the bellows leads to a larger area of the originally occluded color being exposed to the window of the color sensor. As a result, the measurement of the sensor changes accordingly. The same sensing strategy can be applied to bellow-based pneumatic actuators of different shapes and dimensions. Although the measurements are strongly dependent on the particular design of an actuator,

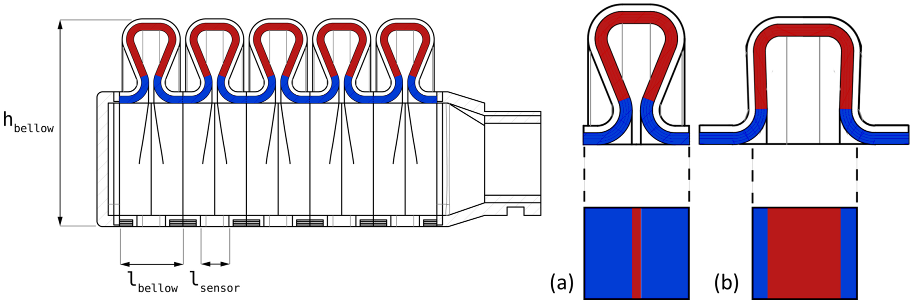

Figure 3.4: An illustration of a bellow before (a) and after (b) being pressurized. The pattern of colors that can be captured through the sensing window is also shown at the bottom. (b) shows a larger red region can be 'seen' through the window in the presence of a large bending deformation. In this example, the dimensions of a bellow are $l_{\text{sensor}} = 5.1\,\text{mm}$, $l_{\text{bellow}} = 11.3\,\text{mm}$ and $h_{\text{bellow}} = 37.0\,\text{mm}$.

a general calibration procedure as discussed in the next section of this chapter can be conducted to link the measurements of a color sensor to the level of bending deformation presented on the bellows.

3.2.3 Materials & Fabrication

The hardware realization of the color-change generating structures is shown in Fig.3.5.

The external signal generator is attached on top of an existing soft pneumatic actuator. One end of the belt is mounted at the root of the actuator, while the other end is attached to the tip of the bellow. The color sensor is also placed at the root of the actuator. When the actuator is bent, the structure elongates underneath the sensing window to generate color signals.

For the internal signal generator, miniaturized sensors were designed and mounted onto plugs. These plugs are inserted in the inextensible layer of the actuator. The number of sensors and the location of the sensors can be easily adjusted in our design. Our experimental results are obtained by a single sensor mounted at the root of the actuator. The outside of the plug and inside of the plug opening are built from rubber-like photopolymer (Agilus 30) that seals the air chamber. No air leakage was observed upon full actuation.

The embodiments of our design are fabricated on a Stratasys Objet 350 Connex3 Multi Material 3D printer, which uses Material Jetting technology and can print combinations of up to three different building materials together

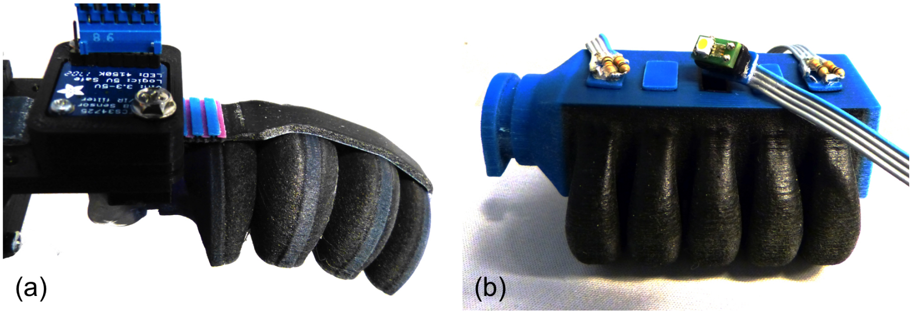

Figure 3.5: Hardware realization of our color-based deformation sensing approach on 3D printed soft actuators in an external way (a) and an integrated manner (b). For illustrating the flexibility of our design, three sensors are presented in (b) although all the experimental results presented in this chapter are obtained by placing a single sensor at the root of the actuator.

with a water soluble supporting material. All examples shown in this chapter are printed using a combination of the flexible Agilus 30 Black, the rigid VeroCyan and the rigid VeroMagenta. Note that 3D printing materials with pure blue or red colors are not available.

The Agilus 30 Black has an elongation of $220 \sim 270\%$ at break and a tensile strength of $2.4 \sim 3.1\mathrm{MPa}$ – as documented by Stratasys. The RGB values of the VeroCyan (VC) and VeroMagenta (VM) materials are $RGB_{\mathrm{VM}} = (166, 33, 98)$ and $RGB_{\mathrm{VC}} = (0, 93, 127)$ respectively. Brunton et al. [44] have characterized the VeroCyan and the VeroMagenta materials as highly translucent. We find that VeroMagenta has an even higher translucency than VeroCyan. Since translucency of the upper layer will decrease the color difference upon stretching, the VeroCyan material was chosen for the higher T-components in the external design and for the region near the 'neck' of air chambers in the integrated design.

3.3 Signal Analysis and Processing

This section starts with an analysis of the signals that are captured by our sensing approach, and then proceeds to a method for converting RGB values into a deformation metric κ. Remaining fluctuations in the signal is explained by simulations. After that, we introduce the calibration method.

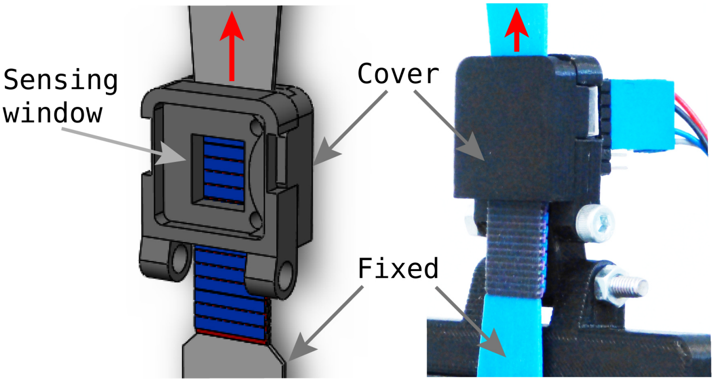

Figure 3.6: The measurement setup for testing the sensor belts. The stretching direction is indicated with a red arrow.

3.3.1 Raw-data of color signal

A TCS34725 light-to-digital converter with an integrated white LED is used for the measurement of RGB colors. A miniaturized version of this sensor was designed to be mounted on the sensor plugs of the internal signal generator (see Fig.3.5(b)). For both embodiments, we use an integration time of $154\,\mathrm{ms}$ and 1X gain setting to obtain different RGB values from the converter when different color patterns are exposed to the sensing window. The TCS34725 sensor returns four values for each exposure, namely the R-, G-, B-components of color plus the light intensity.

To capture a set of raw data to conduct the signal analysis, we clamp a sample of our external signal generator onto a tensile testing machine. The sensor is then placed in a case having a window with dimensions $10\,\mathrm{mm} \times 12\,\mathrm{mm}$ (see Fig.3.6). The distance between the belt and the sensor is $4\,\mathrm{mm}$, and the sensing window is positioned at the boundary of the second period on the belt. A light absorbing cover is attached to the case of sensing to shield the belt from environmental light. Note that we use the same sensing window for the external sensing belt mounted on the bending actuator (see Fig.3.5(a)). The tensile testing machine moves the upper clamp upwards to stretch the belt in steps of $0.5\,\mathrm{mm}$ while the colors are measured for each step. The color sensor is connected to the lower clamp and remains fixed.

Figure 3.7 shows a typical RGB measurement of an external signal generator with a VeroCyan top and a VeroMagenta bottom layer in a tensile test with strain ranging from 0 to 0.5. Besides the change in colors, stretching the sensing belt also affects the measured overall intensity. Due to changes in

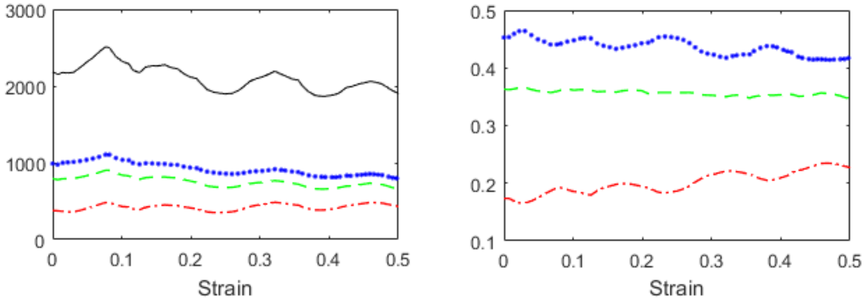

Figure 3.7: (Left) The raw data of red (dash-dot), green (dashed), blue (dotted) and light-intensity (full line) obtained from a color-based sensing setup as shown in Fig.3.6. (Right) Normalized RGB by dividing by the measured light-intensity.

reflectivity, shadows, distance-to-sensor and the underlaying materials, the intensities of the R-, G- and B-components go up or down simultaneously, which thereby distorts the signal. The same phenomenon is also observed for the integrated design. Normalizing the RGB-data by the intensity does not give a monotonic signal either. A more sophisticated method is presented in Section 3.3.2.

3.3.2 Signal processing

As can be found in Fig. 3.7, the RGB raw data shows a trend of increase in red and decrease in both blue and green. According to the RGB values of VeroMagenta (VM) and VeroCyan (VC) materials $RGB_{\mathrm{VM}} = (166, 33, 98)$ and $RGB_{\mathrm{VC}} = (0, 93, 127)$, it can be found that the change of colors in three components is indicating the increase of VeroMagenta and the decrease of VeroCyan. A naive processing of the RGB signals would therefore be

$$f = -I_{\mathrm{R}} + I_{\mathrm{G}} + I_{\mathrm{B}}, \tag{3.4}$$

which accumulates the trend of three components, I_{R}, I_{G} and I_{B}, into a single signal. Note that, if a positive weight is placed in front of I_{R}, the increasing of red will somewhat cancel out the decrease of I_{G} and I_{B} which leads to a less significant signal. A problem of processing by Eq.(3.4) is that it does not result in a monotonic function – i.e., fluctuations still exist (see the left of Fig. 3.8). We can eliminate the intensity peaks where R, G and B components move up in intensity with an equal amount (as shown on the left of Fig. 3.7), by adding weights to the intensities that sum up to zero. Our experimental tests show

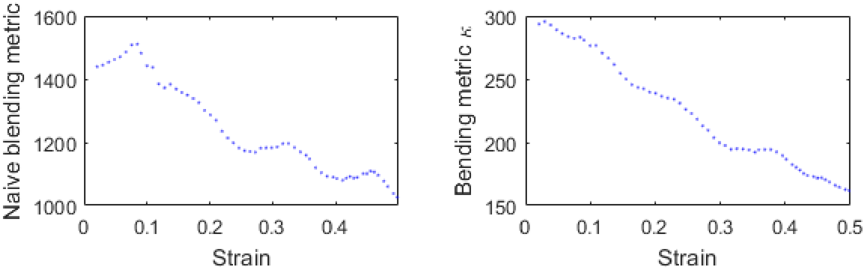

Figure 3.8: Processing color signals into a metric of deformation – (left) by a naive blending scheme (as Eq.(3.4)) and (right) by a weighted blending scheme (as Eq.(3.5)).

that using the normalized difference between VeroCyan and VeroMagenta as weights can generate a monotonic function $\kappa(\cdot)$. The weighted integration of $I_{\rm R}$, $I_{\rm G}$ and $I_{\rm B}$ can be defined as

$$\kappa = (\hat{R}_{\rm C} - \hat{R}_{\rm M})I_{\rm R} + (\hat{G}_{\rm C} - \hat{G}_{\rm M})I_{\rm G} + (\hat{B}_{\rm C} - \hat{B}_{\rm M})I_{\rm B}, \tag{3.5}$$

where the normalized RGB components of VeroCyan and VeroMagenta are $(\hat{R}_{\rm C}, \hat{G}_{\rm C}, \hat{B}_{\rm C}) = (0, 0.4227, 0.5773)$ and $(\hat{R}_{\rm M}, \hat{G}_{\rm M}, \hat{B}_{\rm M}) = (0.5589, 0.1111, 0.3300)$.

For the internal signal generator, this results in a very sensitive monotonic signal as demonstrated in Section 3.4 and the supplementary video. For the external generator, the signal is also monotonic, with some small fluctuations occurring at higher strains (see the right of Fig. 3.8). These fluctuations are an artifact of the sensing window, as will be discussed in Section 3.3.3.

3.3.3 Simulation

From the normalized signal of colors shown on the right of Fig. 3.7, we can observe fluctuations where the intensities of red and blue move in opposite directions. These fluctuations occur whenever a non-integer amount of periods is visible within the sensing window. The color of the material moving in and out of the sensing window causes the variations of ratios r_A and r_B going up or down. About the influence of the sensing window on the fluctuations of color signals, the following observations are found:

- **Size of sensing window** – The fluctuations diminish with an increase of window size. Similarly, the same phenomenon can be found when de-

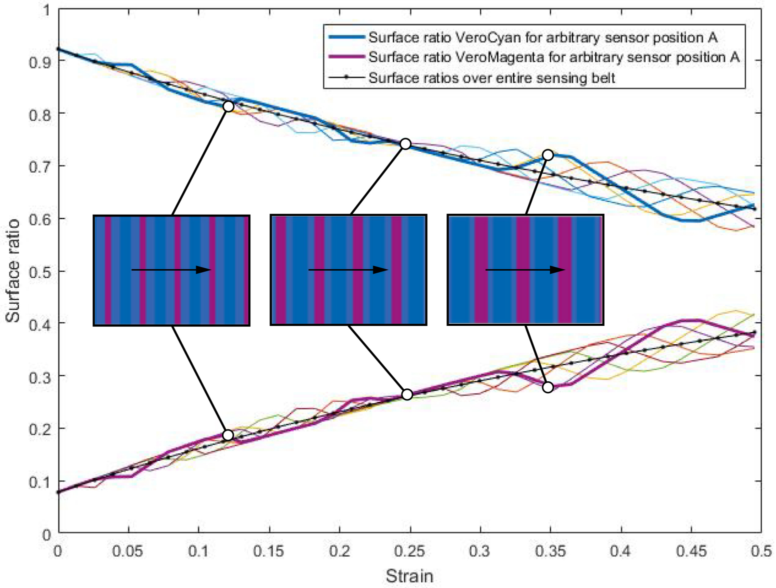

Figure 3.9: Simulation of stretching tests – the signals are obtained by placing the sensing window at six different positions. The color patterns that can be observed through a sensor window are also displayed for a few different strains.

creasing the length of the T-components – this is equivalent to enlarging the relative size of a sensing window.

- **Position of sensing window** – The fluctuations appear at different regions of strains when we place the sensing window at different places. However, the appearance of fluctuations cannot be avoided at any place.

A simulation was conducted to study these influences as shown in Fig.3.9, where the sensing window is placed at the boundary of the second period of the sensing belt and shifted over the length of a period of the structure in six steps. At each place, our simulator generates a curve indicating the ratio of the cyan region's area over the window's area (the top curve) and a curve according to the ratio of the magenta region's area (the bottom curve). Moreover, we also generate two curves by (1) using the total area of all cyan regions over the area of the entire sensing belt and (2) using the total area of all magenta regions over the entire structured strip, which are displayed in black with dots. These two curves serve as ideal signals as they are not influenced by the above two factors – i.e., size and position of sensing window.

The simulation results shown are consistent with the results presented on the right of Fig.3.7 and Fig.3.8. When having a large deformation, the relative size of the sensing window as compared to the dimensions of the periods becomes small. As a result, larger fluctuations appear on the signals.

3.3.4 Calibration

With the help of the processed signals as shown in the right of Fig.3.8(b), we are able to determine an algebraic function $\epsilon(\kappa)$ indicating relationship between color-signal and the level of deformation by a calibration process. Specifically, the parameters of the following function are determined by a least-square fitting,

$$\epsilon(\kappa) = a + b\kappa + c \log(\kappa). \tag{3.6}$$

For the sensing belt data shown in the right of Fig.3.8, we obtain $a = 4.845$, $b = -0.0005137$ and $c = -0.8711$ with R-square being 0.9899.

Similar to stretching tests, bending tests are conducted on the integrated design. We calibrate a function $\alpha(\cdot)$ in terms of bending 'angle'. That is

$$\alpha(\kappa) = \tilde{a} + \tilde{b}(\kappa + \tilde{d}) + \tilde{c} \log(\kappa + \tilde{d}), \tag{3.7}$$

with α indicating the level of deformation (e.g., bending angle of the bellow that is captured by the sensor, as shown in Fig.3.12 C). As negative values are allowed for the bending metric κ, a coefficient $\tilde{d}$ is added to ensure the validity of a $\log(\cdot)$ function. The calibrated coefficients for the bellow shown in Fig.3.12 are $(\tilde{a}, \tilde{b}, \tilde{c}, \tilde{d}) = (2038, 0.1133, -303.3, 1301)$ with R-square being 0.9968. Each newly printed strip or bellow needs to be calibrated, as the performance is also dependent on the fabrication process.

3.4 Experimental Results

This section discusses the experimental results of our sensing approach. Both actuator embodiments and the separate sensing belts have been tested under extreme lighting conditions, ranging from near darkness to illumination by two Menik LS-1200 LED panels (with $7380\,\mathrm{Lumen}$) placed at a distance of $20\,\mathrm{cm}$ on both sides of the actuators. The differences in bending metric caused by lighting variation were marginal, as is also demonstrated in the supplementary video material by turning off the LED panels during measurement.

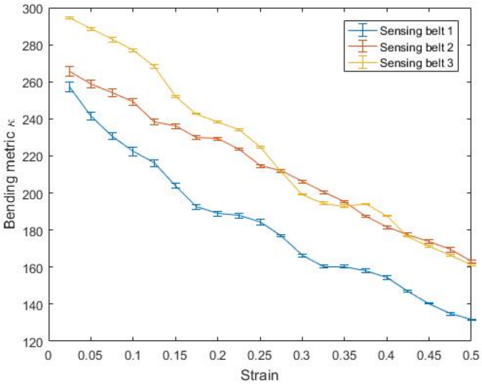

Figure 3.10: Average result of the bending metric κ over five measurements for three different sensing belts. The standard deviations are indicated along with the curves.

3.4.1 Results by external signal generator

Three identical sensing belts have been 3D-printed and tested using the setup described in Section 3.3. Each sample was tested five times using the same clamping. The raw data points were re-sampled at every step of 0.025 in the strain. An average was calculated for the five tests, and the standard deviations are shown as well in Fig.3.10. Although a separate calibration is needed for each sensing belt, different measurements of the same belt are very consistent. Integration of the sensing belt on a bending actuator to control the position and detect obstacles is demonstrated in Fig.3.11. Upon touching an object, the bending metric κ starts to deviate from the curve corresponding to collision-free motion.

3.4.2 Results by internal signal generator

A single miniaturized color sensor was used and placed at the first bellow of the integrated design (as indicated in Fig.3.1). The progressive results of the integrated sensing approach are shown in Fig.3.12. Here, the bending metric is plotted with reference to the pressure during unobstructed bending. Note that the signal generator is still sensitive at full actuation, and thus covers the whole range of actuation. Figure 3.1 has already demonstrated how the deformation of a bellow can be controlled through the bending metric κ.

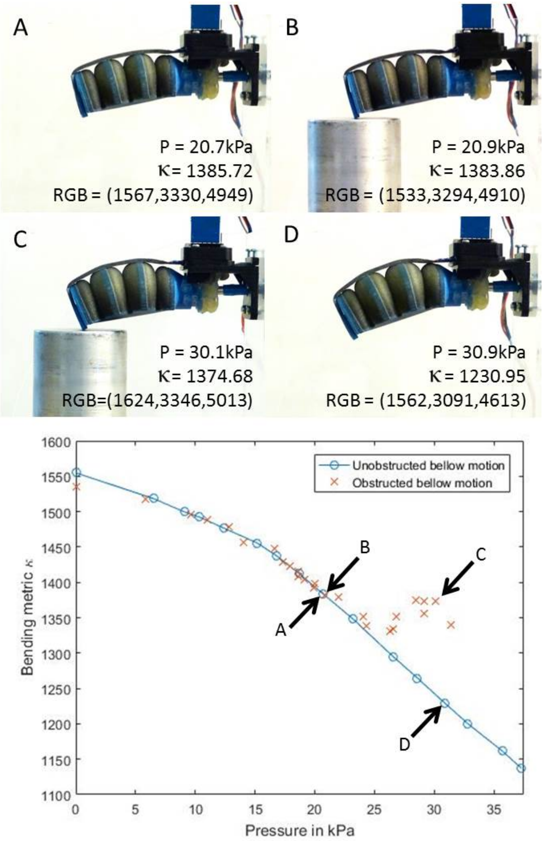

Figure 3.11: Before and until the moment of touching, the measured bending metric κ of the bellow's motion follows that of the collision-free motion (A & B). Upon touching, the bending metric of an obstructed bellow (C) deviates from the unobstructed bellow (D) when the same pressure is applied.

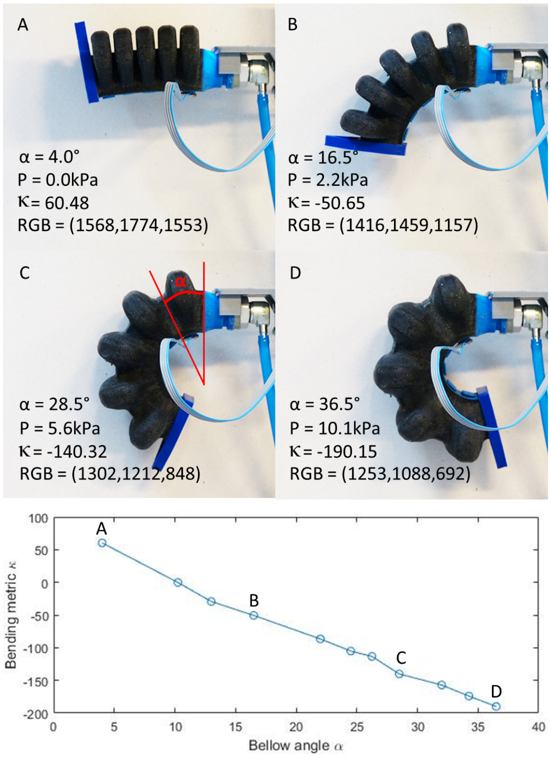

Figure 3.12: The bending metric κ plotted w.r.t. the bellow angle α. The angles have been measured over the deformed bellow as indicated at bellow C. The signal is monotonic and sensitive to small changes.

3.5 Conclusion and Discussion

We present a method to provide feedback for the deformation control of soft robotic actuators using 3D printed color-patterns. Two designs are presented: 1) an external signal generator that translates a change in strain to a change in color ratio, and 2) an internal signal generator that generates a change in color ratio upon a change in bellow shape. Along with the novel structural design, we have investigated methods for converting the color signals into a monotonic metric that can be used as an indicator for the flexure in bending deformation. The effectiveness of the color-based sensing approach has been verified in experimental tests.

In our current practice (e.g., Fig. 3.1), the placement of a sensor is determined by trial-and-error to obtain the most sensitive signal. When moving the sensor to the middle of the actuator, the value of κ is less sensitive to the global shape of the actuator. This is because this color-based sensing method only provides information about a local shape deformation. To obtain a precise shape estimation, the data from multiple sensors needs to be fused, which we plan to investigate in the near future. Moreover, different types of deformations, rather than bending, such as twisting and elongation, also will be considered in our future research.

4

Calibrating Sensors for Soft Robot Proprioception

In the second research cycle, the signals from the sensors were first merged to a single bending metric and then calibrated to the angle of a single bellow on the actuator. This is an overly simplified way of representing the shape of soft actuators that have many more degrees of freedom. Moreover, the calibration was performed during unobstructed bending and would therefore not yield reliable results if the actuator were interacting with objects. The aim of the third research cycle was to address the problem of calibration. As the relationship between the shape of the actuator and the sensor signals cannot be easily modeled analytically, a machine learning-based approach was adopted to calibrate the sensors. First, a vision-based system was used to capture the position of a number of markers on the soft actuator while it was interacting with objects. Next, a machine learning model was trained using the raw sensor data as inputs, and the marker coordinates as outputs. Through this approach, a set of points on the robot can be accurately predicted from the sensor data, even when the soft actuator is interacting with objects. This calibration provided the basis for the reconstruction method (RQ3) discussed in research cycle four.[1]

---

[1] This chapter is published as: **R. B. N. Scharff**, R. M. Doornbusch, E. L. Doubrovski, J. Wu, J. M. P. Geraedts, and C. C. L. Wang, "Color-based proprioception of soft actuators interacting with objects", *IEEE/ASME Transactions on Mechatronics*, vol. 24, no. 5, pp. 1964–1973, 2019. Note: a few small corrections and/or clarifications have been made to the original published text.

4.1 Introduction

Due to their intrinsic compliance, actuators made from soft materials have shown great potential in many tasks such as grasping. The flexibility of soft materials allows the actuator to passively adapt its shape in response to physical contacts with objects. The control of soft robot actuators is typically performed in an open loop. For grasping objects with known geometry, the curvature of a pneumatic actuator can be controlled through applied pressure and mechanical programming (e.g., [14], [28]). However, for precise operations in unstructured environments and dexterous manipulation [46], mechanical programming becomes ineffective and closed-loop control is needed. A fundamental step towards feedback control of soft actuators is the development of proper proprioception methods [42], [47].

Our work focuses on soft pneumatic actuators. This type of actuator is commonly used in soft robotics. It uses pressurized air to inflate chambers. The asymmetry in the geometry of internal chambers or physical properties of constituent materials drives the shape to the intended deformation [12]. Specifically, downward bending can be realized through pressurization of an air chamber with an extensible top layer and an inextensible bottom layer [17]. In this chapter, we present a novel method to accurately sense and reconstruct the bended shape of soft pneumatic actuators during real-time interaction with objects.

4.1.1 Related Work

Sensing in soft actuators

The use of exteroceptive sensing devices such as visual tracking systems has been reported in soft robotics (e.g., [18], [29], [30]). However, proprioceptive sensing approaches have the potential to create more compact sensing systems and further improve the autonomy of soft robots. This requires sensors that can be embedded in soft actuators. Ideally such sensors shall be bendable and/or stretchable, and thus do not prevent the deformation of soft actuators. An overview of sensing principles for soft actuators can be found in [13], [37], [48].

A commonly used approach to realize position sensing in soft robots is through embedded channels filled with conductive inks [32], [36] or liquid metals [33], [41] that change electrical resistance upon deformation. Other resistive sensors make use of conductive polymers that can be directly 3D-

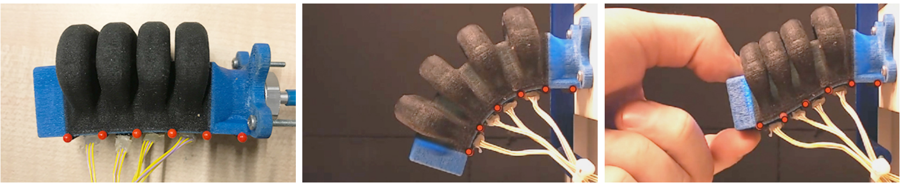

Figure 4.1: A soft pneumatic actuator with red glass-headed pins inserted in the inextensible layer, serving as makers for the training of the neural network (left). The deformed shape is represented by the red dots, the locations of which are predicted from four color sensors embedded in the actuator (middle and right). Note that the predicted locations of the red dots accurately match the red pins, in the absence of object interaction (middle) and during interaction with objects (right).

printed [49], [50], or off-the-shelf flex sensors [51]. An overview of resistive flex sensors is given by Saggio et al. [52]. An alternative use of electrical properties includes highly flexible capacitive sensors built from conductive fabrics and silicone [34] or aluminum and silver layers on an elastomer surface [35].

Some contactless sensors have also been developed, using optics [53] or magnetics [38]. For instance, Zhao et al. developed stretchable optical waveguides in soft prosthetic hands to feel the shape and softness of objects [39], [40].

Many of existing sensors suffer from elastic hysteresis, fabrication complexity and compromise in compliance, or can hardly be extended for the integration of multiple sensors throughout the actuator, which is necessary for reconstructing complex global deformation. Our color-based sensing approach overcomes all these difficulties.

Actuator model

Besides the development of accurate sensors, the actuator model which describes the global deformation and to which the sensing is calibrated is important for feedback control. Existing algorithms for shape reconstruction of soft robots are oversimplified, and do not address complex / local deformations [48]. The global deformation of soft actuators is typically described by using a simple descriptor such as average curvature [38], [39], [41], [54] or bending angle [49]–[51]. These univariate models are representative for bending in the absence of object contacts. However, the soft actuator continuously adapts its shape during interaction with objects. A single parameter thus becomes ineffective to accurately describe the global deformation (e.g., the sigmoid curve in Fig. 4.1). Other soft robot sensing methods [40], [55] focus on object detection rather than shape sensing, bypassing the need for a continuous actuator model.

While the kinematics can be analytically derived for robots composed of rigid links, the deformation and motion for soft robots involves a lot more degrees of freedom (DoFs). A promising direction for soft robots is the use of learning algorithms to directly predict the deformed shape of the actuator based on sensor values. Giorelli et al. [56], [57] used a *Feed-forward Neural Network* (FNN) to learn the tip position of a cable-driven soft tentacle based on the cable forces. Runge et al. [58] suggested *Finite Element Analysis* (FEA) based training to learn a kinematic model of a soft pneumatic actuator through a neural network. Neural networks have also been applied to calibrate soft sensors to estimate the magnitude and the location of a contact pressure [59]. Wall et al. [42] used polynomial regression learning methods to find the most effective layout of sensors from a redundant layout of sensors on a soft pneumatic actuator. In parallel with our work, Van Meerbeek et al. [60] predict the bending and twisting of a soft foam with embedded optical fibers, comparing several learning techniques. Thuruthel et al. [61] show that temporal relations in the sensor data can be used to predict the fingertip position of a soft actuator using a recurrent neural network known as *Long Short-Term Memory* (LSTM). However, neither of them has demonstrated the capability of predicting the deformation generated by unknown interactions as shown in our work. An FNN is used in this chapter to reconstruct the global deformation. It demonstrates that learning algorithms can be used to fuse information of multiple sensors that overlap with each other. Benefited from our novel color-based sensing approach, this is the the first approach that can accurately predict the global shape of an actuator interacting with objects.

4.1.2 Overview and Organization of the Work

The basic idea of our shape sensing approach is to translate the bending that occurs in the extensible parts of soft actuators into a measurable change in colors. The color signals are captured by a miniaturized color sensor that is embedded in the inextensible layer of the soft actuator. To translate structural deformation into changes in color, we developed a multi-color structure that can be fabricated by 3D printing. With the local deformations of the actuator detected by a set of embedded color sensors, we make use of an FNN to reconstruct the global deformation. As shown in Fig. 4.1, the deformed shape of a pneumatic actuator can be accurately reconstructed by the proposed method,

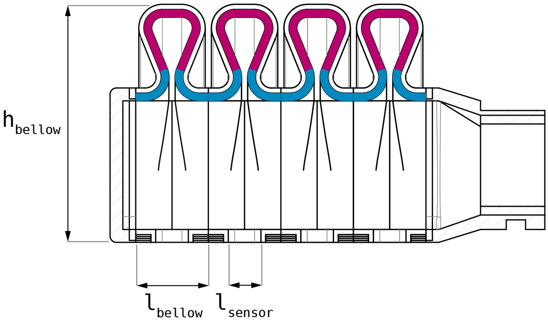

Figure 4.2: Illustration of multi-color bellows inside a soft pneumatic actuator for translating deformation into changes in color. The dimensions of the bellow used in our experiments are $l_{\mathrm{sensor}} = 5.1\,\mathrm{mm}$, $l_{\mathrm{bellow}} = 11.3\,\mathrm{mm}$ and $h_{\mathrm{bellow}} = 37.0\,\mathrm{mm}$.

even after the inextensible bottom layer is largely distorted into a sigmoid-like curve. The reconstructed global deformation can provide much more information than (averaged) curvature or bending angle as used in many existing approaches (e.g., the 3D printed soft hand in [14]) to the control system of soft actuators.

Note that, this chapter is an extension of the previous chapter [27], which proved the principle of color-based curvature sensing. Here, we extend it to reconstruct the multivariate shape deformation by integrating multiple color sensors. To this end, machine learning is employed for deformation reconstruction.

The rest of this chapter is organized into five sections. Section 4.2 presents the developed color-sensing method and discusses the design and fabrication of the actuator with integrated signal generators. In order to generate training data set for accurately estimating a deformed shape, the method for data acquisition is introduced in Section 4.3. Both the hardware setup and the steps of sampling will be discussed. After that, an FNN-based method is employed in Section 4.4 to fuse the color signals captured by multiple sensors to reconstruct the deformed shape of an actuator. The experimental results will be presented in Section 2.5 and the chapter ends with conclusion in Section 4.6.

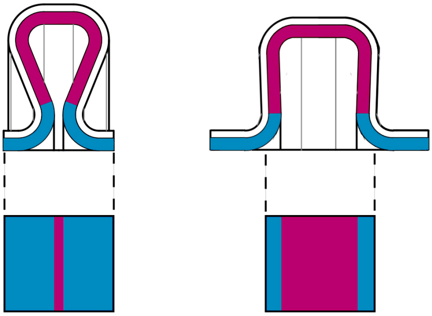

Figure 4.3: Illustration of a bellow before and after being pressurized. The pattern of colors that can be captured through the sensing window is shown at the bottom.

4.2 Color-based Sensing

4.2.1 Sensing Principle

The sensing principle is based on multi-color structures, the color and intensity of which gradually change upon deformation. The changes can be observed by cost-effective color sensors. To substantiate this principle, as illustrated in Fig. 4.2, inside a soft pneumatic actuator Ω-shaped bellows are colored by two distinct colors, distinguishing different parts of a bellow. Beneath each bellow a color sensor, embedded in a plug, is plugged into the inextensible layer of the bending actuator. Upon pressurization of the air chamber, the bellows inflate, exposing a large area of the initially occluded color (i.e., magenta) to the window of the color sensor (see Fig. 4.3). Consequently, the measurement of the sensor changes accordingly. This sensing principle can be applied to bellow-based pneumatic actuators of different shapes and dimensions. The length of the inflatable part in our design is $45.2\,\mathrm{mm}$. The main dimensions of the actuator are indicated in Fig. 4.2. Although the measurements depend on the particular actuator design, a general learning procedure, which will be presented in Section 4.4, can be conducted to map the measurements of the color sensors to the deformed shapes of an actuator.

4.2.2 Sensor Crosstalk

Although each color sensor is influenced most by the signal generated by the bellow directly above it, it is also influenced by adjacent bellows, as illustrated in Fig 4.4. The degree of influence is not constant but depends on the defor-

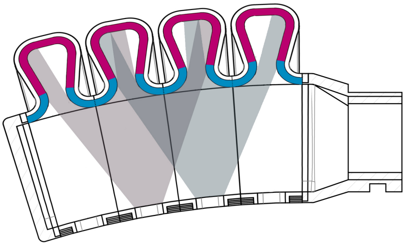

Figure 4.4: Illustration of sensor crosstalk – each sensor captures signals generated by the bellow directly above it and the neighboring bellows.

mation of the actuator.

This ‘crosstalk’ between sensors would normally be undesirable, as it complicates signal processing. We propose the use of neural network based method for fusion, which does not suffer from this undesirable effect as it can learn the deformed shape of an actuator at a global level. In fact, as will be demonstrated in Section 2.5 this crosstalk situation can actually be used to reduce the number of sensors. This would not be possible when using a separate sensor calibration for each bellow segment.

4.2.3 Color Sensors

A color sensor is plugged into the inextensible layer of the actuator at each bellow segment. To reduce the size of color sensors, we customized the color sensor with a design of two-layer PCBs, mounted on a 3D-printed plug (see Fig. 4.5). The shape of the plug creates an airtight seal. The detailed design of the sensor can be found in Appendix 8.2.3. The color sensor has a built-in LED that emits light to the multi-color structures above it. Similar to the sensor crosstalk, the light is also shed on the neighboring bellow segments.

For color sensing, the *TCS34725 light-to-digital converter* is used. The sensor returns four values, namely *Red, Green, Blue and Clear* (RGBC), for each exposure. The clear value is IR filtered light, which gives an indication of overall light intensity. The sensor integration time is set to $50\ \mathrm{ms}$ and the gain to $60X$. An *Adafruit Feather HUZZAH with ESP8266* reads the sensor-data of the four sensors with a negligible delay between each sensor by using a *TCA9548A* I2C Multiplexer. The Feather HUZZAH runs code using Adafruit’s TCS34725 library. A command to collect a data sample is sent from the main Matlab script through serial communication. The collected data is then sent

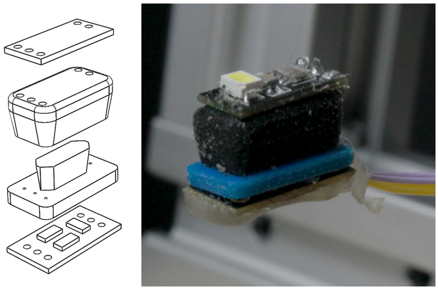

Figure 4.5: Both an exploded view of the sensor plug design (left) and the assembled sensor plug (right) are shown. In the exploded view (left), from the bottom up – the lower PCB, rigid bottom, flexible plug and upper PCB. Note that the rigid bottom and flexible plug are printed as one piece.

back to Matlab.

4.2.4 Materials & Fabrication

The embodiment of our design is fabricated on a *Stratasys Objet 350 Connex3* multi-material 3D printer, which uses Material Jetting technology and can print combinations of up to three different building materials in addition to a water soluble support material. The overall structure of the actuator is printed with the flexible Agilus 30 Black, while the multicolored bellows are printed with the rigid VeroCyan and the rigid VeroMagenta. Note that pure blue or red colors are not available for this 3D printing system. As the colored materials are rigid, we want to apply a layer as thin as possible. VeroMagenta and VeroCyan but not VeroYellow materials are chosen as VeroYellow has a higher translucency.

The Agilus 30 Black has an elongation of $220 \sim 270\%$ at break and a tensile strength of $2.4 \sim 3.1\mathrm{MPa}$ – as documented by Stratasys. The RGB values of the VeroMagenta (VM) and VeroCyan (VC) materials are $RGB_{\mathrm{VM}} = (166, 33, 98)$ and $RGB_{\mathrm{VC}} = (0, 93, 127)$ respectively.

4.2.5 Color Signal

Figure 4.6(a) shows the raw data that was obtained by reading out the RGBC-data of a color sensor during unobstructed progressive bending. A clear decrease in overall intensity can be observed. This is due to the increased measurement distance towards the hidden (magenta) elements that appear upon

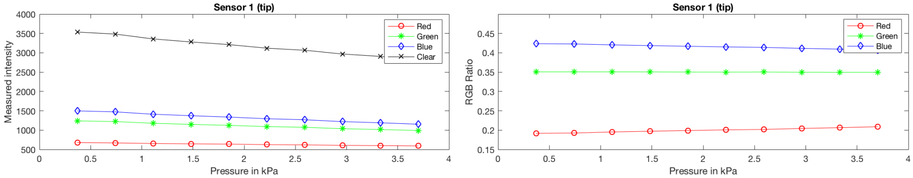

(a) Raw RGBC data

(b) RGB normalized by the Clear value

Figure 4.6: (a) Raw RGBC data of a color sensor measured at pressure intervals during unobstructed bending. Besides a clear decrease in intensity due to an increased measuring distance, a change in color can be observed as well. (b) RGB normalized by the Clear value. The ratio of red gradually increases from 0.1918 to 0.2088, while the blue ratio decreases from 0.4235 to 0.4071.

bending, as well as the decrease in overlap of the light of the LEDs upon bending (similar to the crosstalk in the sensors explained in subsection 4.2.2). Besides the change in intensity, a color change can be observed as well. As shown in Fig. 4.6(b) the raw RGB values are normalized by dividing the raw RGB values by the Clear value. The normalized RGB color codes show a clear increase in red and a clear decrease in blue, confirming the appearance of a larger magenta area. Similar observations can be made from sensors embedded in other slots, as can been seen in Fig. 4.7. We do not observe a clear trend in the green ratio upon bending. This can probably be attributed to the fact that the VeroCyan material contains less green than real cyan while the VeroMagenta contains more green than real magenta, and the AgilusBlack also contains some green.

4.3 Data Acquisition

This section focuses on describing how the data, used in the learning for reconstruction procedure, was acquired. We built a setup that randomly changes the actuation pressure and the position of an obstacle. It then captures an image of the deformed actuator and collects the measurements of the color sensors. Two readings are made during one loop – due to hysteresis the actuator will slowly deform after reaching a certain pressure. Both readings are collected into the set of training samples. This allows for generating more samples in a shorter timespan. The sample data collection process is automatic. The main loop, running in Matlab, looks as follows:

1. Set random obstacle angle;

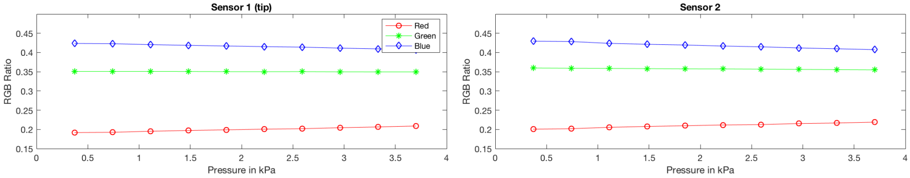

(a) RGB ratio at the first measurement: [0.1918, 0.3508, 0.4235]. RGB ratio at the last measurement: [0.2088, 0.3496, 0.4071]

(b) RGB ratio at the first measurement: [0.2006, 0.3597, 0.4295]. RGB ratio at the last measurement: [0.2188, 0.3548, 0.4074]

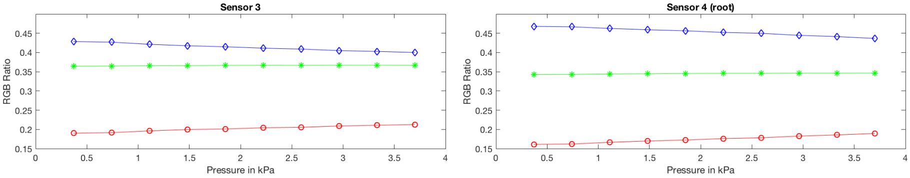

(c) RGB ratio at the first measurement: [0.1902, 0.3646, 0.4286]. RGB ratio at the last measurement: [0.2129, 0, 3666, 0.4001]

(d) RGB ratio at the first measurement: [0.1612, 0.3428, 0.4679]. RGB ratio at the last measurement: [0.1894, 0.3466, 0.4367]

Figure 4.7: RGB values of the four sensors plugged underneath the four bellows. The RGB ratio data is obtained by dividing the raw RGB values by the Clear value. For each sensor there is a clear increase in red and decrease in blue.

2. Set random actuation pressure;
3. Take first picture;
4. Read out data of the color sensors;
5. Wait for 2 seconds;
6. Take second picture;
7. Read out data of the color sensors;
8. Set pressure back to zero;
9. Set obstacle back to default position.

Our data acquisition setup is illustrated in Fig. 4.8. Its main components are discussed in the following.

We took samples from 500 random pressure/obstacle-configurations for the training. Two samples were taken for each configuration, so a total of 1000 data samples were collected. The total data collection procedure took less than 5 hours.

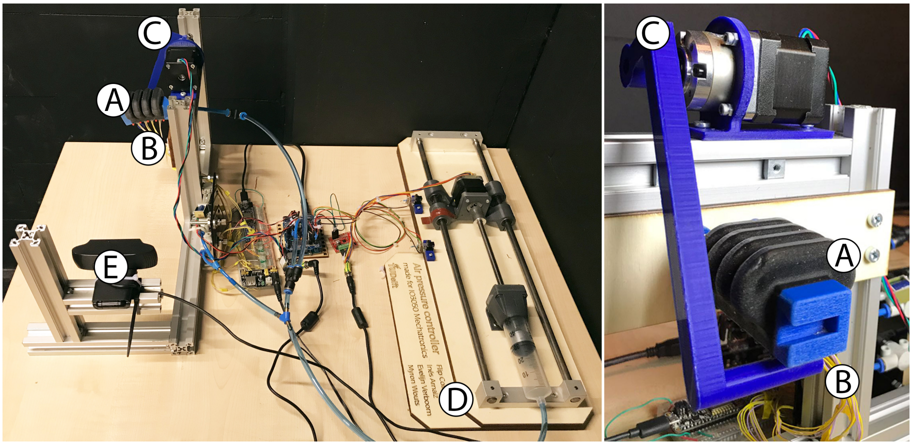

Figure 4.8: The data acquisition setup: (A) the soft pneumatic actuator, (B) the four color sensors, (C) the variable obstacle, (D) the pressure regulator and (E) the camera.

4.3.1 Shape of Actuator

We used the soft actuator design as discussed in Section 4.2. Our actuator has four bellows. Red glass-headed pins are inserted into designated pin holders in the inextensible layer, serving as markers (see Fig. 4.1). An additional marker is placed on the origin of the actuator. The positions of the origin marker and the first marker are fixed (see Fig.4.9), and the distance between the markers is known. These markers are used to determine the orientation of the actuator and to convert from pixel positions to metric positions in the unit of mm. As a result, the shape of an actuator can be obtained by processing the images captured by camera.

4.3.2 Variable Obstacle

An obstacle is attached through a 3D-printed arm linked to to a stepper motor (see Fig.4.8(C)), and thus its location can be varied by the stepper. To (roughly) align the trajectories of the obstacle and the actuator and thus create valid obstructing, the arm has a length of $140\,\mathrm{mm}$ and its axis is located $100\,\mathrm{mm}$ above the inextensible layer of the actuator. At the start of one loop, the obstacle angle is randomly chosen between 15 and 32 degrees. We have a resolution of 65 uniform steps within this range. We use an *Arduino Uno* and *Pololu DRV8825* stepper driver to control the stepper (see Fig.4.8(C)). The random obstacle position is controlled the main Matlab program through

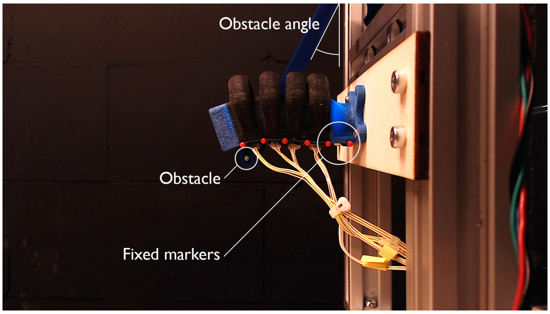

Figure 4.9: An example sample of the raw camera data when the actuator interacts with an obstacle. Six red markers are used to describe the actuator's shape. The two most right markers at the root of actuator are fixed.

serial communication.

4.3.3 Pressure Regulator

The actuator requires low pressures to generate relatively large changes in actuator deformation. For the data acquisition, we need to generate stable actuator deformations with a high resolution within the actuator's actuation range of 0 to $5\,\mathrm{kPa}$. This is realized by a syringe based pressure regulator. Specifically, a stepper motor moves the plunger of a syringe to add air to, or subtract air from, the actuator (see the illustration in Fig.4.8(D)). The pressure inside the actuator is measured using an *NXP MP3V5050GC6U* pressure sensor with a range of $0 - 50\,\mathrm{kPa}$. A desired pressure can then be achieved by a PID-controller using Arduino.

4.3.4 Camera

We use a *Logitech C922 Pro Stream Webcam* to capture the positions of markers. The camera is placed at a distance of $250\,\mathrm{mm}$ to the actuator markers. We capture images with a resolution of $1920 \times 1080\mathrm{p}$. The camera settings are set manually and are kept constant over all captured images. A sample of the raw image captured by camera is shown in Fig. 4.9.

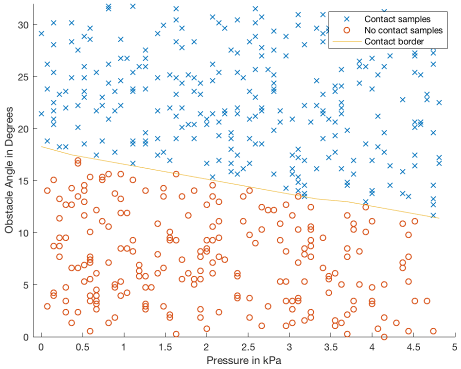

Figure 4.10: Samples that were collected during a pilot acquisition and training, where the samples indicated by a cross are interacting with the obstacle. Although the training performed quite well on the test-data and we can well predict the unobstructed bending, the learned shape predictor had inferior results when confronted with other types of obstacles not presented in the training set.

4.3.5 Sampling Strategy

During a pilot acquisition, the pressure was varied between 0 and $5\,\mathrm{kPa}$ and the obstacle angle between 0 and 32 degrees, as shown in Fig. 4.10. However, our experiments suggest that a relatively high amount of constrained configurations in the training data can improve the training results. Therefore, we increased the minimum value of the obstacle angle to 14.5 degrees. The results of the final sampling are shown in Fig. 4.11. Note that the maximum pressure was also reduced to increase the life-span of the actuator.

4.4 Deformation Reconstruction

The global deformation of an actuator can be represented by the coordinates of the six markers in the inextensible layer. This section discusses the reconstruction of the deformation from the sensor data. We use a Feed-forward Neural Network to train the global actuator shape based on the sensor data. To train the network, we use the RGBC-data of the sensors as inputs and the coordinates of six markers as outputs. The RGBC-data of the four sensors can be directly fed into the FNN. Some processing is needed for the marker coordinates as the set of training data.

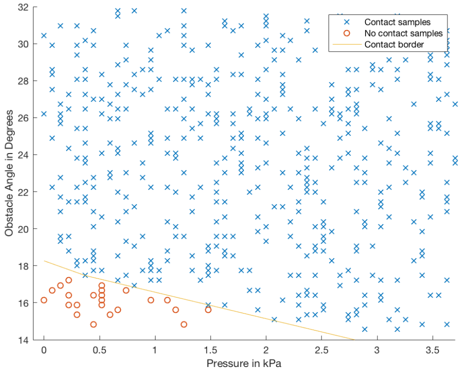

Figure 4.11: The final sampling strategy that was applied to collect the training data. After introducing more contacted samples into the training set, the predictor can reconstruct very accurate shape of an obstructed actuator. the predictor gives a better reconstruction of obstructed actuator shapes, while maintaining its accuracy on unobstructed actuator shapes.

First, we undistort the captured images using the parameters obtained from a multi-plane camera calibration. Our calibration has a Mean Pixel Error of 0.44. Using the fixed distance of $11.4\ \mathrm{mm}$ between the first two markers on the right, we make a conversion from pixel-scale to millimeter-scale at the rate of $6.8875 : 1$. This means the mean error of the calibration is $0.064\ \mathrm{mm}$. We remove the red cables shown on the right of Fig. 4.9, by simply cropping out the right of the picture to a resolution of $1300 \times 1080\mathrm{p}$. After cropping, we use Matlab's *Computer Vision System Toolbox* functions to extract the x- and y-coordinates of the six red markers in millimeter. The positions of the markers are ordered by solving a *Travelling salesman problem*. These values are used as outputs of the FNN.

A graphical representation of the FNN is shown in Fig. 4.12. The two-layer network has a hidden layer with ten neurons. The hidden layer uses a sigmoid transfer function and the output layer uses a linear transfer function. We have a total of 16 inputs (four sensors with four measurements) and 12 outputs (x- and y-coordinates of six markers).

Unless otherwise specified, we use a block division of our samples, where the first 70% of our samples are used for training, the next 15% as validation set and the remaining 15% as test set. We apply the Levenberg-Marquardt algorithm to train the network, and obtain a shape predictor with the raw data of the sensors as input.

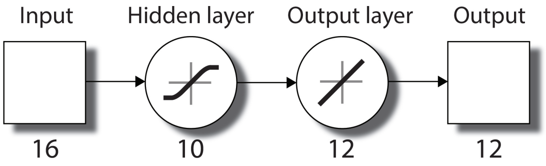

Figure 4.12: Graphical representation of the Neural Network configuration used in our training process and the shape predictor.

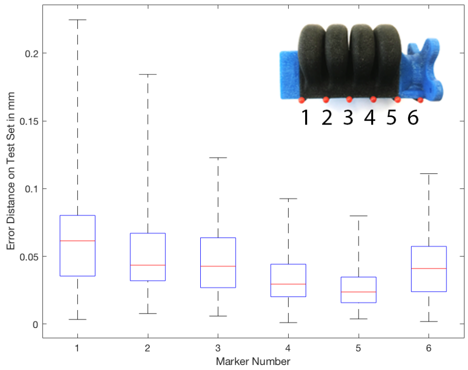

Figure 4.13: The error distance between the real and the predicted positions for each marker. The box plot shows the median, the 25th / 75th percentile, and the minimal / maximal bounds.

4.5 Results

4.5.1 Accuracy

The error distance between the real and the predicted marker positions is calculated for all marker positions of the samples in the test-set. The error distance is calculated as

$$\epsilon_i = \sqrt{(x_{\mathrm{R}_i} - x_{\mathrm{P}_i})^2 + (y_{\mathrm{R}_i} - y_{\mathrm{P}_i})^2}, \tag{4.1}$$

where subscripts R and P indicate the real and predicted coordinates respectively and i indicates the sample number. The results are given in Fig. 4.13. It shows that the median prediction error is lower than $0.1\,\mathrm{mm}$ for all marker coordinates. As would be expected, the largest error is observed on the marker at the tip of the actuator, and the error decreases when moving closer towards the root of the actuator. The error is smallest for the marker at location ‘5’.

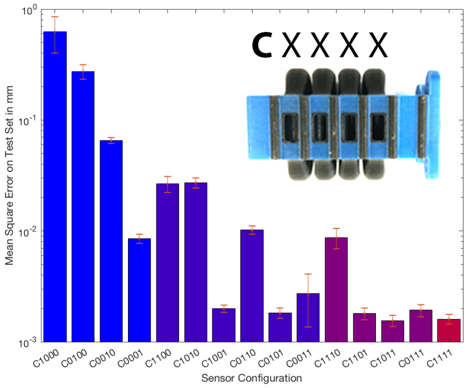

Figure 4.14: The mean MSE of the predicted outputs on the test-set for all 15 possible sensor configurations. Each configuration was trained 10 times. The standard deviation is indicated on the error chart.

To validate the advantage of using multiple sensors, we trained the FNN for all possible sensor quantities and sensor configurations. In Fig. 4.14, the mean *Mean-Squared Error* (MSE) of each configuration is plotted in a bar graph. We trained each configuration 10 times in these experiments.

The results show that the sensor at the root of the actuator (i.e., the configuration '*C0001*') individually provides the most complete information (with the mean MSE: 8.542×10^{-3}mm). As an individual sensor, configuration '*C0010*' (with the mean MSE: 6.551×10^{-2}mm) provides better information than the configuration where the sensor is placed at the second bellow from the tip (i.e., '*C0100*' with the mean MSE of 2.749×10^{-1}mm). However in a two sensor configuration, a combination of the second and the fourth sensors from the tip is the best (i.e., '*C0101*' with the mean MSE: 1.818×10^{-3}mm)) as the second sensor contains information that the root sensor is missing. The results show that two well-placed sensors can already achieve very accurate results and only small improvements are realized by adding more. This demonstrates that each sensor indeed captures information from neighboring bellow segments as well. Note that we train the predictor for the separate sensors by selecting the sensor outputs of the sensor of interest from the same data acquisition, in which the LEDs of all sensor plugs are on.

Our training based predictor also performs well on objects different from the trained obstacles. This is demonstrated in Fig. 4.15, where we test the sensing method on other objects.

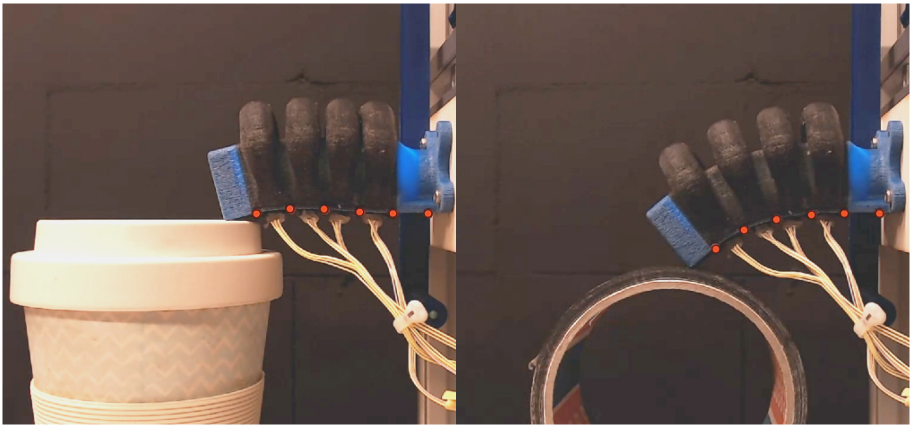

Figure 4.15: While projecting the predicted positions of markers onto the camera images, it can find that our method also gives very accurate prediction in scenarios that are different from the training set. Some have complicated curvatures – e.g., the 'S'-shape shown in the left figure.

The position of the actuator can be predicted in real time. In the supplementary video (https://youtu.be/zgOexw8YLQc), the predicted coordinates are projected on top of the live camera images to demonstrate the accuracy of the method in various scenarios. Due to the simplicity of the FNN configuration, the capturing (50 ms for the integration time) and evaluation (0.232 ms) of a new set of inputs is very efficient. This makes our approach very suitable for real-time feedback control. The relative slow loop in the supplementary video is due to the visualization of the $1920 \times 1080p$ camera image.

4.5.2 Robustness

We tested the actuators under some extreme conditions to explore how it would perform on load cases that were not included in the training set. Although some accuracy is lost, the neural network is still able to predict most of the extreme load cases quite well. The right of Fig.4.1 shows the prediction on a sigmoid-curved actuator shape that is realized by bending and rotating the actuator's tip at the same time.

It should be noted that our light-based sensing method is almost not affected by external lighting conditions. This is due to the light absorbing black flexible air chamber and the bright LEDs placed in the sensor plugs. We demonstrate this in the supplementary video where the actuator is tested in dark and extremely bright conditions.

Another aspect of robustness, repeatability, has also been tested in our experiments. As demonstrated in the supplementary video, sensors can be pulled out and inserted back in while regaining nearly the same result.

4.5.3 Importance of Color Signal

The raw RGBC data in Fig. 4.6 showed that, due to intensity changes that occur upon bending, the Clear signal on itself was already a good indicator of the bending deformation, To test the performancewhen only using the Clear signal to predict an actuator's shape, we trained our network with the Clear signal of the sensors as inputs. The training was able to realize a mean MSE of $2.633 \times 10^{-3}\mathrm{mm}$ on the test set (over 10 trainings) as compared to a mean MSE of $1.602 \times 10^{-3}\mathrm{mm}$ when including the RGB data as addition. This proves that the changes in color upon bending are very necessary for improving the accuracy of shape prediction.

Whereas the mean MSE of the *'1001'* sensor configuration was very close to the *'1111'* configuration when using all RGBC-data as inputs ($1.994 \times 10^{-3}\mathrm{mm}$ and $1.602 \times 10^{-3}\mathrm{mm}$ respectively), the mean MSE increases more significantly when only the Clear value is used ($5.165 \times 10^{-3}\mathrm{mm}$ for configuration *'1001'*). This means that the color signals are very important to ensure the robustness of our sensing approach.

When an application can accept the aforementioned error of $2.633 \times 10^{-3}\mathrm{mm}$, fast and low-cost shape sensing can be achieved by embedding off-the-shelf photo-detectors such as LDRs, and LEDs into a soft pneumatic actuator fabricated in a single color. This is considered as a simplified version of our approach with reduced accuracy and robustness, which can be applied to more durable actuators fabricated by silicone casting.

4.5.4 Comparison to Multivariate Polynomial Regression

To demonstrate the effectiveness of a neural network, we compare the MSE of the training result to the MSE obtained when using Multivariate Polynomial Regression (MVPR). For both the MVPR and the FNN, we use the first 850 samples for training, and evaluate the accuracy of prediction (by MSE) on the remaining 150 samples. A multivariate linear regression (MVLR) results in a predictor with an MSE of 0.0377 mm, whereas a quadratic MVPR results in an

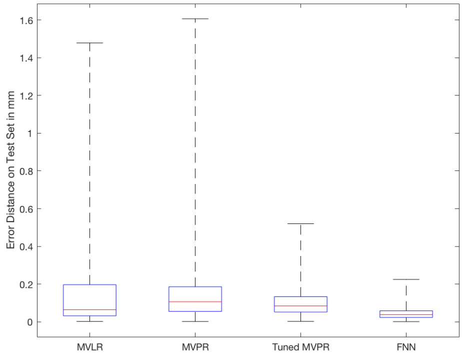

Figure 4.16: The distances between the real positions and the positions predicted by the multivariate linear regression (MVLR), the quadratic multivariate polynomial regression (MVPR), the tuned MVPR and the FNN. The predictions generated by the FNN have smaller errors.

MSE of $0.0788\,\mathrm{mm}$. Such errors are $23.5\times$ and $49.2\times$ that of the prediction by the FNN which has an MSE of $1.602 \times 10^{-3}\,\mathrm{mm}$. After manually tuning the polynomials of the MVPR by removing some of the quadratic terms, we were able to obtain a prediction with an MSE of $0.0079\,\mathrm{mm}$, which is still $4.9\times$ that of the corresponding MSE of the FNN. Moreover, the FNN-based predictor is robust and does not involve any manual tuning of parameters. Figure 4.16 shows the error distances over all markers by using the MVLR, the quadratic MVPR, the tuned MVPR and the FNN.

4.6 Conclusion

We have demonstrated a complete method to fabricate a soft pneumatic actuator with integrated color signal generators to realize accurate shape estimation in both obstructed and unobstructed situations. We have shown that our color-based sensing approach is robust and performs well on obstacles that were not included in the training data. This realization of accurate shape sensing is a significant step towards the application of soft robots in many dexterous tasks.

Our future work will focus on improving the performance on cases under specific loading conditions by collecting additional training data for these load-cases. Moreover, 3-dimensional load cases and data collection could be used to include the effects of twisting of the bellow upon contact. Optimization could be performed to minimize the amount of samples needed without losing accuracy. Another existing problem is the long-term reliability of a 3D-printed actuator. It is worthy to work towards digital fabrication of soft actuators using materials with longer durability. Lastly, we will also work on how to estimate the complete actuator shape based on the predicted coordinates on the inextensible layer (e.g. by using elasticity simulation).

5

Reconstructing the Deformed Shape of Soft Robots

In the previous chapter, it was demonstrated that the captured sensor signals can be used to accurately predict points that are located on the robot. However, this collection of points must be converted to a robot representation that is useful for real-time visualization as well as closed-loop control. To this end, the captured marker coordinates are converted to shape parameters that are used for training the machine learning model. The shape parameters that are predicted by the machine learning model can be used to reconstruct the shape of soft robots in real time. The calibration procedure presented in Chapter 4 is limited to static soft robot postures with two-dimensional bending deformation. In this chapter, sensing, calibration and reconstruction are demonstrated for soft robots composed of multiple actuators undergoing dynamic three-dimensional deformation. With a much larger soft robot workspace, many more training samples were needed to train the machine learning model. A motion capture system was thus deployed to rapidly collect the dynamic data.[1]

---

[1] This chapter is published as: **R. B. N. Scharff**, G. Fang, Y. Tian, J. Wu, J. M. P. Geraedts, and C. C. L. Wang, "Sensing and reconstruction of 3D deformation on pneumatic soft robots", *IEEE/ASME Transactions on Mechatronics* (***under review***), 2020. Note: a few small corrections and/or clarifications have been made to the original submitted text.

5.1 Introduction

Proprioception for soft robots is a challenging problem because of the virtually infinite degrees of freedom (DOFs) of the deformable bodies, and because there is no off-the-shelf sensor available. However, accurate proprioception is crucial for closing the loop of control. Existing solutions generally conduct a simplified model according to a specific soft robot design – e.g., sensing a single bending angle [51] or curvature [39]. A general and easy-to-fabricate solution for sensing 3D deformation is needed. In this chapter, we propose a method using low-cost sensors to realize accurate proprioception and real-time 3D shape reconstruction. Our approach is based on a data-driven strategy that can be generally applied to different designs based on their own shape parameterization.

5.1.1 Related Work

The literature is reviewed from three angles, namely sensors, deformation acquisition and machine learning.

Sensors for proprioception

A large variety of sensors have been developed for proprioception in soft robotics. For soft bending actuators, proprioceptive sensing is commonly achieved by embedding paths of conductive materials that change their resistivity upon deformation, such as liquid metal [41], a 3D-printed carbon black/PLA compound [49], [50], commercial flex sensors based on conductive ink [51], EMIM-ES ionogel [63], PDMS impregnated with carbon nanotubes [61], or laser-cut patterns from off-the-shelf conductive silicone [64]. Proprioception can also be achieved by magnetic sensing [38] and inductance-based sensing [65]. The inductance-based sensing method can also be applied to a continuum joint [66]. However, most of the sensors mentioned above cannot accommodate very large strains or cannot capture multiple DOFs, making them unsuitable for other types of actuators, such as elongational actuators or three-dimensionally deforming surfaces. Moreover, integrating these sensors into an actuator is usually cumbersome during fabrication.

The use of optical sensing for proprioception in soft robots has been shown to have great potential. Examples of optical sensing for soft robots include the stretchable optical waveguides for use in bending actuators [39], [67], macrobend optical sensing for elongational actuators [68], optical distance sensors on a helical flexible printed circuit board for a soft robotic joint [69], fiber optics in a three-dimensionally deforming surface [70], the use of fluidic channels in combination with an external camera [71], and embedded cameras for tactile sensing [72]–[74] and inflatable bellows [75]. However, some of these approaches can only sense relatively simple deformation (e.g., it is difficult to embed optical waveguides and fluidic channels inside three-dimensionally deforming surfaces or elongational actuators). Furthermore, the image-texture-based methods can only be used in large actuators because of the size of cameras.

In previous work, we demonstrated that accurate proprioception of soft robots could be achieved by integrating a light source, color sensors (photodiodes) and color patterns inside the air chambers of pneumatic bending actuators [27], [45]. Deformation of the air chamber changes the reflection and traveling distance of the light coming from the light source(s), which lead to changes in the light intensity and the colors observed by the optical sensors. A similar principle was applied for a linear bellow by using only four phototransistors [76]. Following the same working principle, we demonstrate in this chapter that accurate proprioception of three-dimensionally deformed soft robots can be realized by using only light-dependent resistors (LDRs) and light-emitting diodes (LEDs). In contrast to existing solutions, this solution can be easily integrated into many different types of soft pneumatic actuators while achieving highly accurate proprioception for soft robots interacting with their environment.

Deformation acquisition

An important challenge in sensing soft robot deformation is how to obtain accurate ground truth information in deformation. Simplified information has been sensed in prior research, including the bending angle [51], the curvature [39] and the position of the tip point [57], [60]. However, important information on the shape of a soft robot is lost. A straightforward solution is to increase the number of sensed points on the actuator. However, the number of points is limited when physical manipulators [60] or sensors (e.g., inertial measurement units [66] or electromagnetic sensors [68], [77]) are used to determine the position of each point. For these reasons, systems that capture markers on a soft robot with one or more camera sensors are a popular choice for capturing ground truth information of soft objects (ref. [45], [66], [70], [78], [79]). The captured marker coordinates on the robot can be used to reconstruct the complete shape of a soft robot [80]. Therefore, we use this approach to capture ground truth information for soft actuators with different types of deformation.

Machine learning

Due to the highly nonlinear deformation presented on soft bodies, it is difficult to build an accurate analytical sensing model for soft robots. Simplified analytical models can only be applied to a specific type of design and thus lack of generality. Machine learning methods, particularly artificial neural networks, have proved to be a powerful tool to learn these nonlinearities while being applicable to a wide range of designs. Feedforward neural networks (FNNs) have been used to learn the kinematics of soft robots [57], [58] and to characterize various types of soft sensors [45], [60], [79]–[81]. When sequential data is collected, a recurrent neural network (RNN) or long short-term memory (LSTM) network can be used to include time-variant effects such as hysteresis in the sensing model [59], [61], [64], [71]. As a powerful tool when working with camera data as sensor input, a convolutional neural network (CNN) has been employed in combination with an LSTM to calibrate a soft tactile sensor for detecting the hardness of objects [82]. We employ neural networks in our learning process to establish the mapping between the signals from sensors and the shape parameters that are extracted from the captured positions of markers.

5.1.2 Our Approach

Our approach endows soft pneumatic actuators with the sensing capability for real-time 3D shape reconstruction through four steps (see Fig. 5.1):

1. Embedding optical sensors and lamps into the air chambers of soft robots to translate deformations of the air chambers to the variation of light intensity;
2. Capturing the ground truth deformation of the soft robot using markers placed on the robot;
3. Extracting shape parameters that can represent deformation more compactly from the positions of markers;
4. Learning the mapping between the signals captured on sensors and the corresponding deformation represented by shape parameters.

To the best of our knowledge, this is the first work that provides a full pipeline for real time 3D reconstruction of pneumatic soft robots consisting of multiple

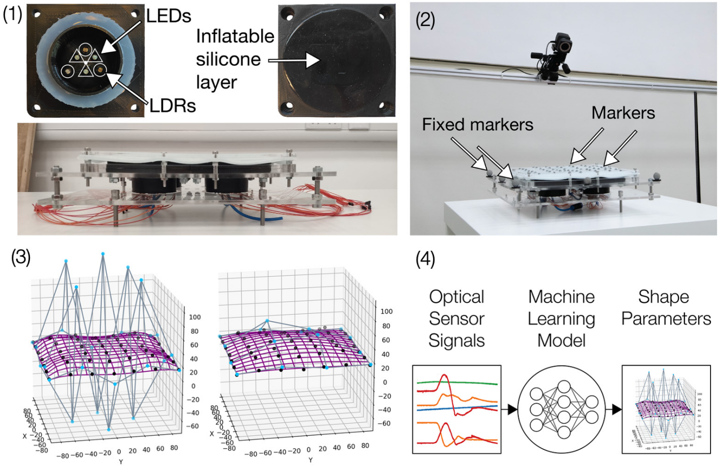

Figure 5.1: Overview of our approach for enabling the sensing capability of 3D shape on soft robots in four steps: (1) sensor integration, (2) data collection, (3) shape parameterization, and (4) learning the mapping.

interacting actuators. This was made possible due to the following technical contributions:

- Accurate proprioception method for pneumatic soft robots consisting of multiple interacting actuators undergoing 3D deformation;
- A method to efficiently reconstruct the three-dimensionally deformed overall shape by directly learning the mapping between the sensed signals and the shape parameters.

Due to the small number of sensors as well as the efficient mapping between the sensor readings and the shape parameters used for reconstruction, both the sensing and the reconstruction steps can run at 50 Hz on a consumer-level device.

Two vastly different robot designs – a robotic joint and a deformable membrane – were selected to demonstrate the flexibility of the proprioception method as well as the shape parameterization. The robotic joint is composed of three interacting bellows that can extend and bend to a great extent without presenting large material strains. As the bellows are connected to the same rigid body as end-effector, the deformation can be parameterized as a transformation matrix to compute the forward kinematics easily. On the other hand, the deformable membrane is composed of four modules that inflate the stretchable silicone layer to form a 3D freeform surface. Real-time reconstruction of free-form surfaces is challenging. In this work, shape of the deformable membrane is parameterized by the control points of a Bézier surface.

5.2 Sensing Deformation on Soft Actuators

This section explains the importance of using multiple sensors to capture the deformation of pneumatic actuators on soft robots. Deformation of an actuator with one DOF can often be captured by a single sensor. However, the signals captured by a single sensor cannot distinguish the configurations of deformation in multi-DOF actuators. Attempts have been made to increase the number of signals that can be captured by using a camera instead of single (optical) sensors (ref. [71]–[75]). For example, if images are taken at the resolution of 1280×720, this method can capture up to $1280 \times 720 \times 3 = 2,764,800$ different signals. However, in practice, the number of sensors required for capturing 3D deformation is much smaller than this as redundancy exists in sensing and computation. Besides the excessive computing time, another downside of camera-based sensing is the difficulty of integrating it into a narrow space, which is quite common in many soft actuators. In our approach, we place LEDs and LDRs inside each air chamber to capture the deformation inside a chamber. The signals captured in all chambers are later fused to reconstruct a 3D shape of the soft robot driven by these chambers.

It is important to capture the deformation on each chamber. As shown in the experiment of Fig. 5.2, the 3D transformation can already be well reconstructed even if only one bellow (i.e., the air chamber) is equipped with sensors. However, as multiple configurations exist for which a single sensor gives the same reading, a chamber should have multiple sensors to make a distinction between these configurations – see the difference between blue (only one LDR inside the bellow) and light red (with four LDRs inside the bellow). As the ends of the three bellows are connected to the same rigid frames, their deformations are somewhat coupled. Therefore, the accuracy obtained using four LDRs in one bellow already approaches that of using four LDRs in every bellow (i.e., $4 \times 3 = 12$ LDRs in total). However, this is not the case for many other soft robots with multiple actuators, such as the deformable membrane shown in Figs.5.1 and 5.4.

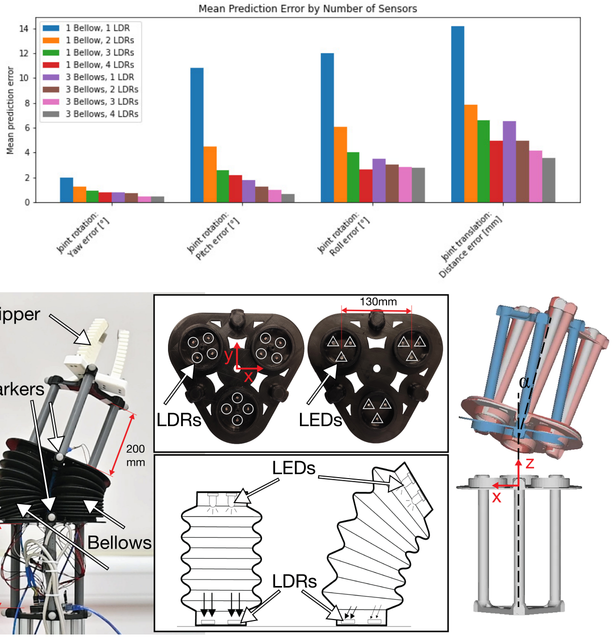

Figure 5.2: (Top row) The mean prediction errors generated by using different numbers of light-dependent resistors (LDRs) inside either only one bellow or inside all three bellows. (Bottom row) The predicted transformation is already highly accurate when using four LDRs in one bellow (light red). For the purpose of comparison, the predictions by using only one LDR in one bellow (blue) and four LDRs in all three bellows (gray) are also given. The ground truth transformation is calculated from markers located on the robot by using a motion capture system, and displayed in dark red. The layout of LDRs and light-emitting diodes (LEDs) and the illustration of their working principle are also given in the bottom row.

5.3 Soft Robot Realization

In this section, we present the realization of our sensing and reconstruction method on two different designs of soft robots. Methods for data acquisition and shape parameterization are also introduced. Lastly, we discuss the feasibility of using different machine learning approaches. The process from data acquisition to training the machine learning model is described by the framework diagram shown in Fig. 5.3, which also presents the pipeline for real-time reconstruction.

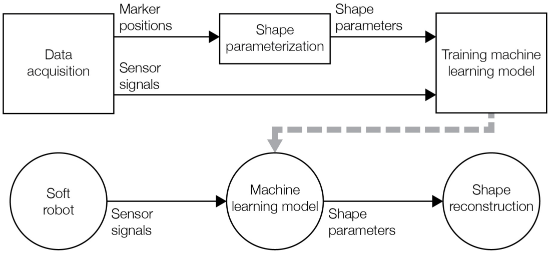

Figure 5.3: (Top) The framework diagram for training the neural network and (bottom) the pipeline for real-time reconstruction.

5.3.1 Two Soft Robots

Soft continuum joint

The design of a soft continuum joint is indicated in Fig. 5.2. The soft continuum joint is composed of three inflatable bellows, the top and bottom of which are attached to two rigid frames. The centers of these frames are connected by a cable that constrains the longitudinal expansion of the bellows such that a multi-directional bending motion can be generated upon inflating the bellows. The maximum bending angle α (see Fig. 5.2) is at least 26 degrees in all directions and the operating pressure is in the range of [0, 10] kPa. The top and bottom frame of the joint are fabricated by using fused deposition modeling (FDM) with black polyactic acid (PLA) filaments. The leads of the LEDs and LDRs are fed through small holes in the frames and sealed with epoxy glue. The bellows are off-the-shelf Freudenberg V6-00400 bellows, which are sealed around the cylindrical parts of the frame using cable ties. In each bellow, four LDRs are mounted on the bottom frame to measure the light intensity inside the bellow. This light is generated by three LEDs mounted on the top frame of each bellow. Deformations of the bellows result in variation of light intensity that is sensed by the LDRs. The change of sensed light intensity is indicated by the changed lengths of the black arrows illustrated in the inset of Fig. 5.2. This information can be used to determine the deformed shape of a bellow. As different external forces are applied to the joint when the gripper mounted on top of the arm holds different objects, rotation and translation of the joint cannot be determined from the pressure of air inside the bellows. Sensors are needed to determine the rotation and translation of the joint based on the shape variation of the bellows. Due to the application of machine learning, an accurate mapping between the sensor signals and soft robot shape can be learned regardless of variations in the sensors or their placement.

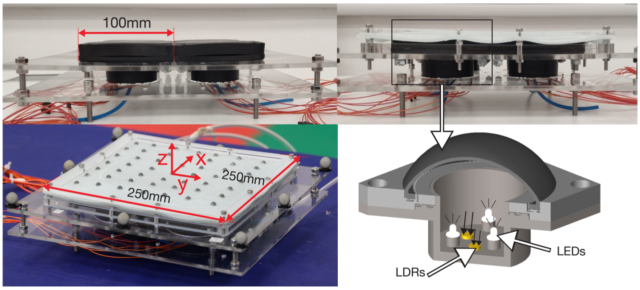

Figure 5.4: The hardware setup of the deformable membrane and its main dimensions. An illustration of the inflated module and its inner layout is shown in the bottom right.

Soft deformable membrane

The design of a deformable membrane is as shown in Fig. 5.4. This hardware setup is composed of four chamber modules that can be inflated separately. The bottom of each module is rigid and mounted with three LEDs and three LDRs. The chamber is sealed by a lid with a thin inflatable silicone layer. The modules have been fabricated using a combination of FDM and silicone casting. A mechanical interlocking structure, as proposed by Rossing et al. [83], is used to create an airtight bond between the 3D-printed part and the silicone. The silicone used is *Smooth-On Dragonskin* with a shore hardness of $30A$ colored with black silicone pigment. The filament used is black PLA. The materials were selected for their opacity in order to eliminate the influence of external lighting conditions on the sensor readings. When the chamber of a module is pressurized, the silicone layer inflates. This inflation results in a change in reflection and traveling distance of the light emitted by the LEDs, which is sensed by the LDRs. This information can be used to determine the shape of the inflated silicone. Four modules are mounted on a frame in a 2×2 layout and covered by a thin layer of silicone to create a smooth deformable membrane. The operating pressure is in the range of $[0, 15\mathrm{kPa}]$. The modules can be inflated to a height of up to $40\mathrm{mm}$. Note that as all four inflatable modules interact with the silicone layer and therefore are coupled, the shape of each module cannot be determined from the air pressure of each chamber. This effect is amplified by the highly non-linear material behavior of the silicone. Therefore, sensors are essential to determine the shape of the membrane.

5.3.2 Data Acquisition

This subsection introduces the method of generating the dataset for training.

Setup for data acquisition

A motion capturing system of Vicon was used to capture a number of strategically placed markers on the soft robots. For the soft continuum joint, markers were placed at the top and the bottom frame of the joint (see Fig. 5.2). For the soft deformable membrane, a layout of 7×7 markers was placed on top of the membrane. Additional markers were placed on the rigid frame as reference points for sensing its orientation. These markers are illustrated in Figs. 5.1 and 5.5. Upon data collection, the positions of markers were collected at a frequency of 100 Hz, whereas data of all 12 LDRs was collected at a frequency of 1000 Hz. The data was synchronized using the Vicon Lock Sync Box.

Sampling strategy

A good sampling scheme that spans the robot's workspace as well as a wide range of external loads was found crucial to prevent overfitting in data-driven learning. For the soft continuum joint, a range of weights were added on top of the actuator to enable accurate predictions when different external loads were applied to the joint. The weights held by the gripper on top of the arm varied from 0 to $500\mathrm{g}$ in steps of $50\mathrm{g}$. A total of $242,131$ samples were collected in $40\mathrm{m}21\mathrm{s}$. Note that each sample refers to a collection of the markers' positions. The data collection was divided into three batches. These batches were collected at different times of a day and with an altered orientation and position of the soft robot in the room to guarantee independence of external lighting conditions and the calibration of the motion capturing system. For the deformable membrane, the actuation sequence was varied to ensure that samples can span the entire working space. The data was collected in two batches with varying positions and orientations of the robot as well as varying lighting conditions. A total of $44,403$ samples were collected in $7\mathrm{m}24\mathrm{s}$ for the soft deformable membrane.

Data Preparation

Before further processing of the data, the captured marker positions were converted into a more convenient system aligned with the robots. The origin of the soft continuum joint was selected as the center of the bottom triangle of the joint. The z-axis was aligned with the triangle's normal pointing upwards, the y-axis pointed from origin towards one of the markers, and the x-axis was then defined as orthogonal to these two axes (see Fig. 5.2). For the soft deformable membrane, the centroid of the fixed markers on the frame was selected as the origin. The axes were defined such that the x- and y-axes aligned with the frame's boundary and z-axis pointed upwards.

5.3.3 Shape Parameterization

The most intuitive way to present the shape of a deformed soft robot is to describe it by the predicted locations of markers [45]. However, this approach is redundant in many scenarios. Two shape parameterizations are introduced below for the hardware setups employed in our work, which provides a more compact and effective way to reconstruct the shape of deformed soft robots.

Soft continuum joint

A parameterization with physical meaning is demonstrated for this hardware setup. The collected marker positions are converted to a rigid transformation represented by a rotation matrix $\mathbf{R}$ together with a translation vector $\mathbf{T}$, which describe the rotation and translation from the bottom triangle of the joint to the top triangle of the joint. For a set of points (i.e., markers) on the bottom triangle denoted as $\{\mathbf{m}_i\}$ and the corresponding set of points on the top triangle as $\{\mathbf{d}_i\}$, the mapping between them can be described as

$$\mathbf{d}_i = \mathbf{R}\mathbf{m}_i + \mathbf{T} + \mathbf{v}_i \tag{5.1}$$

where $\mathbf{v}_i$ is a noise vector to incorporate the errors of marker placement and measurement. The best solution of $\mathbf{R}$ and $\mathbf{T}$ can then be determined by the unit-quaternion approach in the sense of minimizing a least-squares error (ref. [84]). The set of $(\mathbf{R}, \mathbf{T})$ determined from motion capture are used as samples for training and testing.

Soft deformable membrane

For the soft deformable membrane, a parameterization based on Bézier surfaces is conducted to represent its shape more compactly than by the positions of markers on the robot. The positions of 7×7 ($N = 49$) markers are used to provide raw data for presenting the shape of a deformed membrane. A surface fitting process is conducted to generate the control points of a Bézier surface patch for describing the shape. In general, a Bézier surface maps parameters (u, v) to surface point coordinate $\mathbf{p} \in \Re^3$ as

$$\mathbf{p}(u, v) = \sum_{i=0}^{m} \sum_{j=0}^{n} B_{i,m}(u) B_{j,n}(v) \mathbf{c}_{i,j} \tag{5.2}$$

where $\{\mathbf{c}_{i,j}\}$ are control points of the surface and $B_{i,m}(u)$ and $B_{j,n}(v)$ are Bernstein basis polynomials defined as

$$B_{i,m}(u) = \tbinom{m}{i} u^i (1-u)^{m-i}. \tag{5.3}$$

For this hardware setup, the positions of markers can be captured by the motion capture system. For a marker with position $\mathbf{p}_k$, we can determine its parameters (u_k, v_k) by the marker's planar coordinate when the membrane is flat – that is, before pumping air into the chambers. The control points can be determined by minimizing the following energy, which measures the square distances between the real coordinates of markers (captured by cameras) and the positions obtained by surface description

$$E = \sum_{k=0}^{N-1} (\mathbf{p}_k - \sum_{i=0}^{m} \sum_{j=0}^{n} B_{i,m}(u_k) B_{j,n}(v_k) \mathbf{c}_{i,j})^2. \tag{5.4}$$

With the help of Bézier surface fitting, the deformable membrane could be expressed as the linear combination of several control points, thus removing the redundant information embedded in the marker positions. Moreover, this compact representation is more robust to noises and outliers. The accuracy of the shape representation is dependent on the number of control points of the Bézier surface. As the Bézier surface is a special case of B-spline surface, the extension to a B-spline surface is also straightforward. However, increasing the number of control points means that more information needs to be generated from the sensed signals. As a result, a more complex machine learning model is needed, and such a model generally must also be fed by more training samples. As the dataset is obtained through physical experiments, the collection of additional samples is time-consuming and thus expensive. Figure 5.5 displays a comparison of the fitting of a Bézier surface with 16, 25, and 36 control points. It can be seen that a Bézier surface with 5×5 control points can already describe the deformable membrane with accuracy at a satisfactory level.

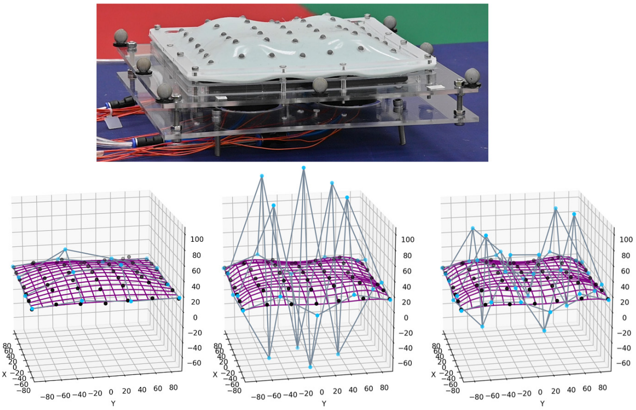

Figure 5.5: Surface fitting for a deformed surface (top row) with 49 markers' positions determined by a motion capture system. The results by using 4×4, 5×5, and 6×6 control points are given from left to right (bottom row). The black points indicate the measured coordinates of markers, the blue points present the control points obtained by surface fitting and the fitted Bézier surfaces are visualized as the purple grids.

5.3.4 Machine Learning

Machine learning is applied to learn the relationship between the sensor data and the shape-oriented parameters. We studied different learning models to determine the best model for different hardware setups. For this purpose, accuracy was tested on different trained models, including an LSTM network, an FNN, a support vector regression (SVR), and a multivariate linear regression (MVLR). The network design of these models is presented below.

- The LSTM network has a hidden layer of 50 neurons with $\tanh(\cdot)$ as the activation function. In the output layer, a linear function is used for learning the translation and the control points of the Bézier surface, while $\tanh(\cdot)$ is employed for learning the rotation matrix.
- For the learning model by FNN, we also use a hidden layer of 50 neurons with sigmoid as the activation function. The output layer is designed identical to the LSTM network.
- For SVR, we chose standard radial basis functions (RBF) as kernels and used 1.0 as the C-parameter for regularization.
- An ordinary least squares multivariate linear regression is used for MVLR.

For the soft deformable membrane, we obtained the datasets for training, validation, and testing from the readings from 12 sensors in 10 subsequent

Table 5.1: Datasets for Machine Learning

	# Samples in Different Datasets		
Hardware Setups	Training	Validation	Test
Continuum Joint	$168,251$	$50,510$	$23,370$
Deformable Membrane	$21,396$	$11,503$	$11,504$

time-steps at 1000 Hz, resulting in $12 \times 10 = 120$ readings as input for each prediction. Positions of markers were captured by cameras and converted into control points of a Bézier surface – specifically, we generated different control polygons with 4×4, 5×5, and 6×6 to explore the best result. To verify the generality of a learning model's performance, the actuation sequence that was used to generate the dataset of the test must be different from the actuation sequence used to generate the training dataset. For the soft continuum joint, the datasets were also obtained from the readings from 12 sensors and the captured positions of markers in 10 subsequent time-steps at 1000 Hz, again resulting in $12 \times 10 = 120$ readings as input for each prediction. The positions of markers were converted into a rotation matrix and a translation vector to form a sample. The performance of learning models was evaluated on the dataset captured while external loads were applied. Note that these specific external loads were not applied while generating training data so that the generality of a learning model is well verified. The total numbers of samples in different datasets and the comparison of mean prediction errors are given in Table 5.1.

5.4 Results

This section presents the experimental results of applying our approach on the two hardware setups – the soft continuum joint and the soft deformable membrane. Quantitative analysis was conducted to verify the performance of our method. The performance of different machine learning models is compared and displayed in Fig. 5.6 for the soft continuum joint and the soft deformable membrane. It is found that both LSTM and FNN perform well in general. However, we did not find clear indicators to predict which of these two networks will perform better on a specific shape parameterization.

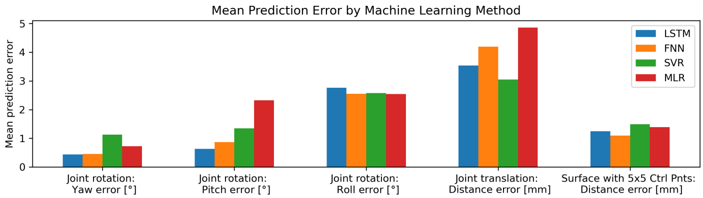

Figure 5.6: Comparison of the mean prediction errors by using different learning models for the soft continuum joint and the soft deformable membrane.

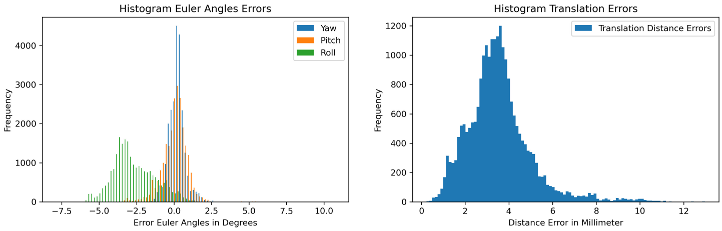

Figure 5.7: Histograms of the prediction errors for the rotation (left) and the translation (right) of the soft continuum joint, where the prediction is generated by the LSTM network.

5.4.1 Soft Continuum Joint

To provide a more meaningful interpretation of the errors in the rotation matrix, the prediction errors of a rotation matrix are translated to Tait-Bryan Euler angles following the z-, y'-, and x''–convention (intrinsic rotations) – referred to as yaw, pitch, and roll respectively. The best performance was achieved using the LSTM with mean prediction errors as 0.44, 0.63, and 2.76 degrees in yaw, pitch, and roll, respectively. Prediction error of the translation vector is evaluated by the error vector's magnitude. According to the evaluation of the test dataset, SVR gives the smallest error as $3.05\,\mathrm{mm}$. LSTM's error is $3.53\,\mathrm{mm}$, which is comparable to SVR. Therefore, by combining rotation and translation, the LSTM learning model provides the best performance. Mean prediction errors and their distribution are shown in Fig. 5.7.

A side-by-side comparison of the reconstructed joint and the real joint position for a time sequence of 16 seconds is shown in Fig. 5.8 and also the supplementary video. This reconstruction is based on the predictions obtained from the LSTM model, which demonstrate the capability of accurate prediction regardless of the external load.

A prediction for the rotation and translation can be generated within $4\,\mathrm{ms}$

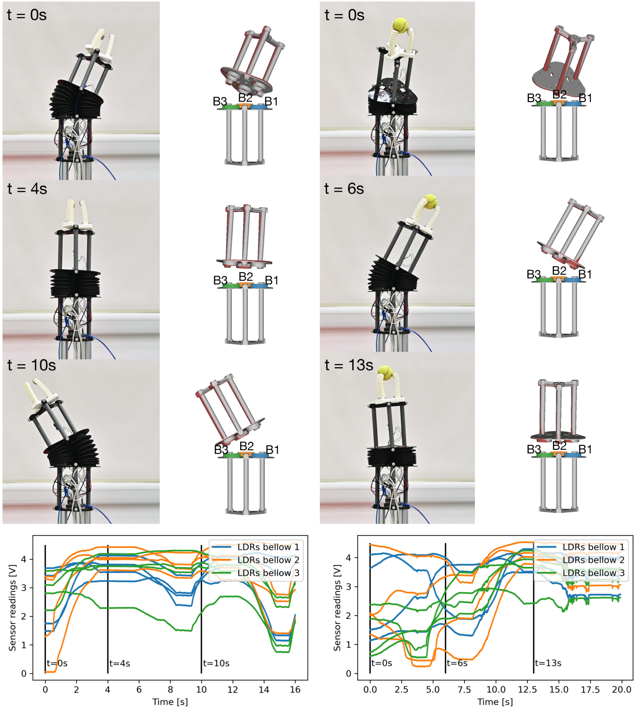

Figure 5.8: Comparison of the rotation and translation predicted by the LSTM network on the continuum joint and the actual rotation and translation (obtained from motion capture) for a sequence without external load (left) and with external load (right). The transformation obtained from motion capture is displayed in dark red, while the reconstructed transformation from LSTM prediction is rendered in gray. LDRs sensor readings in different modules throughout the time sequences are shown at the bottom. Bellows and their corresponding set of LDR sensor readings are visualized in matching colors.

on a consumer-level device (i.e., a laptop PC with 2.3GHz CPU + 16GB RAM), whereas the calculation of the forward kinematics is very fast. In practice, the sensor readings can be obtained at the rate of 1000 Hz, and each prediction is made by using readings from 10 time-steps. Therefore, we can make a prediction in a single-thread computation (see the bottom row of Fig. 5.3) every 14 ms, which makes it possible to run the reconstruction in real-time (at the rate of 50 to 70 Hz). The speed of visualizing deformed 3D models as shown in Fig. 5.8 depends on the mesh density.

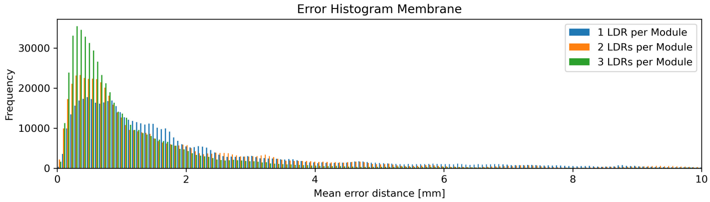

Distance Errors	1 LDR	2 LDRs	3 LDRs
Mean Values	$2.21\mathrm{mm}$	$1.79\mathrm{mm}$	$1.18\mathrm{mm}$
Standard Deviation	$2.44\mathrm{mm}$	$2.06\mathrm{mm}$	$1.39\mathrm{mm}$

Figure 5.9: Histogram showing the distribution of the distance errors between the real and the predicted marker positions for the samples in the test dataset when using different numbers of LDRs in each module.

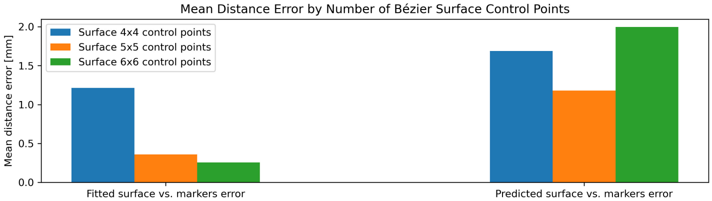

Figure 5.10: Comparison of the mean distance error for the fitted surface vs. the captured markers, and the predicted surface vs. the captured markers on Bézier surfaces with different numbers of control points.

5.4.2 Soft Deformable Membrane

The prediction error of the soft deformable membrane is indicated on the right side of Fig.5.6. For each marker, its uv-parameters can used to generate the marker's position on the predicted surface. The distance between the real position of a marker (obtained from motion capture) and its predicted position is employed as a metric to evaluate the error. When comparing the mean errors, FNN gives the best result with 1.18 mm as the mean of distance errors. An error histogram is given in Fig. 5.9. It is also interesting to study the influence of different numbers of sensors. Therefore, we also generated results by the test dataset using only two LDRs and one LDR per module. Their corresponding error histograms are also shown in Fig. 5.9. It can be observed that the mean distance error by using only one LDR within each module is nearly twice the error when using three LDRs.

We also studied the errors by using different numbers of control points for

Bézier fitting. The errors were measured as the distances between the positions of markers and their corresponding points on the resultant surface of fitting. It is obvious that more control points lead to less fitting error (see the left side of Fig. 5.10). However, the error of a surface (with 6×6 control points) predicted from sensor readings can be larger than the error on a surface with 5×5 control points (see the right of Fig. 5.10). The reason is twofold. First of all, the surface fitting error of 5×5 is already very close to the error of 6×6. Secondly, the information from 12 sensors is not sufficient to predict 36 control points. Therefore, we used 5×5 control points to represent and reconstruct the soft deformable membrane.

A visual comparison of the physically deformed membrane and the reconstructed surface over a period of 29 seconds can be found in Fig. 5.11 and also the supplementary video. The surface is predicted by FNN from the light intensities captured by LDRs in each module. The distance errors between the surface predicted from sensor readings and the surface generated by fitting camera captured positions of markers are visualized as color maps.

Prediction of the control points from sensor readings can be generated within $1\ \mathrm{ms}$ on a consumer-level device. Again we made a prediction by using the readings from 10 time-steps, which is captured at the rate of 1000 Hz. The speed of visualization as shown in Fig. 5.11, strongly depends on the density of the grid – for example, a visualization with a 30×30 grid can be generated within $6\mathrm{ms}$ using a C++ implementation. Incorporating all these computations, our system can be operated in real-time at the rate of more than 50 Hz.

5.5 Conclusion

In this chapter, we presented a method to sense and reconstruct 3D deformation on pneumatic soft robots composed of multiple actuators. Our method is based on integrating multiple low-cost sensors inside the chambers of pneumatic actuators and then using machine learning to fuse the captured signals into shape parameters of the soft robots. These shape parameters can be used to efficiently reconstruct the 3D shape of the soft robot. The sensing and shape prediction pipeline can run at 50 Hz in real time on a consumer-level device. This is an important step towards the development of more advanced closed-loop control for soft robots.

In this work, LDRs were chosen to capture the changes in light conditions. It should be noted that the resistivity of these semiconductors changes with temperature and humidity. In our experiments, this did not raise any issues

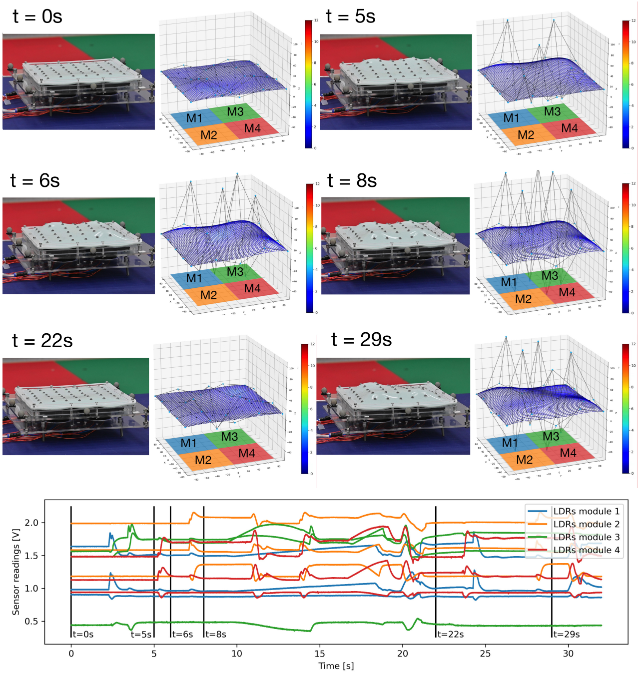

Figure 5.11: Visual comparison of the FNN predicted surface represented by 5×5 control points and the physically deformed soft membrane during a time sequence of 29 seconds. The positions of markers obtained from motion capture are displayed in black dots, while their corresponding points on the predicted surface are connected by red line segments. The errors between the predicted surface and the captured surface (by fitting camera-captured positions of markers) are visualized as color maps. The sensor readings of the LDRs within the different modules throughout the time sequence are shown in the bottom graph. Modules and their corresponding set of LDR sensor readings are indicated in matching colors.

when testing under mildly varying (room temperature) conditions. If a robot is required to operate under severe temperature changes, it is recommended to replace the LDRs with photodiodes as our previous work [45] or to add a temperature sensor for further calibration. Future research could investigate the use of transfer learning to reduce the required number of new training samples when a minor modification is applied to a design. Lastly, the simulation of light variation inside the air chambers could be a promising direction for optimizing the placement of the optical sensors and the light sources inside air chambers. This simulation could also be used for integrating other effective signal generators, such as color patterns [27], to further increase the accuracy of proprioception.

6

Restraining Superfluous Degrees of Freedom of Soft Robots

This research cycle addresses the restraining of superfluous degrees of freedom in soft robots. In Chapter 2, it was demonstrated that a range of different actuation behaviors could be realized by modifying the shape of the air chambers. However, the fingers of the soft robotic hand had a tendency to slip as a result of out-of-plane deformation. In soft robotic manipulators, this out-of-plane deformation is a major cause of failed grasps. In this chapter, the problem of out-of-plane deformation in soft pneumatic actuators is demonstrated and a method for reducing the out-of-plane deformation is developed. This is achieved through embedding a structure inspired by spatial flexures in the 3D-printed soft actuator. This structure reduces the out-of-plane deformation without significantly increasing the in-plane bending stiffness.[1]

---

[1] This chapter is published as: **R. B. N. Scharff**, J. Wu, J. M. P. Geraedts, and C. C. L. Wang, "Reducing out-of-plane deformation of soft robotic actuators for stable grasping", in *2019 2nd IEEE International Conference on Soft Robotics (RoboSoft)*, 2019, pp. 265–270

6.1 Introduction

One practical application of soft robots is to pick and place objects in unknown environments. In soft robots, the grasping motion is often realized by the bending of soft pneumatic actuators, induced by the inflation of air chambers that are made of soft material [13], [17], [86], [87]. While the soft actuators are designed to bend in a specific direction, their flexibility allows them to deform in other directions when the reaction force from the objects is asymmetric – that is, not in the plane of intended bending. As illustrated in Fig. 6.1, out-of-plane deformations include sidewards bending (B) and a combination of bending and twisting (C). This type of deformation is not typically observed either in human hands or in conventional rigid robotic grippers [2], [7], [88], [89]. Both rigid robotic grippers and human hands, composed of rigid phalanxes connected by joints, have a limited number of degrees of freedom (DOFs). In contrast, soft pneumatic actuators have a large number of DOFs which allows complex deformation when they are confronted with different loading conditions. As soft actuators are intended to operate in situations where the shape and position of objects are unknown, the chance of having these asymmetric loadings is high.

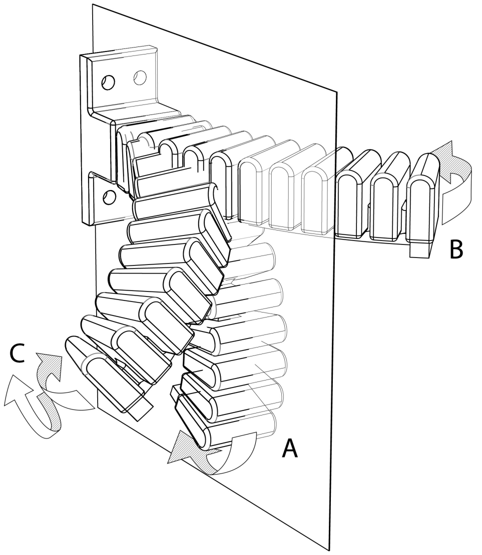

Figure 6.1: Besides in-plane bending (A), the flexibility of soft pneumatic actuators allows out-of-plane deformations including sidewards bending (B) and a combination of bending and twisting (C), which could reduce the stability of grasping.

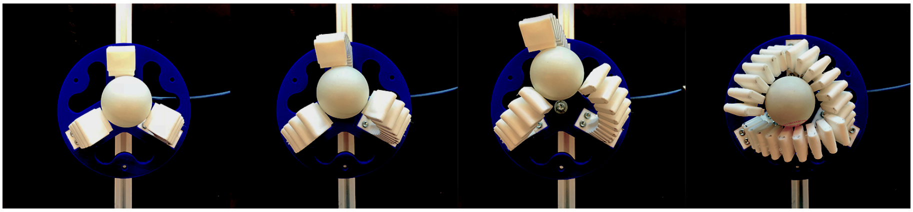

Figure 6.2: A three-fingered soft pneumatic gripper failed to grasp a spherical object due to the progressive out-of-plane deformation. Slipping occurs at a pressurization of about $400\,\mathrm{kPa}$.

Instability of soft grippers due to out-of-plane deformation was discussed at the early stage of soft robotics research [90]. Dexterous grasping using soft pneumatic actuators revealed significant out-of-plane deformations [18]. A sensorized version of the soft hand confirmed that significant twisting and lateral bending occur when grasping a spherical object [42]. In line with this, in Fig. 6.2 we demonstrate that a three-fingered soft pneumatic gripper failed to stably grasp a sphere due to the out-of-plane slippage of the actuators. Similar failure is also reported for a four-fingered gripper [41], [90].

The out-of-plane behavior is often not reported during evaluation of soft pneumatic actuators. For example, force measurements of soft pneumatic actuators are commonly performed using symmetric loadings [17], [91], [92]. Furthermore, optimization of the actuators commonly focuses only on the in-plane deformation [17], [93], neglecting the consequences of the design changes on the out-of-plane behavior of the actuator.

In early works spring models were developed to understand slipping phenomena of soft grippers [90], [94]. Morrow et al. [41] suggested the use of lower friction fingertips to prevent some out-of-plane slippage. This comes with a loss of desired in-plane friction as well. To reduce out-of-plane deformation, a simple way is to increase the stiffness by fabricating the actuators using stiffer materials. However, this also increases the in-plane stiffness and therefore requires a higher actuation effort. Anisotropic stiffnesses can be created using paper layers [17], or fiber reinforcements [43]. However, it is not known how these principles can be applied to reduce out-of-plane deformation. Different from existing works, we improve grasping stability by structural design that increases out-of-plane stiffness without modifying the in-plane stiffness.

6.1.1 Our approach

In this chapter, we approach the problem of out-of-plane deformation by structural analysis. Our purpose is two-fold. First, we demonstrate the effects of out-of-plane deformation on the grasping stability of soft actuators (Section 6.2). This demonstration, through the physical experiments and numerical simulations, is performed on a pair of actuators which have the same in-plane bending stiffness but different stiffnesses to out-of-plane deformation. We evaluate these actuators in terms of exerted forces when they bend towards a flat and an angled surface. This demonstration serves as a guideline for structural optimization of soft actuators.

Second, we propose a stiffening structure to increase the out-of-plane stiffness (Section 6.3). This stiffener pattern has a marginal in-plane bending stiffness, but provides strong resistance to the out-of-plane deformation. Our design is inspired by the spatial flexures [95]–[97]. The improved actuator is fabricated by 3D printing using a single material, and is verified by physical experiments (Section 2.5).

6.2 Out-of-Plane Deformation

This section is dedicated to demonstrate and analyze the importance of the resistance to out-of-plane deformation for stable grasping. The out-of-plane slipping of soft pneumatic actuators includes the effects of sidewards bending, twisting and twist-coupled bending. The influences of these deformations to the stability of grasping depend not only on the actuator design but also on the loading that is applied. Moreover, the actuator's stiffness with regards to these deformations changes over the actuation range. Analytical description of such complex deformation is difficult. Our approach thus mainly relies on physical experiments and numerical simulations.

To isolate the out-of-plane deformation from other factors, we test a pair of actuators which have an equal stiffness to in-plane bending, but with different stiffnesses to out-of-plane deformation. Building upon a commonly used type of soft actuators as the basis, an extra beam is added to its inextensible layer (see Fig. 6.3). The extra beam is placed along the full length of the actuator. For small in-plane deflections, the radius of curvature R of a beam is calculated by

$$R = \frac{EI_z}{M}, \tag{6.1}$$

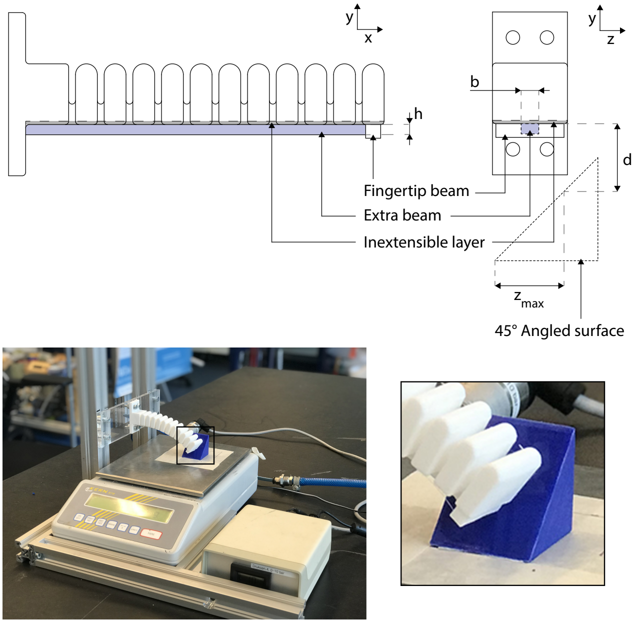

Figure 6.3: Experimental setup. We measure the vertical component of the in-plane force for an actuator interacting with an object. In this scenario, the object has a 45° angled surface.

where E and M are Young's modulus and the applied bending moment, respectively [98]. I_z is the area moment of inertia around the z-axis,

$$I_z = \frac{bh^3}{12}, \tag{6.2}$$

where b indicates the base width and h indicates the height of the beam.

We compare two beams with different dimensions of the cross-section, one with a width $b = 20\,\mathrm{mm}$ and a height $h = 2\,\mathrm{mm}$, and the other one with $6\,\mathrm{mm} \times 3(\approx \sqrt[3]{80/3})\,\mathrm{mm}$. The height is designed smaller than the width to prevent buckling on the beams. The area moment of inertia for in-plane bending, I_z, for these two beams is the same. In contrast, the area moment of inertia for sidewards bending (I_y) has a difference of around 25 times – with the one having $b = 20\,\mathrm{mm}$ being stiffer. This is calculated by switching b and h when considering another bending direction.

The torsional stiffness of the actuator is also changed when different beams

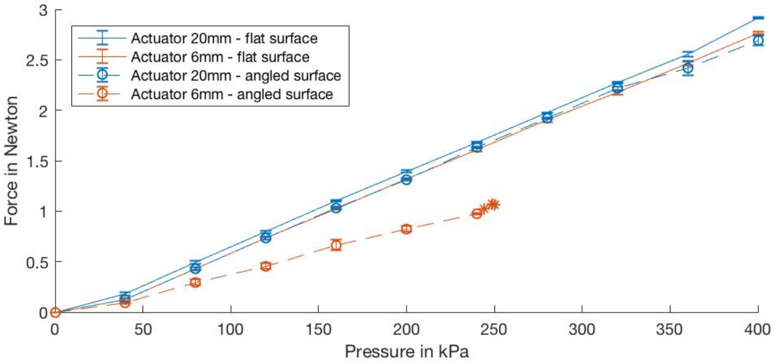

Figure 6.4: Vertical component of the in-plane forces exerted by an actuator having a $6\,\mathrm{mm}$ beam (blue) or a $20\,\mathrm{mm}$ beam (orange). When confronted with a flat surface (symmetric loading), the exerted forces as represented by solid curves are nearly the same for both actuators. When confronted with an angled surface (asymmetric loading), the actuator with $20\,\mathrm{mm}$ beam exerts comparable forces (dashed, blue) as in the case of symmetric loading. In contrast, the actuator with $6\,\mathrm{mm}$ beam exhibits smaller forces (dashed, orange) and fails to consistently exert a force when the pressure is larger than $240\,\mathrm{kPa}$.

are attached. The torsional stiffness k of a beam can be calculated by

$$k = \frac{J_T G}{l} \tag{6.3}$$

where l is the beam's length, G is the shear modulus and J_T is the torsional constant. When $b \geq h$, the torsional constant of a rectangular cross-section can be approximated by

$$J_T \approx bh^3\Big(\frac{1}{3} - 0.21\frac{h}{b}\Big(1 - \frac{h^4}{12b^4}\Big)\Big) \tag{6.4}$$

with an error not greater than 4% (ref. [98]). Therefore, the torsional stiffness of the $20\,\mathrm{mm}$-width beam is around 35% higher, which is also good against the unwanted out-of-plane deformation.

To ensure identical contacts with the object in the presence of variably sized beams, we add a fingertip-beam along the z-axis to the free-end of the actuator. Both actuators are fabricated by a 3D printer using *Fused Deposition Modeling* (FDM). A flexible filament (Ultimaker TPU 95A) is used.

6.2.1 Experimental Analysis

To quantify the actuator's resistance to different deformations during grasping, we test the force exertion of the actuators on a flat surface (symmetric loading) and a surface under an angle of 45 degrees (asymmetric loading, cf setup in Fig. 6.3). The contact surfaces of both objects have been printed flat on the printbed to ensure identical friction coefficients. The distance (d) between the first contact and the tip of the actuator (i.e., the inextensible layer) is $20\,\mathrm{mm}$. When the actuator is pressurized, it exerts a force to the flat (or inclined) surface. The vertical component of this force is recorded. We progressively increase the pressure by using $40\,\mathrm{kPa}$ pressure intervals. As the actuators show very slow slipping, we wait 10 seconds at each pressure before recording the corresponding force. When the actuator bends towards the inclined surface its free-end slips down along the surface. We consider the actuator as slipped away when its sidewards displacement reaches $20\,\mathrm{mm}$ ($\mathrm{z}_{\mathrm{max}}$, cf Fig. 6.3). Each actuator is tested three times. Here we purposely measure the contact interaction when the actuator is already in a bent configuration, as this more closely simulates a real grasping situation. The actuator's stiffness with respect to the out-of-plane deformations such as sidewards bending and twisting usually decreases rapidly when the bending of the actuator is increased.

The experimental results are shown in Fig. 6.4. The solid curves represent the measured vertical forces under symmetric loadings. These two curves are very close. This confirms that the in-plane bending behavior of actuators with the same I_z (Eq.(6.2)) is almost identical. The dashed curves are corresponding to vertical forces when the actuators are confronted with an angled surface, i.e., an asymmetric loading condition. The actuator with a wider beam is still able to exert a large force. In contrast, the other actuator slipped away before the pressure reaches $250\,\mathrm{kPa}$, and failed to apply a large force onto the angled surface. Slippage points are indicated with a star in Fig. 6.4. This comparison reveals the importance of the out-of-plane stiffness for grasping stability.

6.2.2 Numerical Simulation

We further verify the different behaviours in deformation by using numerical simulation.

First of all, the tensile properties of the material (Ultimaker TPU 95A) were determined from experiments. A total of 10 dumb-bell test pieces were 3D printed in different XY-orientations on the printbed. We used a test length

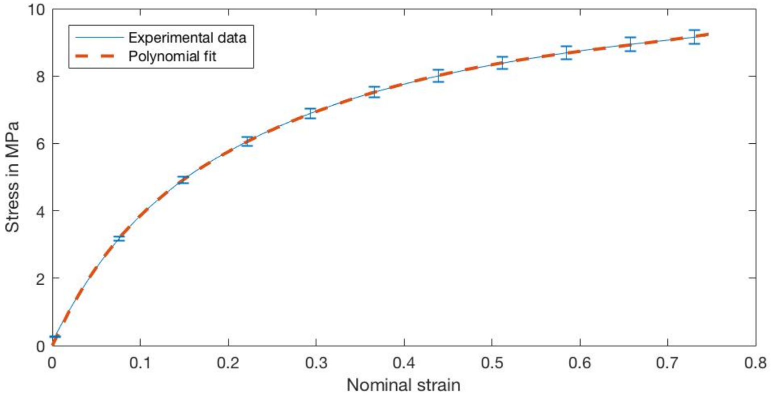

Figure 6.5: Average stress-strain relationship for 10 TPU 95A dumbbells and fitted nonlinear material model.

of $25\,\mathrm{mm}$ and a test speed of $500\,\mathrm{mm/min}$, according to the ISO 37 norm (test piece type 1). The (average) stress-strain relationship is plotted in Fig. 6.5. As the material behavior is nonlinear, a second order polynomial strain energy function was selected to fit the measured data. The friction coefficient was estimated through a sliding test. The slipping point of the Ultimaker TPU 95A surface on an angled surface of smooth PLA (all obstacle contact surfaces are printed flat on the buildplate) was determined at 25 degrees. Therefore, the static friction coefficient was determined at $\mu = \arctan(25°) \approx 0.47$. The pressure is increased slowly in our experiments to assume the static friction holds.

Numerical simulations were performed using ABAQUS. The NLgeom option in ABAQUS is used to enable simulating large displacements. The actuator and the obstacle have been positioned in the same configuration as shown in Fig. 6.3. For the angled obstacle, we use a finite sliding formulation. For the flat obstacle, we use a small sliding formulation. We also include the effect of gravity on the actuator and detect self-contact between the bellows. After applying a pressure of $400\,\mathrm{kPa}$ to the actuators. We output the in-plane components of the forces due to the contact pressure and the frictional stress on the obstacle.

The simulation results are reported in Figs. 6.6-6.8. Fig. 6.6 confirms that the $6\,\mathrm{mm}$ beam actuator and $20\,\mathrm{mm}$ beam actuator exhibit the similar in-plane bending in the absence of obstacles. Fig. 6.7 (a) and (c) show that the actuators deform similarly when they are resisted by a flat surface. When they are

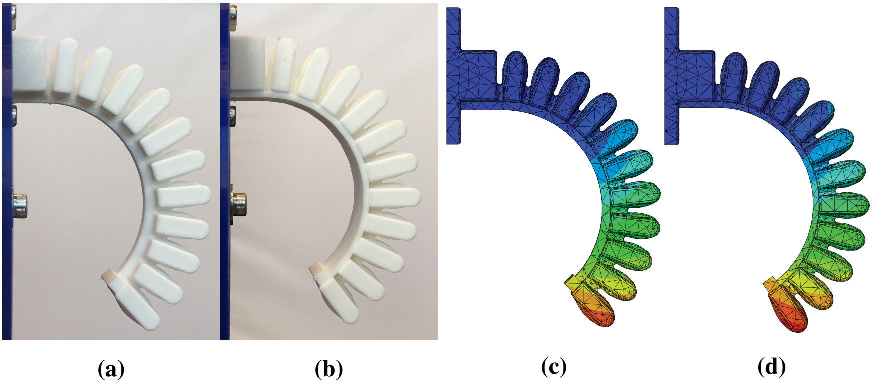

Figure 6.6: The actuator with a 6 mm-width beam (a) and the actuator with a 20 mm-width beam (b) show almost identical bending behavior (demonstrated at a pressure of 400 kPa). The simulation results ((c) & (d)) agree with the physical experiments. The colors projected on the deformed actuators indicate the magnitude of the spatial displacement of the nodes, ranging between 0 mm (dark blue) and 120 mm (dark red) for all simulation results.

confronted with an angled surface, the actuator with a 6 mm beam, Fig. 6.7(b), has a larger sidewards deformation than the one with a 20 mm beam (d). The vertical contact forces in numerical simulations are plotted in Fig. 6.8. Similar to the physical test results plotted in Fig. 6.4, it shows that the actuator with the 6 mm beam failed to exert a larger force on the angled surface (dashed orange curve). Although the simulation of contact force on a flat surface is in good agreement with the physical tests shown in Fig. 6.4, the simulation for the cases with the angled surface agrees less well with the forces measured in physical experiments. This indicates the difficulty of simulating the slipping phenomenon, and therefore the need for conducting physical experiments.

6.3 Reducing Out-of-Plane Deformation

In the previous section, it has been demonstrated that a smaller out-of-plane deformation is beneficial for maintaining a firm contact with objects while under the same in-plane bending stiffness. Thus, it can potentially improve grasping stability. In the experiments, we increased the relative stiffness to out-of-plane deformation through an extra beam that was attached to the inextensible layer, which necessitates a higher actuation effort.

In this section, we present a newly designed stiffening-structure which has

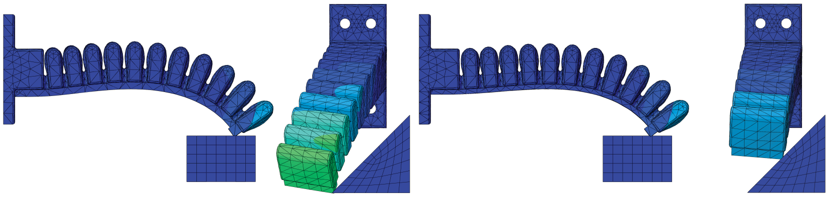

(a) (b) (c) (d)

Figure 6.7: Simulated deformation of the actuator with a $6\,\mathrm{mm}$-width beam ((a) & (b)) and the one with a $20\,\mathrm{mm}$-width beam ((c) & (d)). An obstacle with a flat surface ((a) & (c)) or an angled surface ((b) & (d)) is in the way of bending. The deformation results are similar in the case of a flat surface, while in the case of an angled surface the actuator with a $20\,\mathrm{mm}$-width beam (d) shows a smaller sidewards deformation.

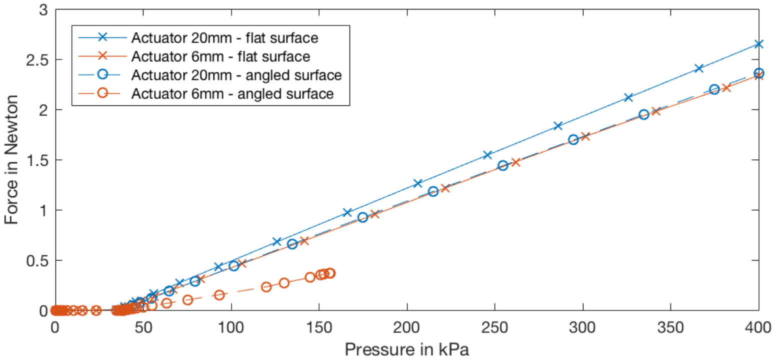

Figure 6.8: Simulated vertical force between the actuators and the flat or angled surface.

marginal effects on the in-plane bending but significantly increases the out-of-plane stiffness. The structure is shown in Fig. 6.9. The design is inspired by the infinity-flexure presented in [96]. We use the inextensible layer as the main flexure and add auxiliary flexures in perpendicular direction between each bellow segment. Then, the auxiliary flexures are connected at the ends through additional elements. Loading the actuator in torsion r_{x_l} will load the auxiliary flexures in the constrained r_{y_l}-direction (see Fig. 6.9). As the auxiliary flexures are connected in series, their deflection angle is much smaller than the total deflection angle of the actuator α, thereby limiting the decrease of stiffness in r_{y_l}-direction. This ensures that the actuator retains a significant torsional stiffness at large deflection angles. At the same time, the auxiliary flexures barely increase the bending stiffness about the r_{z_l}-direction.

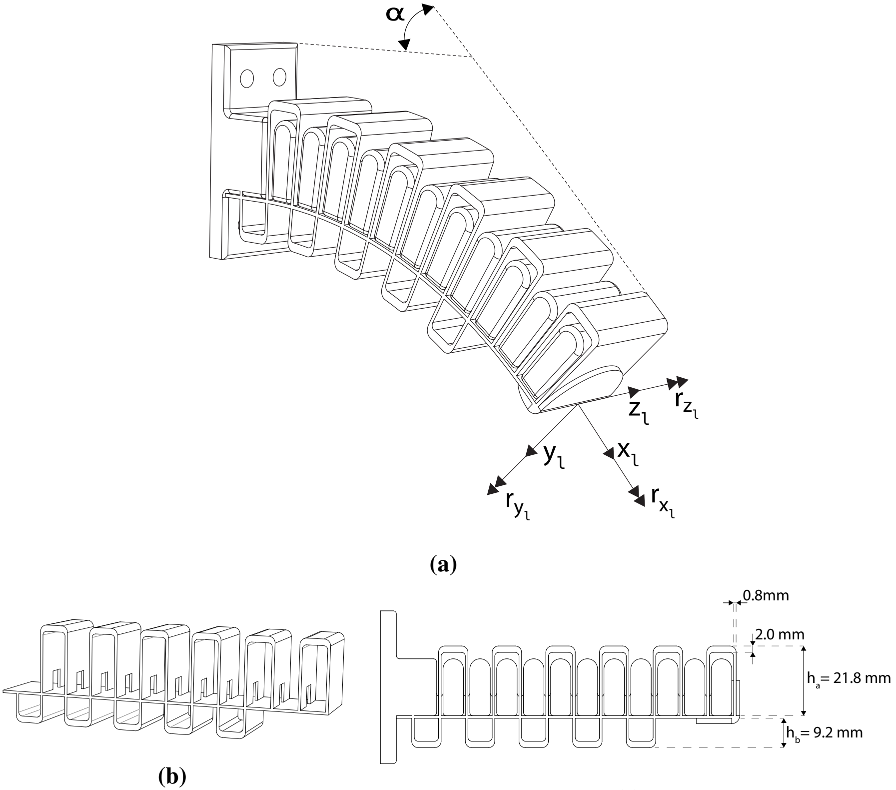

(a)

(b)

(c)

Figure 6.9: The improved soft actuator design with stiffening structure.

The heights of the auxiliary flexures above and below the inextensible layer are empirically determined and indicated in Fig. 6.9. A smaller height h_b increases the in-plane bending stiffness. However, a large h_b results in severe self-contact when the actuator bends forward. At the fingertip, no auxiliary flexures are added below, to avoid undesired interaction between the flexures and the grasping targets. We note that the upper auxiliary flexures are beneficial for forward bending. Collisions between the flexures and the expanding bellows effectively increase the elongation of the extensible layer, thus improving the bending performance [17]. On the other hand, these flexures reduce the range for reverse bending, which is sometimes required for grasping larger objects. In this case, the distance between the bellows should be increased.

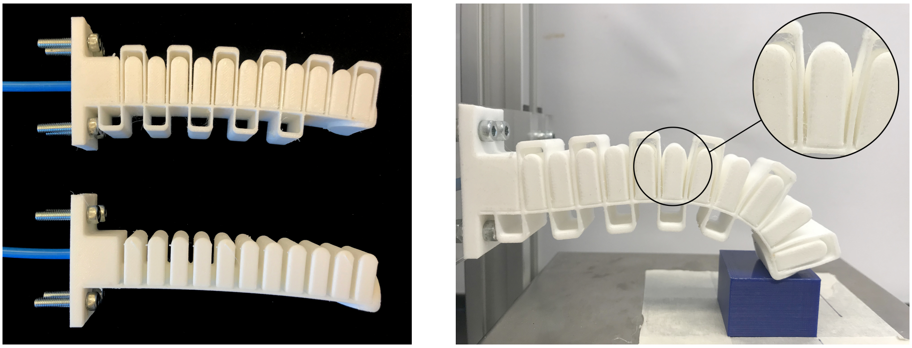

(a) (b)

Figure 6.10: (a) Fabricated design with and without stiffening structure. (b) Self-collision between the bellows and the stiffening-structure results in an increase in the exerted force.

6.4 Results

We compare our design to a reference design with an identical inextensible layer with a thickness of $0.8\,\mathrm{mm}$ and a width of $20\,\mathrm{mm}$ (see the bottom of Fig. 6.10(a)). We test the actuators using the same setup shown in Fig. 6.3. Figure 6.11 shows the vertical forces exerted on the flat surface and the $45°$ angled surface. The design with stiffening-structure was able to exert a force of $3.11\,N$ on a $45°$ angled surface before reaching a sidewards displacement of $20\,\mathrm{mm}$. This force is more than 70% higher than that of the reference design $(1.82\,N)$. It is also observed that at the same pressure the stiffening-structure reinforced design exerts a larger in-plane force on the flat surface. This can be explained by the accelerated self-collision between the bellows due to the stiffening-structure, as is highlighted in Fig. 6.10(b).

We integrate the bellows with stiffening-structure onto a gripper with three fingers. Figure 6.12 shows the newly designed gripper grasping a variety of objects stably at a pressure of $500\,\mathrm{kPa}$. It should be noted that the gripper with the $6\,\mathrm{mm}$-width beam failed to grasp the spherical object (Fig. 6.2) before reaching such a pressure, with a failure happening at a pressure of $400\,\mathrm{kPa}$. Similarly, a gripper built from the reference design actuators (Fig. 6.10(b)) showed several failed grasps for the tape-measure, the wrench and the marker at pressures below $500\,\mathrm{kPa}$ due to out-of-plane deformation. The design with stiffening-structure also increases the quality of the successful grasps in terms of holding force. Note that oblong objects such as the wrench and the marker

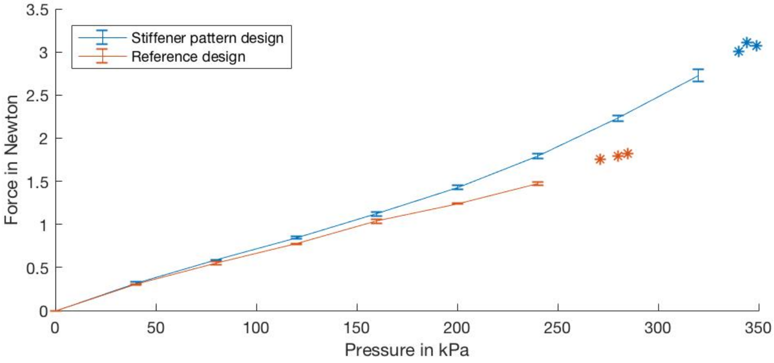

(a)

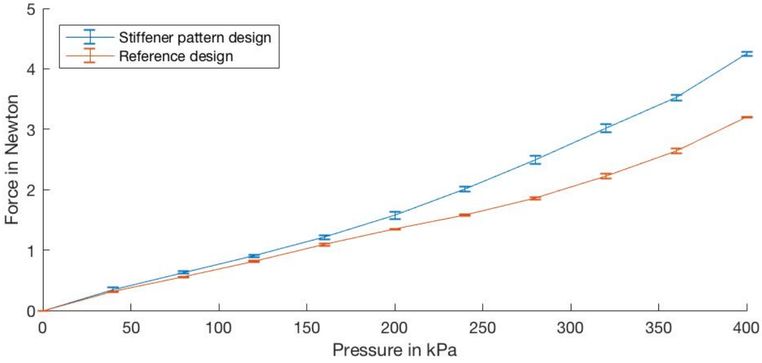

(b)

Figure 6.11: Vertical component of the in-plane force exerted by different designs on a $45°$ angled surface (top) and a flat surface (bottom). Slippage points are indicated by a star.

are held in place in a straight orientation, whereas the reference gripper would hold these objects in a less stable orientation due to out-of-plane deformation of the gripper fingers. We further demonstrate the improved grasping stability in the supplementary video material.

6.5 Conclusions

This chapter demonstrates the importance of the out-of-plane stiffness of soft actuators for grasping stability. Under the same in-plane deformation, a smaller out-of-plane deformation is beneficial for stable grasping.

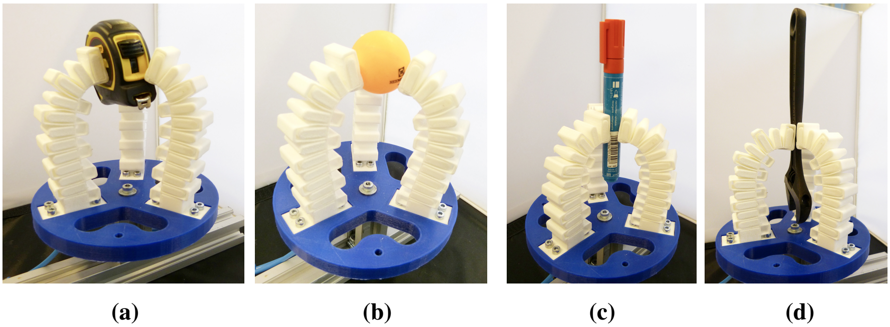

Figure 6.12: A gripper consisting of three actuators with the stiffening-structure can stably grasp a variety of objects at a high pressure of $500\,\mathrm{kPa}$.

The newly designed stiffening-structure increases the out-of-plane stiffness with minimal influence on the in-plane stiffness. The stiffening-structure retains a significant out-of-plane stiffness when it is in a bent configuration. An actuator with the reinforced out-of-plane stiffness is able to exert higher forces without slippage when confronted with asymmetric loadings.

7

Discussion

In the previous chapters, the results of the five research cycles of this research project were presented. The research has focused on the development of soft actuators with proprioception in order to move towards the use of soft robotic manipulators for dexterous manipulation tasks. In this chapter, the implications of this development are discussed. First, the role of proprioception in performing dexterous manipulation tasks with soft robots is discussed. Second, the implications of soft robotic manipulators for dexterous manipulation tasks such as harvesting on sustainability are discussed, with a focus on the role of proprioception. Third, the impact on jobs caused by the automation of these tasks is briefly discussed. Finally, we argue that the necessity of an integrated design approach for developing soft manipulators with proprioception will further implicate product designers in the development of robots. The last paragraph of this discussion discusses the role of the designer in the development of soft robots.

7.1 Implications of the Research

7.1.1 Proprioception for Dexterous Manipulation

The soft robotic manipulators developed in this work are intended to complete dexterous manipulation tasks by employing a grasping strategy that is inspired by that of the human hand. To allow for similar control strategies, this work is aimed at realizing a similar level of proprioceptive accuracy as well. However, systems that are completely composed of soft materials and have virtually infinite DOFs (e.g. the tentacles of the octopus) commonly show a very different approach to dexterous manipulation than an articulated hand. Here, the accuracy of proprioception and control is often less important and compensated for by the compliance of the soft structures [99]. The commercially available soft grippers mentioned in Chapter 1 have shown that the control of an adaptive caging grasp with multi-finger grippers can be greatly simplified as well through the use of soft materials and without the presence of any proprioception. However, for dexterous manipulation tasks such as harvesting an apple, the brain needs to be involved in the task execution as well. For example, harvesting an apple requires finding the stem of the apple by touch and tilting the apple around it, which requires knowledge of what an apple looks like. For the planning of such tasks, the brain has to rely on accurate proprioceptive signals. Similarly, accurate proprioception of the soft actuators is needed to decide upon the actuation strategy. Exploiting the softness of the actuator, the execution of the adaptive caging grasp that follows can still be greatly simplified in terms of control.

7.1.2 Sustainability

Agriculture is currently facing serious sustainability challenges. Intense farming has negatively impacted the environment through deforestation, reduced biodiversity, soil-erosion and -degradation, and plastic waste. While agriculture needs to make a transition to more sustainable practices, it must also deal with the consequences of climate change and an increasing food demand due to a rapidly growing world population [100].

Part of the solution may lie in moving from monocultures, in which fields only contain a single crop at a time, towards polycultures in which multiple species are grown at the same time. Examples of such agricultural land management systems include combining agriculture with growing trees (agroforestry [101]) and growing multiple crops in close proximity (intercropping [102]). Their benefits include increased biodiversity; soil quality; nutrient management; water-holding capacity; control of weeds, diseases, and pests; pollination services; carbon sequestration; energy efficiency and reduction of warming potential; resistance and resilience to climate change; and crop productivity [103], [104].

Figure 7.1: Example of agroforestry (left) and intercropping (right) - *Photo Credits: Duchy apple agroforestry July 2014 by Phil Sumption ORC, https://www.flickr.com/photos/agforward/14875280528/ (left), and Romania, https://commons.wikimedia.org/wiki/File:Romania.jpg (right), License at http://creativecommons.org/licenses/by/2.0.*

However, the maintenance of diversified agroecosystems generally requires more manual labor and skills than mechanized monocultures. A major barrier to the adoption of these systems is the shortage of qualified human labor [105]. Research into soft robotics as enabling technology for diversified agroecosystems concludes that there are opportunities for soft robots to make these systems more feasible through their potential ability to manage intricate agricultural tasks [105]. However, the research also indicates that there are several open questions on control and sensing for soft robots. This research contributes to addressing these challenges.

Besides the potential of soft robotics to aid the adoption of more sustainable agricultural practices, it also faces challenges with respect to sustainability. Firstly, there is a challenge with respect to food waste. Harvesting is already a critical loss point in the food supply chain [106]. Therefore, it is important that automation of harvesting tasks does not come at the cost of increased food losses due to poor handling. Although it is not unimaginable that soft manipulators could outperform manual labor in terms of effectiveness in the future, the current state of the art is not capable of doing so. The development of accurate proprioception methods for soft robots is an important step in this direction.

Secondly, there are sustainability challenges regarding the durability, recyclability, and reuse of soft robots. The soft robots presented in this thesis commonly have a shorter lifespan than traditional rigid robots. This is mainly due to the use of fragile materials, imperfections in the manufacturing processes, and a knowledge gap as to how to design structures that undergo large deformations. However, through new smart materials and design methodologies, soft robotics has also allowed for replication of operations and functionalities of biological organisms that exploit softness [107]. Examples include biodegradable soft robots [108], edible soft robots [109], and self-healing soft robots [110]. Taking inspiration from nature, we can start to think of soft robots as organisms that live, die and decay with minimal impact on the environment.

7.1.3 Jobs

Many countries face a shortage of skilled agricultural workers [111]. A shortage of qualified human labor in agriculture is responsible for food losses during harvesting [106] and hinders the adoption of more sustainable agricultural systems [105]. The shortage of qualified labor is likely to grow due to an aging farming population [112] and mobility restrictions on seasonal migrant workers (e.g. due to the COVID-19 pandemic [113]). Therefore, automation of dexterous harvesting tasks is likely to be necessary to sustainably feed the growing world population.

It is likely that the development of soft manipulators capable of performing dexterous manipulation tasks will also impact other sectors. The tasks that are most likely to be automated are those that are highly repetitive, physically heavy, or dangerous, or that deal with labor shortage. Examples of such tasks are waste disposal and sorting, swab collection during a pandemic, and supporting the elderly in everyday life. For many of these tasks, robots are required to closely collaborate with the human. As soft robots are safer to interact with, the use of soft robots is a promising direction for enabling humans and robots to work closely together (e.g. human–robot coproduction [114]). Even for soft robots, proprioception is needed to guarantee safe interaction.

7.1.4 Industrial Design Engineering

In contrast to rigid robots, the specializations and components required to build a soft robot are highly dependent on each other. Thus, an integrated design ap-

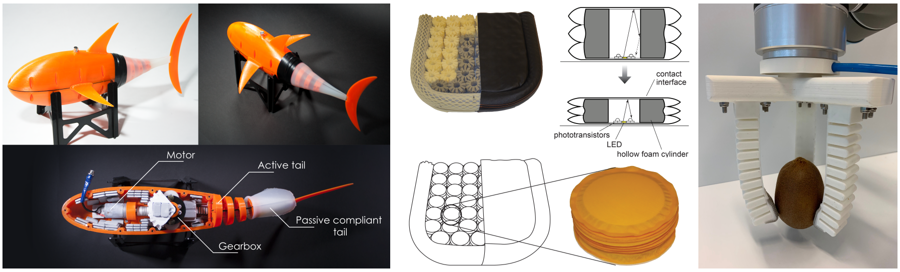

Figure 7.2: Integrated design of a soft robotic fish (left), soft robotic car seat (middle), and soft robotic gripper with silicone fingertips (right) - *Photo Credits: Sander van den Berg (left), Alice Buso (middle), and Lars Rossing (right)*

proach is needed in which all factors are taken into consideration during the entire design process. The integration of color patterns inside a soft pneumatic actuator to aid proprioception (Chapter 3) and the use of a structure that limits unwanted out-of-plane deformation and thereby simplifies sensor calibration and control (Chapter 6) are examples of how better solutions can be realized when components such as sensors and actuators are designed with a holistic approach. Due to the multidisciplinary nature of soft robotics, such a holistic approach often requires bringing together knowledge from various disciplines such as material science, mechatronics, zoology, computer science and industrial design. Moreover, to develop soft robots that successfully solve real-world problems, all stakeholders need to be involved throughout the design process. Industrial designers are adept at tackling such complex problems through an integrated design approach. Therefore, designers are expected to play a crucial role in advancing the field of soft robotics. To illustrate this point, three projects that were executed in collaboration with students or alumni from the Integrated Product Design (IPD) Master at Delft University of Technology are highlighted below.

The first project is a graduation project by Sander van den Berg (Fig. 7.2 [left]). The goal of the project was to develop a high-speed free-swimming soft robotic fish. The tuna-inspired design was able to achieve speeds of up to 0.85 m/s, outperforming the previously reported fastest free-swimming soft robotic fish by a margin of 27 % [115]. This feat could only be achieved through incorporating input from marine engineers and zoologists throughout the entire design process.

The second project is a graduation project by Alice Buso (Fig. 7.2 [middle]). The goal of this project was to use soft robotics to improve the comfort of BMW car seats. The final result is a layout of soft inflatable modules that can sense and control the pressure distribution in the seat [76]. Stakeholders such as BMW's seat factory, BMW's business unit, and the end user were involved throughout the entire design process to ensure a good fit between the actuator's design and its application.

The third project was executed in collaboration with IPD-alumni Lars Rossing (Fig. 7.2 [right]). The goal of this project was to fabricate soft robots that contain thermoplastic as well as silicone elements. This was achieved through a hybrid manufacturing method that combined 3D-printing of a thermoplastic structure with silicone casting [83]. This design could only be realized through simultaneous consideration of the manufacturing method and the design of the soft robots.

8

Conclusion

Following the discussion on the implications of the research, this chapter summarizes the main contributions of this research. The research questions defined in Chapter 1 are answered. Hereafter, the limitations of this research and opportunities for future work are discussed.

8.1 Contributions

The research presented in this thesis aims to address the challenges in building soft robotic manipulators with proprioception. It thus paves the way for the development of closed-loop control algorithms for soft robotic manipulators and, ultimately, the development of soft manipulators capable of performing dexterous manipulation tasks. The research objective was divided into four research questions, which were answered through five research cycles. The answers to the research questions are discussed below.

8.1.1 Answers to the research questions

RQ1 *What combination of actuation technique(s), sensing technique(s), and fabrication technique(s) for soft robotic manipulators can facilitate an integrated design approach to design the behavior of soft robotic manipulators with proprioception?*

A combination of pneumatic actuation, optical sensing with machine learning-based calibration, and additive manufacturing (AM) was found to facilitate an integrated design approach to design the behavior of soft robotic manipulators with proprioception. Soft pneumatic actuators provide designers with the possibility of realizing a wide range of forces and motions merely by adjusting the geometry of the air chambers, which allows them to adjust the behavior of the manipulator according to the application's requirements. AM allows multiple of these complexly shaped actuators to be fabricated in one go directly from the CAD file, almost regardless of the complexity of their geometry and without the need for design-specific tooling or assembly. This potential is demonstrated in Chapter 2. As the soft robot is driven by the inflation of the air chambers, the shapes of these air chambers are excellent indicators of the global soft robot shape. This feature, combined with the fact that these air chambers are insulated from external light, can be exploited to realize proprioception. A low number of small optical sensors and LEDs can be integrated into the air chambers to capture their shape (Chapter 3). In contrast to sensors that capture changes at specific locations of the soft robot, the signals captured by the optical sensors are always affected by the complete shape of the air chamber. Therefore, making changes in the design of the actuator (e.g. making the air chamber longer or changing the design of the bellow segments) does not require changing the design of the sensor. For each design, machine learning can be applied to learn the specific mapping between the sensor signals and the shape of the robot. From a design perspective, this model-free calibration has the advantage of being applicable to a wide range of designs without requiring changes in the approach.

RQ2 *How to endow soft actuators with embedded sensors that accurately capture the actuator's deformed shape?*

As discussed above, the shape of the air chambers of pneumatic soft robots are excellent indicators of their global shape. The deformed shape of soft pneumatic actuators was accurately captured by a number of optical sensors placed inside the inflatable air chambers. The signal for these optical sensors is realized by multiple light sources inside the air chamber. The amount of light from these light sources that is captured by the optical sensors depends on the shape of the air chamber at that time. Thus, the captured signals give a reliable indication of the actuator's shape, even when the soft robot is interacting with its environment. To enhance the change in signal upon deformation, color-based signal generators were embedded in the soft actuators such that a deformation would result in a change of color observed by color sensors. This sensing principle was demonstrated in Chapter 3. A comparison between the use of color signals and a single-intensity signal for a soft bending actuator is demonstrated in Chapter 4. Although the color signals enhance the accuracy, they are not necessary for capturing the shape of soft actuators with good accuracy. This finding is further demonstrated by the actuators presented in Chapter 5, which do not include colored patterns. The placement of the sensors also plays an important role in the accuracy with which the deformation is captured. A comparison of the obtained accuracy for different sensor layouts is presented in Chapter 4. With good placement, only a small number of signals is needed to capture the robot's deformation. A major advantage of using a small number of optical sensors is that they can be easily integrated inside the air chambers of soft actuators, such as on the inextensible layer of a soft bending actuator (Chapter 3)

RQ3 *How to reconstruct the shape of soft robots in real time?*

This research presents a method for reconstructing the shape of soft actuators from the signals of the optical sensors. First, the positions of a number of markers on the robot are captured using one or more cameras. Second, a large number of marker coordinates and their corresponding sensor signals are collected while the soft robot moves throughout its entire workspace and interacts with objects (Chapter 4 and 5). Next, the marker coordinates are converted to a reduced number of shape parameters that can be used to represent and reconstruct the shape of the soft robot in a computationally efficient way. Hereby, the solution for bending actuators presented in Chapter 4 can be scaled to complex structures with multiple interacting actuators and three-dimensional deformation. For example, the coordinates of a number of markers on a soft deformable membrane can be reduced to the control parameters of a Bézier surface, and marker coordinates on a soft continuum joint can be reduced to a rotation matrix and translation vector (see Chapter 5). A neural network is then deployed to learn the mapping between the signals from the optical sensors and the soft robot's shape parameters. By directly predicting the shape parameters instead of the marker coordinates, the sensing, prediction, and visualization of complex soft robot shapes can run in real time.

RQ4 *How to restrain superfluous degrees of freedom in soft robotic manipulators?*

This dissertation demonstrates how superfluous degrees of freedom in a soft robotic bending actuator can be restrained through the design of the soft actuator. This is achieved through embedding a structure inspired by compliant mechanisms in the 3D-printed soft actuator. This structure reduces the out-of-plane deformation without significantly increasing the in-plane bending stiffness (see Chapter 6). Thus, the grasping performance could be significantly improved.

8.2 Limitations and Future Work

The research presented in this thesis has several limitations and also indicates several opportunities for future work. These will be discussed below.

8.2.1 Process Automation

In this thesis, a set of actuation, sensing, and manufacturing techniques were proposed to facilitate an integrated approach to designing the behavior of soft robots with proprioception. However, multiple steps in this approach could be automated and optimized to further streamline and improve the design process.

- First, the design of the actuators could be automated and optimized. Although it was demonstrated that a wide range of behaviors can be realized through modifying the geometry of pneumatic actuators, it is still unclear what exact geometry should be generated to realize a desired behavior. The use of generative design methods could be an interesting direction towards automated generation of an actuator geometry based on the desired behavior as well as the manufacturing constraints. For an overview of design optimization methods for soft robots, see [116].
- Second, the placement of the optical sensors and light sources within the air chambers could be automated and optimized. For an example of sensor layout optimization for soft robots, see [42]. In this thesis, the indentification of a sensor and light-source layout for which the sensors are highly sensitive to changes in the shape of the actuator was largely based on empirical evidence. Future research may focus on evaluating and optimizing layouts through simulating the light inside the air chambers. This could lead to higher proprioceptive accuracy and a possible reduction of the number of sensors and light sources required inside the air chambers.
- Finally, the amount of training data required for calibration of the sensors could be optimized. In this thesis, a complete set of training data was collected across the entire soft robot workspace for every soft robot design, which is time-consuming. When fabricating multiple soft robots with a similar design and sensor layout, it might be possible to reuse training data that was acquired on other designs. Transfer learning may be used to calibrate a new soft robot based on only a small amount of new training data [117].

8.2.2 Durability

This thesis adopts AM of soft materials as a technology for fabricating soft pneumatic manipulators aimed at performing dexterous manipulation tasks in agricultural environments. This application area requires manipulators to be food-grade and to last for hundreds of thousands of actuation cycles. The soft pneumatic manipulators presented in this thesis do not meet those requirements. The multi-material actuators presented in Chapter 3 and 4 are built using PolyJet technology. The photo-polymers used in this process are not suitable for agricultural applications as they are too fragile and not food-grade. In contrast, selective laser sintering (adopted in Chapter 2) and fused deposition modeling (adopted in Chapter 6) allow for the use of high-quality thermoplastics. Although these actuators can typically last thousands of cycles, inconsistencies in manufacturing processes often lead to leaking air chambers. Further development of durable and food-grade soft materials for AM, consistent and precise AM processes, and a better mechanical design of soft actuators are needed to achieve the durability required for agricultural applications. A promising direction is the use of hybrid fabrication approaches to fabricate soft actuators, such as our method combining fused-deposition-modeling printing of thermoplastic polyurethane and casting of food-grade silicones [83]. An additional durability challenge for the soft robotic manipulators presented in this thesis is the wiring to the sensors that are mounted on a moving body. These wires are prone to failure due to fatigue or might break while the actuator is interacting with an object. Flexible printed circuit boards or 3D-printed electronics are both promising solutions for addressing this challenge [118]. More durable actuators and wiring would also allow for studying the long-term performance of the proprioception method. The prototypes developed in this work were typically tested over a period of several months without a noticeable decline in proprioceptive accuracy over time. However, sensor drift and changing mechanical properties of the soft actuators might worsen the performance over an extended amount of time. Future research might also focus on applying more advanced machine learning techniques to compensate for such long-term changes.

8.2.3 Closed-loop Control

This thesis presents a method for developing soft manipulators with accurate real-time proprioception. This is an important step towards using soft manipulators to perform dexterous manipulation tasks as it enables the development of closed-loop control algorithms. For an overview of control algorithms for soft robotic manipulators, see [119]. However, even with accurate proprioception, the development of such strategies is nontrivial (e.g. due to underactuation). It is expected that this research will contribute to solving control problems in soft robots, by providing a means of studying the dynamic behavior of soft robots while they are interacting with objects. This ability is expected to lead not only to the development of novel control algorithms for existing soft robot designs, but also perhaps to more knowledge on what DOFs should be restrained (such as in Chapter 6), how parts of the control can be outsourced to the body of the robot, and where additional actuators should be added to actively adjust the behavior of the soft robot. Such design improvements may in turn reduce the complexity of the final proprioceptive system that is required to perform a task. For example, a structure that reduces the out-of-plane deformation of soft bending actuators (see Chapter 6), eliminates the need for integrating additional sensors to capture the out-of-plane deformation. Moreover, a simpler 2D model with less shape parameters can be used to represent the actuator shape. This will not only speed up the reconstruction, but also reduces the amount of training data that is required to learn the mapping between the sensor signals and shape parameters. Finally, the machine learning model can be less complex as well.

Bibliography

[1] C. Piazza, G. Grioli, M. Catalano, and A. Bicchi, “A century of robotic hands”, *Annual Review of Control, Robotics, and Autonomous Systems*, vol. 2, no. 1, pp. 1–32, 2019.

[2] S. Jacobsen, E. Iversen, D. Knutti, R. Johnson, and K. Biggers, “Design of the Utah/M.I.T. dextrous hand”, in *Proceedings. 1986 IEEE International Conference on Robotics and Automation*, vol. 3, 1986, pp. 1520–1532.

[3] H. Kawasaki, T. Komatsu, K. Uchiyama, and T. Kurimoto, “Dexterous anthropomorphic robot hand with distributed tactile sensor: Gifu hand II”, in *IEEE SMC’99 Conference Proceedings. 1999 IEEE International Conference on Systems, Man, and Cybernetics (Cat. No.99CH37028)*, vol. 2, 1999, 782–787 vol.2.

[4] J. Butterfass, M. Grebenstein, H. Liu, and G. Hirzinger, “DLR-Hand II: Next generation of a dextrous robot hand”, in *Proceedings 2001 ICRA. IEEE International Conference on Robotics and Automation (Cat. No.01CH37164)*, vol. 1, 2001, 109–114 vol.1.

[5] J. Craig, Ping Hsu, and S. Sastry, “Adaptive control of mechanical manipulators”, in *Proceedings. 1986 IEEE International Conference on Robotics and Automation*, vol. 3, 1986, pp. 190–195.

[6] N. Hogan, “Impedance control: An approach to manipulation”, in *1984 American Control Conference*, 1984, pp. 304–313.

[7] T. Laliberte, L. Birglen, and C. Gosselin, “Underactuation in robotic grasping hands”, *Machine Intelligence & Robotic Control*, vol. 4, no. 3, pp. 1–11, 2002.

[8] T. William, “The BarrettHand grasper – programmably flexible part handling and assembly”, *Industrial Robot: An International Journal*, vol. 27, no. 3, pp. 181–188, Jan. 2000, ISSN: 0143-991X.

[9] C. Meijneke, G. A. Kragten, and M. Wisse, “Design and performance assessment of an underactuated hand for industrial applications”, *Mechanical Sciences*, vol. 2, no. 1, pp. 9–15, 2011.

[10] G. A. Pratt and M. M. Williamson, “Series elastic actuators”, in *Proceedings 1995 IEEE/RSJ International Conference on Intelligent Robots and Systems. Human Robot Interaction and Cooperative Robots*, vol. 1, 1995, 399–406 vol.1.

[11] D. Trivedi, C. D. Rahn, W. M. Kier, and I. D. Walker, "Soft robotics: Biological inspiration, state of the art, and future research", *Applied Bionics and Biomechanics*, vol. 5, pp. 99–117, 2008.

[12] D. Rus and M. T. Tolley, "Design, fabrication and control of soft robots", *Nature*, vol. 521, no. 7553, pp. 467–475, 2015, ISSN: 0028-0836.

[13] J. Hughes, U. Culha, F. Giardina, F. Guenther, A. Rosendo, and F. Iida, "Soft manipulators and grippers: A review", *Frontiers in Robotics and AI*, vol. 3, p. 69, 2016, ISSN: 2296-9144.

[14] **R. B. N. Scharff**, E. L. Doubrovski, W. A. Poelman, P. P. Jonker, C. C. L. Wang, and J. M. P. Geraedts, "Towards behavior design of a 3D-printed soft robotic hand", in *Soft Robotics: Trends, Applications and Challenges: Proceedings of the Soft Robotics Week, April 25-30, 2016, Livorno, Italy*. Springer International Publishing, 2017, pp. 23–29.

[15] H. Freyer, A. Breitfeld, S. Ulrich, R. Bruns, and J. Wulfsberg, "3D-printed elastomeric bellow actuator for linear motion", in *2014 International Conference on Additive Technologies (ICAT)*, Oct. 2014, pp. 29–32.

[16] A. D. Marchese, R. K. Katzschmann, and D. Rus, "A recipe for soft fluidic elastomer robots", *Soft Robotics*, vol. 2, no. 1, pp. 7–25, 2015.

[17] B. Mosadegh, P. Polygerinos, C. Keplinger, S. Wennstedt, R. F. Shepherd, U. Gupta, J. Shim, K. Bertoldi, C. J. Walsh, and G. M. Whitesides, "Pneumatic networks for soft robotics that actuate rapidly", *Advanced Functional Materials*, vol. 24, no. 15, pp. 2163–2170, 2014.

[18] R. Deimel and O. Brock, "A novel type of compliant and underactuated robotic hand for dexterous grasping", *The International Journal of Robotics Research*, vol. 35, no. 1-3, pp. 161–185, 2016.

[19] P. Polygerinos, Z. Wang, K. C. Galloway, R. J. Wood, and C. J. Walsh, "Soft robotic glove for combined assistance and at-home rehabilitation", *Robotics and Autonomous Systems (RAS) Special Issue on Wearable Robotics*, vol. 73, pp. 135–143, Nov. 2015.

[20] R. F. Shepherd, F. Ilievski, W. Choi, S. A. Morin, A. A. Stokes, A. D. Mazzeo, X. Chen, M. Wang, and G. M. Whitesides, "Multigait soft robot", *Proceedings of the National Academy of Sciences*, vol. 108, no. 51, pp. 20 400–20 403, 2011.

[21] H. Zhao, Y. Li, A. Elsamadisi, and R. Shepherd, "Scalable manufacturing of high force wearable soft actuators", *Extreme Mechanics Letters*, vol. 3, pp. 89–104, 2015.

[22] R. MacCurdy, R. K. Katzschmann, Y. Kim, and D. Rus, "Printable hydraulics: A method for fabricating robots by 3D co-printing solids and liquids", in *2016 IEEE International Conference on Robotics and Automation, ICRA 2016, Stockholm, Sweden, May 16-21, 2016*, D. Kragic, A. Bicchi, and A. D. Luca, Eds., IEEE, 2016, pp. 3878–3885.

[23] B. N. Peele, T. J. Wallin, H. Zhao, and R. F. Shepherd, "3d printing antagonistic systems of artificial muscle using projection stereolithography", *Bioinspiration & Biomimetics*, vol. 10, no. 5, p. 055 003, Sep. 2015.

[24] R. Slyper and J. Hodgins, "Prototyping robot appearance, movement, and interactions using flexible 3D printing and air pressure sensors", in *Proceedings of the 21st International Symposium on Robot and Human Interactive Communication*, ser. Ro-Man 2012, IEEE, 2012, pp. 6–11.

[25] W. M. Kier and K. K. Smith, "Tongues, tentacles and trunks: The biomechanics of movement in muscular-hydrostats", *Zoological Journal of the Linnean Society*, vol. 83, no. 4, pp. 307–324, 1985.

[26] E. Doubrovski, E. Tsai, D. Dikovsky, J. Geraedts, H. Herr, and N. Oxman, "Voxel-based fabrication through material property mapping: A design method for bitmap printing", *Computer-Aided Design*, vol. 60, no. March, pp. 3–13, 2015, ISSN: 0010-4485.

[27] **R. B. N. Scharff**, R. M. Doornbusch, X. L. Klootwijk, A. A. Doshi, E. L. Doubrovski, J. Wu, J. M. P. Geraedts, and C. C. L. Wang, "Color-based sensing of bending deformation on soft robots", in *2018 IEEE International Conference on Robotics and Automation (ICRA)*, 2018, pp. 4181–4187.

[28] K. C. Galloway, P. Polygerinos, C. J. Walsh, and R. J. Wood, "Mechanically programmable bend radius for fiber-reinforced soft actuators", in *2013 16th International Conference on Advanced Robotics (ICAR)*, 2013, pp. 1–6.

[29] A. D. Marchese, K. Komorowski, C. D. Onal, and D. Rus, "Design and control of a soft and continuously deformable 2D robotic manipulation system", in *2014 IEEE International Conference on Robotics and Automation (ICRA)*, 2014, pp. 2189–2196.

[30] M. Luo, W. Tao, F. Chen, T. K. Khuu, S. Ozel, and C. D. Onal, “Design improvements and dynamic characterization on fluidic elastomer actuators for a soft robotic snake”, in *2014 IEEE International Conference on Technologies for Practical Robot Applications (TePRA)*, 2014, pp. 1–6.

[31] M. D. Grissom, V. Chitrakaran, D. Dienno, M. Csencits, M. Pritts, B. Jones, W. McMahan, D. Dawson, C. Rahn, and I. Walker, “Design and experimental testing of the OctArm soft robot manipulator”, in *Unmanned Systems Technology VIII, Proceedings of the SPIE*, vol. 6230, 2006.

[32] J. T. Muth, D. M. Vogt, R. L. Truby, Y. Mengüç, D. B. Kolesky, R. J. Wood, and J. A. Lewis, “Embedded 3D printing of strain sensors within highly stretchable elastomers”, *Advanced Materials*, vol. 26, no. 36, pp. 6307–6312, 2014.

[33] C. Majidi, R. Kramer, and R. J. Wood, “A non-differential elastomer curvature sensor for softer-than-skin electronics”, *Smart Materials and Structures*, vol. 20, no. 10, p. 105 017, 2011.

[34] C. Lucarotti, M. Totaro, A. Sadeghi, B. Mazzolai, and L. Beccai, “Revealing bending and force in a soft body through a plant root inspired approach”, *Scientific Reports*, vol. 5, no. 1, p. 8788, 2015, ISSN: 2045-2322.

[35] O. Atalay, A. Atalay, J. Gafford, H. Wang, R. Wood, and C. Walsh, “A highly stretchable capacitive-based strain sensor based on metal deposition and laser rastering”, *Advanced Materials Technologies*, vol. 2, no. 9, p. 1 700 081, 2017.

[36] J. C. Yeo, H. K. Yap, W. Xi, Z. Wang, C.-H. Yeow, and C. T. Lim, “Flexible and stretchable strain sensing actuator for wearable soft robotic applications”, *Advanced Materials Technologies*, vol. 1, no. 3, p. 1 600 018, 2016.

[37] S. Li, H. Zhao, and R. F. Shepherd, “Flexible and stretchable sensors for fluidic elastomer actuated soft robots”, *MRS Bulletin*, vol. 42, no. 2, pp. 138–142, 2017.

[38] S. Ozel, E. H. Skorina, M. Luo, W. Tao, F. Chen, Yixiao Pan, and C. D. Onal, “A composite soft bending actuation module with integrated curvature sensing”, in *2016 IEEE International Conference on Robotics and Automation (ICRA)*, May 2016, pp. 4963–4968.

[39] H. Zhao, R. Huang, and R. F. Shepherd, “Curvature control of soft orthotics via low cost solid-state optics”, in *2016 IEEE International Conference on Robotics and Automation (ICRA)*, 2016, pp. 4008–4013.

[40] H. Zhao, K. O’Brien, S. Li, and R. F. Shepherd, “Optoelectronically innervated soft prosthetic hand via stretchable optical waveguides”, *Science Robotics*, vol. 1, no. 1, 2016.

[41] J. Morrow, H. Shin, C. Phillips-Grafflin, S. Jang, J. Torrey, R. Larkins, S. Dang, Y. Park, and D. Berenson, “Improving soft pneumatic actuator fingers through integration of soft sensors, position and force control, and rigid fingernails”, in *2016 IEEE International Conference on Robotics and Automation (ICRA)*, May 2016, pp. 5024–5031.

[42] V. Wall, G. Zöller, and O. Brock, “A method for sensorizing soft actuators and its application to the RBO hand 2”, in *2017 IEEE International Conference on Robotics and Automation (ICRA)*, May 2017, pp. 4965–4970.

[43] P. Polygerinos, Z. Wang, J. T. B. Overvelde, K. C. Galloway, R. J. Wood, K. Bertoldi, and C. J. Walsh, “Modeling of soft fiber-reinforced bending actuators”, *IEEE Transactions on Robotics*, vol. 31, no. 3, pp. 778–789, Jun. 2015, ISSN: 1552-3098.

[44] A. Brunton, C. A. Arikan, and P. Urban, “Pushing the limits of 3D color printing”, *ACM Trans. Graphics*, vol. 35, no. 1, pp. 1–13, 2015.

[45] **R. B. N. Scharff**, R. M. Doornbusch, E. L. Doubrovski, J. Wu, J. M. P. Geraedts, and C. C. L. Wang, “Color-based proprioception of soft actuators interacting with objects”, *IEEE/ASME Transactions on Mechatronics*, vol. 24, no. 5, pp. 1964–1973, 2019.

[46] A. Gupta, C. Eppner, S. Levine, and P. Abbeel, “Learning dexterous manipulation for a soft robotic hand from human demonstrations”, in *2016 IEEE/RSJ International Conference on Intelligent Robots and Systems (IROS)*, 2016, pp. 3786–3793.

[47] G. Gerboni, A. Diodato, G. Ciuti, M. Cianchetti, and A. Menciassi, “Feedback control of soft robot actuators via commercial flex bend sensors”, *IEEE/ASME Transactions on Mechatronics*, vol. 22, no. 4, pp. 1881–1888, 2017, ISSN: 1083-4435.

[48] H. Wang, M. Totaro, and L. Beccai, “Toward perceptive soft robots: Progress and challenges”, *Advanced Science*, p. 1 800 541, 2018.

[49] K. Elgeneidy, G. Neumann, M. Jackson, and N. Lohse, “Directly printable flexible strain sensors for bending and contact feedback of soft actuators”, *Frontiers in Robotics and AI*, vol. 5, p. 2, 2018, ISSN: 2296-9144.

[50] Y. Yang and Y. Chen, “Innovative design of embedded pressure and position sensors for soft actuators”, *IEEE Robotics and Automation Letters*, vol. 3, no. 2, pp. 656–663, 2018, ISSN: 2377-3766.

[51] K. Elgeneidy, N. Lohse, and M. Jackson, “Bending angle prediction and control of soft pneumatic actuators with embedded flex sensors – a data-driven approach”, *Mechatronics*, vol. 50, pp. 234–247, 2018, ISSN: 0957-4158.

[52] G. Saggio, F. Riillo, L. Sbernini, and L. R. Quitadamo, “Resistive flex sensors: A survey”, *Smart Materials and Structures*, vol. 25, no. 1, p. 013 001, 2016.

[53] M. K. Dobrzynski, R. Pericet-Camara, and D. Floreano, “Contactless deflection sensor for soft robots”, in *2011 IEEE/RSJ International Conference on Intelligent Robots and Systems*, 2011, pp. 1913–1918.

[54] A. Koivikko, E. S. Raei, V. Sariola, M. Mosallaei, and M. Mantysalo, “Soft actuators with screen-printed curvature sensors”, in *2017 IEEE SENSORS*, 2017, pp. 1–3.

[55] R. A. Bilodeau, E. L. White, and R. K. Kramer, “Monolithic fabrication of sensors and actuators in a soft robotic gripper”, in *2015 IEEE/RSJ International Conference on Intelligent Robots and Systems (IROS)*, 2015, pp. 2324–2329.

[56] M. Giorelli, F. Renda, G. Ferri, and C. Laschi, “A feed-forward neural network learning the inverse kinetics of a soft cable-driven manipulator moving in three-dimensional space”, in *2013 IEEE/RSJ International Conference on Intelligent Robots and Systems*, 2013, pp. 5033–5039.

[57] M. Giorelli, F. Renda, M. Calisti, A. Arienti, G. Ferri, and C. Laschi, “Neural network and Jacobian method for solving the inverse statics of a cable-driven soft arm with nonconstant curvature”, *IEEE Transactions on Robotics*, vol. 31, no. 4, pp. 823–834, Aug. 2015, ISSN: 1552-3098.

[58] G. Runge, M. Wiese, and A. Raatz, “Fem-based training of artificial neural networks for modular soft robots”, in *2017 IEEE International Conference on Robotics and Biomimetics (ROBIO)*, Dec. 2017, pp. 385–392.

[59] S. Han, T. Kim, D. Kim, Y. Park, and S. Jo, “Use of deep learning for characterization of microfluidic soft sensors”, *IEEE Robotics and Automation Letters*, vol. 3, no. 2, pp. 873–880, Apr. 2018, ISSN: 2377-3766.

[60] I. M. Van Meerbeek, C. M. De Sa, and R. F. Shepherd, “Soft optoelectronic sensory foams with proprioception”, *Science Robotics*, vol. 3, no. 24, 2018.

[61] T. G. Thuruthel, B. Shih, C. Laschi, and M. T. Tolley, “Soft robot perception using embedded soft sensors and recurrent neural networks”, *Science Robotics*, vol. 4, no. 26, 2019.

[62] **R. B. N. Scharff**, G. Fang, Y. Tian, J. Wu, J. M. P. Geraedts, and C. C. L. Wang, “Sensing and reconstruction of 3D deformation on pneumatic soft robots”, *IEEE/ASME Transactions on Mechatronics (**under review**)*, 2020.

[63] R. L. Truby, M. Wehner, A. K. Grosskopf, D. M. Vogt, S. G. M. Uzel, R. J. Wood, and J. A. Lewis, “Soft somatosensitive actuators via embedded 3D printing”, *Advanced Materials*, vol. 30, no. 15, p. 1 706 383, 2018.

[64] R. L. Truby, C. D. Santina, and D. Rus, “Distributed proprioception of 3D configuration in soft, sensorized robots via deep learning”, *IEEE Robotics and Automation Letters*, vol. 5, no. 2, pp. 3299–3306, 2020.

[65] W. Felt, M. Suen, and C. D. Remy, “Sensing the motion of bellows through changes in mutual inductance”, in *2016 IEEE/RSJ International Conference on Intelligent Robots and Systems (IROS)*, Oct. 2016, pp. 5252–5257.

[66] W. Felt, M. J. Telleria, T. F. Allen, G. Hein, J. B. Pompa, K. Albert, and C. D. Remy, “An inductance-based sensing system for bellows-driven continuum joints in soft robots”, *Auton. Robots*, vol. 43, no. 2, pp. 435–448, Feb. 2019, ISSN: 0929-5593.

[67] H. Bai, S. Li, J. Barreiros, Y. Tu, C. R. Pollock, and R. F. Shepherd, “Stretchable distributed fiber-optic sensors”, *Science*, vol. 370, no. 6518, pp. 848–852, 2020, ISSN: 0036-8075.

[68] S. Sareh, Y. Noh, M. Li, T. Ranzani, H. Liu, and K. Althoefer, “Macrobend optical sensing for pose measurement in soft robot arms”, *Smart Materials and Structures*, vol. 24, no. 12, p. 125 024, Nov. 2015.

[69] Teichert Systemtechnik GmbH. (2019). Innovative cable-like-shape-sensor, [Online]. Available: `http://www.tst-inno.de/cable-like-shape-sensor/?lang=en` (visited on 12/30/2020).

[70] R. Wang, S. Wang, E. Xiao, K. Jindal, W. Yuan, and C. Feng, "Real-time soft robot 3D proprioception via deep vision-based sensing", *CoRR*, vol. abs/1904.03820, 2019. arXiv: `1904.03820`. [Online]. Available: `http://arxiv.org/abs/1904.03820`.

[71] G. Soter, H. Hauser, A. Conn, J. Rossiter, and K. Nakajima, "Shape reconstruction of CCD camera-based soft tactile sensors", in *2020 IEEE/RSJ International Conference on Intelligent Robots and Systems (IROS)*, 2020.

[72] B. Ward-Cherrier, N. Pestell, L. Cramphorn, B. Winstone, M. E. Giannaccini, J. Rossiter, and N. F. Lepora, "The TacTip family: Soft optical tactile sensors with 3d-printed biomimetic morphologies", *Soft Robotics*, vol. 5, no. 2, pp. 216–227, 2018.

[73] X. Lin, L. Willemet, A. Bailleul, and M. Wiertlewski, "Curvature sensing with a spherical tactile sensor using the color-interference of a marker array", in *2020 IEEE International Conference on Robotics and Automation (ICRA)*, 2020.

[74] W. Yuan, S. Dong, and E. Adelson, "GelSight: High-resolution robot tactile sensors for estimating geometry and force", *Sensors*, vol. 17, no. 12, p. 2762, Nov. 2017, ISSN: 1424-8220.

[75] P. Werner, M. Hofer, C. Sferrazza, and R. D'Andrea, "Vision-based proprioceptive sensing: Tip position estimation for a soft inflatable bellow actuator", in *2020 IEEE/RSJ International Conference on Intelligent Robots and Systems (IROS)*, Oct. 2020.

[76] A. Buso, **R. B. N. Scharff**, E. L. Doubrovski, J. Wu, C. C. L. Wang, and P. Vink, "Soft robotic module for sensing and controlling contact force", in *2020 3rd IEEE International Conference on Soft Robotics (RoboSoft)*, 2020, pp. 70–75.

[77] R. Xu, A. Asadian, A. S. Naidu, and R. V. Patel, "Position control of concentric-tube continuum robots using a modified Jacobian-based approach", in *ICRA*, IEEE, 2013, pp. 5813–5818, ISBN: 978-1-4673-5641-1.

[78] M. Bächer, B. Hepp, F. Pece, P. G. Kry, B. Bickel, B. Thomaszewski, and O. Hilliges, "DefSense: Computational design of customized deformable input devices", in *Proceedings of the 2016 CHI Conference on Human Factors in Computing Systems*, ser. CHI '16, San Jose, California, USA: ACM, 2016, pp. 3806–3816, ISBN: 978-1-4503-3362-7.

[79] T. L. T. Lun, K. Wang, J. D. L. Ho, K. Lee, K. Y. Sze, and K. Kwok, "Real-time surface shape sensing for soft and flexible structures using fiber bragg gratings", *IEEE Robotics and Automation Letters*, vol. 4, no. 2, pp. 1454–1461, Apr. 2019, ISSN: 2377-3766.

[80] O. Glauser, D. Panozzo, O. Hilliges, and O. Sorkine-Hornung, "Deformation capture via soft and stretchable sensor arrays", *ACM Trans. Graph.*, vol. 38, no. 2, 16:1–16:16, Mar. 2019, ISSN: 0730-0301.

[81] C. Sferrazza and R. D'Andrea, "Transfer learning for vision-based tactile sensing", *CoRR*, vol. abs/1812.03163, 2018.

[82] W. Yuan, C. Zhu, A. Owens, M. A. Srinivasan, and E. H. Adelson, "Shape-independent hardness estimation using deep learning and a GelSight tactile sensor", in *2017 IEEE International Conference on Robotics and Automation (ICRA)*, May 2017, pp. 951–958.

[83] L. Rossing, **R. B. N. Scharff**, B. Chömpff, C. C. L. Wang, and E. L. Doubrovski, "Bonding between silicones and thermoplastics using 3D printed mechanical interlocking", *Materials & Design*, vol. 186, p. 108 254, 2020, ISSN: 0264-1275.

[84] D. W. Eggert, A. Lorusso, and R. B. Fisher, "Estimating 3-D rigid body transformations: a comparison of four major algorithms", *Machine Vision and Applications*, vol. 9, no. 5, pp. 272–290, 1997, ISSN: 1432-1769.

[85] **R. B. N. Scharff**, J. Wu, J. M. P. Geraedts, and C. C. L. Wang, "Reducing out-of-plane deformation of soft robotic actuators for stable grasping", in *2019 2nd IEEE International Conference on Soft Robotics (RoboSoft)*, 2019, pp. 265–270.

[86] F. Ilievski, A. D. Mazzeo, R. F. Shepherd, X. Chen, and G. M. Whitesides, "Soft robotics for chemists", *Angewandte Chemie*, vol. 123, no. 8, pp. 1930–1935, 2011.

[87] K. C. Galloway, K. P. Becker, B. Phillips, J. Kirby, S. Licht, D. Tchernov, R. J. Wood, and D. F. Gruber, "Soft robotic grippers for biological sampling on deep reefs", *Soft Robotics*, vol. 3, no. 1, pp. 23–33, 2016.

[88] T. Okada, “Computer control of multijointed finger system for precise object-handling”, *IEEE Transactions on Systems, Man, and Cybernetics*, vol. 12, no. 3, pp. 289–299, May 1982, ISSN: 0018-9472.

[89] M. Rakić, “Multifingered robot hand with selfadaptability”, *Robotics and Computer-Integrated Manufacturing*, vol. 5, no. 2, pp. 269–276, 1989.

[90] K. Suzumori, S. Iikura, and H. Tanaka, “Development of flexible microactuator and its applications to robotic mechanisms”, in *Proceedings. 1991 IEEE International Conference on Robotics and Automation*, vol. 2, Apr. 1991, pp. 1622–1627.

[91] H. K. Yap, H. Y. Ng, and C.-H. Yeow, “High-force soft printable pneumatics for soft robotic applications”, *Soft Robotics*, vol. 3, no. 3, pp. 144–158, 2016.

[92] P. Polygerinos, S. Lyne, Z. Wang, L. F. Nicolini, B. Mosadegh, G. M. Whitesides, and C. J. Walsh, “Towards a soft pneumatic glove for hand rehabilitation”, in *2013 IEEE/RSJ International Conference on Intelligent Robots and Systems*, Nov. 2013, pp. 1512–1517.

[93] P. Glick, S. A. Suresh, D. Ruffatto, M. Cutkosky, M. T. Tolley, and A. Parness, “A soft robotic gripper with gecko-inspired adhesive”, *IEEE Robotics and Automation Letters*, vol. 3, no. 2, pp. 903–910, Apr. 2018, ISSN: 2377-3766.

[94] T. Yamada, T. Koishikura, Y. Mizuno, N. Mimura, and Y. Funahashi, “Stability analysis of 3D grasps by a multifingered hand”, in *Proceedings 2001 ICRA. IEEE International Conference on Robotics and Automation*, vol. 3, May 2001, 2466–2473 vol.3.

[95] D. M. Brouwer, J. P. Meijaard, and J. B. Jonker, “Elastic element showing low stiffness loss at large deflection”, in *Proceedings of the 24th Annual Meeting of the American Society of Precision Engineering, Monterey,CA.*, 2009, pp. 30–33.

[96] D. H. Wiersma, S. E. Boer, R. G. K. M. Aarts, and D. M. Brouwer, “Design and performance optimization of large stroke spatial flexures”, *Journal of Computational and Nonlinear Dynamics*, vol. 9, no. 1, pp. 11 010–11 016, Nov. 2013, ISSN: 1555-1415.

[97] S. Awtar, A. H. Slocum, and E. Sevincer, “Characteristics of beam-based flexure modules”, *Journal of Mechanical Design*, vol. 129, no. 6, pp. 625–639, May 2006, ISSN: 1050-0472.

[98] W. C. Young, R. G. Budynas, and A. M. Sadegh, *Roark's formulas for stress and strain; 8th ed.* New York, NY: McGraw Hill, 2012.

[99] B. Mazzolai, A. Mondini, F. Tramacere, G. Riccomi, A. Sadeghi, G. Giordano, E. Del Dottore, M. Scaccia, M. Zampato, and S. Carminati, "Octopus-inspired soft arm with suction cups for enhanced grasping tasks in confined environments", *Advanced Intelligent Systems*, vol. 1, no. 6, p. 1 900 041, 2019.

[100] "World population prospects 2019", United Nations, Department of Economic and Social Affairs, Population Division, 2019. [Online]. Available: `https://population.un.org/wpp/` (visited on 2019).

[101] R. P. K. Nair, *An introduction to agroforestry*. Springer, 1993.

[102] J. H. Vandermeer, *The Ecology of Intercropping*. Cambridge University Press, 1989.

[103] C. Kremen and A. Miles, "Ecosystem services in biologically diversified versus conventional farming systems: Benefits, externalities, and trade-offs", *Ecology and Society*, vol. 17, no. 4, 2012, ISSN: 17083087.

[104] C. Sirami, N. Gross, A. B. Baillod, C. Bertrand, R. Carrié, A. Hass, L. Henckel, P. Miguet, C. Vuillot, A. Alignier, J. Girard, P. Batáry, Y. Clough, C. Violle, D. Giralt, G. Bota, I. Badenhausser, G. Lefebvre, B. Gauffre, A. Vialatte, F. Calatayud, A. Gil-Tena, L. Tischendorf, S. Mitchell, K. Lindsay, R. Georges, S. Hilaire, J. Recasens, X. O. Solé-Senan, I. Robleño, J. Bosch, J. A. Barrientos, A. Ricarte, M. Á. Marcos-Garcia, J. Miñano, R. Mathevet, A. Gibon, J. Baudry, G. Balent, B. Poulin, F. Burel, T. Tscharntke, V. Bretagnolle, G. Siriwardena, A. Ouin, L. Brotons, J.-L. Martin, and L. Fahrig, "Increasing crop heterogeneity enhances multitrophic diversity across agricultural regions", *Proceedings of the National Academy of Sciences*, vol. 116, no. 33, pp. 16 442–16 447, 2019, ISSN: 0027-8424.

[105] G. Chowdhary, M. Gazzola, G. Krishnan, C. Soman, and S. Lovell, "Soft robotics as an enabling technology for agroforestry practice and research", *Sustainability*, vol. 11, no. 23, p. 6751, Nov. 2019, ISSN: 2071-1050.

[106] "The state of food and agriculture, Moving forward on food loss and waste reduction", Food and Agriculture Organization of the United Nations (FAO), 2019. [Online]. Available: `http://www.fao.`

org/state-of-food-agriculture/2019/en/ (visited on 2019).

[107] J. Rossiter, J. Winfield, and I. Ieropoulos, “Eating, drinking, living, dying and decaying soft robots”, in *Soft Robotics: Trends, Applications and Challenges*, Cham: Springer International Publishing, 2017, pp. 95–101, ISBN: 978-3-319-46460-2.

[108] ——, “Here today, gone tomorrow: Biodegradable soft robots”, in *Electroactive Polymer Actuators and Devices (EAPAD) 2016*, Y. Bar-Cohen and F. Vidal, Eds., International Society for Optics and Photonics, vol. 9798, SPIE, 2016, pp. 312–321.

[109] J. Shintake, H. Sonar, E. Piskarev, J. Paik, and D. Floreano, “Soft pneumatic gelatin actuator for edible robotics”, in *2017 IEEE/RSJ International Conference on Intelligent Robots and Systems (IROS)*, 2017, pp. 6221–6226.

[110] S. Terryn, J. Brancart, D. Lefeber, G. Van Assche, and B. Vanderborght, “Self-healing soft pneumatic robots”, *Science Robotics*, vol. 2, no. 9, 2017.

[111] “Determining labour shortages and the need for labour migration from third countries in the eu”, Migration & Home Affairs - European Commission, 2015. [Online]. Available: `https://ec.europa.eu/home-affairs/sites/homeaffairs/files/what-we-do/networks/european_migration_network/reports/docs/emn-studies/emn_labour_shortages_synthesis__final.pdf` (visited on 2020).

[112] “Young people in farming”, European Commission. [Online]. Available: `https://ec.europa.eu/info/food-farming-fisheries/key-policies/common-agricultural-policy/income-support/young-farmers_en` (visited on 2020).

[113] S. Kalantaryan, J. Mazza, and M. Scipioni, “Meeting labour demand in agriculture in times of covid 19 pandemic”, European Commission, 2020. [Online]. Available: `https://ec.europa.eu/jrc/en/publication/annual-reports/meeting-labour-demand-agriculture-times-covid-19-pandemic` (visited on 2020).

[114] A. Çençen, J. Verlinden, and J. Geraedts, “Design methodology to improve human-robot coproduction in small and medium sized enterprises”, English, *IEEE - ASME Transactions on Mechatronics*, vol. 23, no. 3, pp. 1092–1102, 2018, ISSN: 1083-4435.

[115] S. C. van den Berg, **R. B. N. Scharff**, Z. Rusák, and J. Wu, “Biomimetic design of a soft robotic fish for high speed locomotion”, in *Biomimetic and Biohybrid Systems*, Cham: Springer International Publishing, 2020, pp. 366–377, ISBN: 978-3-030-64313-3.

[116] F. Chen and M. Y. Wang, “Design optimization of soft robots: A review of the state of the art”, *IEEE Robotics Automation Magazine*, vol. 27, no. 4, pp. 27–43, 2020.

[117] G. Fang, Y. Tian, Z.-X. Yang, J. M. P. Geraedts, and C. C. L. Wang, “Jacobian-based learning for inverse kinematics of soft robots”, *arXiv e-prints*, arXiv:2012.13965, arXiv:2012.13965, Dec. 2020. arXiv: `2012.13965 [cs.RO]`.

[118] Y. Song, R. A. Boekraad, L. Roussos, A. Kooijman, C. C. L. Wang, and J. M. P. Geraedts, “3D printed electronics: Opportunities and challenges from case studies”, in *ASME 2017 International Design Engineering Technical Conferences and Computers and Information in Engineering Conference (IDETC-CIE2017)*, Aug. 2017, ISBN: 978-0-7918-5811-0.

[119] T. George Thuruthel, Y. Ansari, E. Falotico, and C. Laschi, “Control strategies for soft robotic manipulators: A survey”, *Soft Robotics*, vol. 5, no. 2, pp. 149–163, 2018.

Appendix

Color Sensor PCB Design

This appendix discusses the sensor design. The design of the sensor plug has been shown in Fig. 4.5. The body of the plug is fabricated by a PolyJet 3D printing system using the rigid VeroCyan and the flexible Agilus30 photopolymers. Two *Printed Circuit Boards* (PCBs) – both customized – are mounted on the top and the bottom parts of the plug. The designs of these PCBs are shown in Fig. 8.1. The schemes of the upper and the lower PCBs can be found in Fig. 8.2. Wires are guided through the 3D-printed plug to connect the upper and lower PCB in an airtight way.

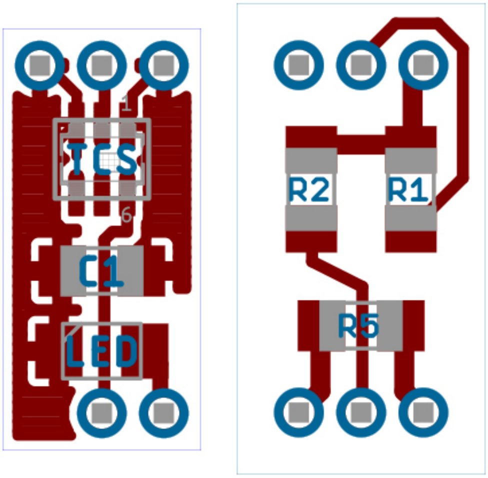

Figure 8.1: The design of the upper PCB (left with dimension: $10.80\ \mathrm{mm} \times 5.08\ \mathrm{mm}$) and the design of the lower PCB (right with dimension: $12.07\ \mathrm{mm} \times 6.35\ \mathrm{mm}$

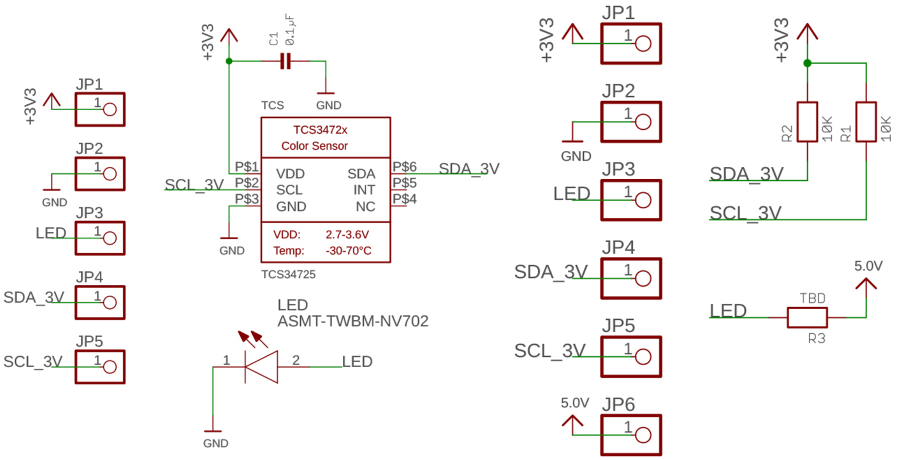

Figure 8.2: Scheme of the upper PCB (left) and lower PCB (right)

Acknowledgments

The execution of this research would not have been possible without the support of many individuals.

I would like to start by thanking Prof.dr. Charlie Wang, Prof.dr.ir. Jo Geraedts, and Dr. Jun Wu. Charlie Wang, thank you for believing in me and giving me the chance to start my doctoral research under your guidance. You have always helped me to bring out the best in myself and provided me with everything I needed to develop myself professionally. Jo Geraedts, thank you for sharing your knowledge and managerial skills with me ever since the first day of my MSc graduation project. I would not be where I am today without your help. Jun Wu, thank you for always having my best interests at heart. You have been a great mentor to me and I will miss your advice as well as our weekly research discussions.

Doctoral committee members, Prof.dr.ir. R.H.M. Goossens, Prof.dr.ir. D.A. Abbink, Dr. B. Mazzolai, Dr. A. Weightman and Prof.dr. P. Vink, thank you for reading my dissertation and providing me with valuable feedback.

Thanks should also go to Em.Prof.dr.ing Wim Poelman and Em.Prof.dr.ir. Pieter Jonker for their guidance during my MSc graduation project on the development of a soft robotic hand. You showed me how exciting conducting research can be and inspired me to pursue a PhD.

Argun Çençen, Chengkai Dai, Guoxin Fang, Rado Dukalski, Tim Kuipers, Willemijn Elkhuizen, Zishun Liu, and Zjenja Doubrovski. Thank you for the many special moments we shared together inside as well as outside the *Applied Labs*. I will never forget the *Soft Baxter* research demonstrations, festivals, hours in the gym, concerts, dinners, celebrations, barbeques at Delftse Hout, conference trips to Sweden, Singapore, and Australia, summerschool in Denmark, and half a year in Hong Kong. Besides all this, many of you have also directly or indirectly contributed to this research.

I must also thank all students, interns, and other collaborators who I have worked with over the past four years. A special thanks goes to the (co-)authors of one or more publications: Rens Doornbusch, Alex Klootwijk, Ajinkya Doshi, Lars Rossing, Bryan Chömpff, Alice Buso, Sander van den Berg, and Yingjun Tian.

Mauricio Sandoval, thank you very much for the great front cover art and

illustrations.

Additionally, I would like to thank Prof.dr.ir. Kaspar Jansen, Prof.dr. Elvin Karana, Dr. Yu Song, Dr.ir. Jouke Verlinden, Dr. Zoltán Rusák, Prof.dr.ir Just Herder, Prof.dr.ir. Paul Breedveld, Dr. Michaël Wiertlewski, Dr. Xi Lin, and Dr.ir. Aimée Sakes for the inspiring research discussions which led to valuable insights.

A big thanks to all who have made working in the lab so much fun: Martin, Adrie, Mascha, Tessa, Joris, Elvis, Doris, Helen, Dolores, Yusheng, Jun, Farzam, and Linda.

I am very grateful to my friends and family for their encouragement. In particular, I would like to thank the most important people in my life. Mom, dad, Anouk, Jelle, and Nathan, thank you for everything you have done for me. Amanda, thank you for your love and support every day. I am looking forwards to a new adventure with you.

Curriculum Vitæ

Rob Bernardus Nicolaas Scharff

09 Aug 1990 Born in Meerkerk, the Netherlands

Education

2017–2020 **PhD in the Materializing Futures section, IDE**
Delft University of Technology, The Netherlands
Thesis: Soft Robotic Manipulators with Proprioception
Promotors: Prof.dr. Charlie C.L. Wang
Prof.dr.ir. Jo M.P. Geraedts
Co-promotor: Dr. Jun Wu

2012–2015 **MSc Integrated Product Design**
Delft University of Technology

2008–2012 **BSc Industrial Design Engineering**
Delft University of Technology

Professional Experience

2019 **Honorary Research Assistant**
Department of Mechanical and Automation Engineering
The Chinese University of Hong Kong, Hong Kong

2015–2016 **Teacher/Researcher**
Department of Design Engineering
Delft University of Technology, The Netherlands

Publications

Journals

1. **R. B. N. Scharff**, R. M. Doornbusch, E. L. Doubrovski, J. Wu, J. M. P. Geraedts, and C. C. L. Wang, "Color-based proprioception of soft actuators interacting with objects", *IEEE/ASME Transactions on Mechatronics*, vol. 24, no. 5, pp. 1964–1973, 2019
2. **R. B. N. Scharff**, G. Fang, Y. Tian, J. Wu, J. M. P. Geraedts, and C. C. L. Wang, "Sensing and reconstruction of 3D deformation on pneumatic soft robots", *IEEE/ASME Transactions on Mechatronics (**under review**)*, 2020
3. L. Rossing, **R. B. N. Scharff**, B. Chömpff, C. C. L. Wang, and E. L. Doubrovski, "Bonding between silicones and thermoplastics using 3D printed mechanical interlocking", *Materials & Design*, vol. 186, p. 108 254, 2020, ISSN: 0264-1275
4. H. Khanbareh, K. de Boom, B. Schelen, **R. B. N. Scharff**, C. C. L. Wang, S. van der Zwaag, and P. Groen, "Large area and flexible micro-porous piezoelectric materials for soft robotic skin", *Sensors and Actuators A: Physical*, vol. 263, pp. 554–562, 2017, ISSN: 0924-4247
5. G. Fang, C. D. Matte, **R. B. N. Scharff**, T. H. Kwok, and C. C. L. Wang, "Kinematics of soft robots by geometric computing", *IEEE Transactions on Robotics*, vol. 36, no. 4, pp. 1272–1286, 2020

Conferences

1. **R. B. N. Scharff**, J. Wu, J. M. P. Geraedts, and C. C. L. Wang, "Reducing out-of-plane deformation of soft robotic actuators for stable grasping", in *2019 2nd IEEE International Conference on Soft Robotics (RoboSoft)*, 2019, pp. 265–270
2. **R. B. N. Scharff**, R. M. Doornbusch, X. L. Klootwijk, A. A. Doshi, E. L. Doubrovski, J. Wu, J. M. P. Geraedts, and C. C. L. Wang, "Color-based sensing of bending deformation on soft robots", in *2018 IEEE International Conference on Robotics and Automation (ICRA)*, 2018, pp. 4181–4187
3. A. Buso, **R. B. N. Scharff**, E. L. Doubrovski, J. Wu, C. C. L. Wang, and P. Vink, "Soft robotic module for sensing and controlling contact force", in *2020 3rd IEEE International Conference on Soft Robotics (RoboSoft)*, 2020, pp. 70–75
4. S. C. van den Berg, **R. B. N. Scharff**, Z. Rusák, and J. Wu, "Biomimetic design of a soft robotic fish for high speed locomotion", in *Biomimetic and Biohybrid Systems*, Cham: Springer International Publishing, 2020, pp. 366–377, ISBN: 978-3-030-64313-3

Book Chapters

1. **R. B. N. Scharff**, E. L. Doubrovski, W. A. Poelman, P. P. Jonker, C. C. L. Wang, and J. M. P. Geraedts, "Towards behavior design of a 3D-printed soft robotic hand", in *Soft Robotics: Trends, Applications and Challenges: Proceedings of the Soft Robotics Week, April 25-30, 2016, Livorno, Italy*. Springer International Publishing, 2017, pp. 23–29